UNIVERSITY OF Southampton

FACULTY OF ENGINEERING AND THE ENVIRONMENT

NATIONAL CENTRE FOR ADVANCED TRIBOLOGY AT SOUTHAMPTON (NCATS)

PHILIPS ORAL HEALTHCARE (POH)

MECHANICAL PROPERTIES AND DISRUPTION OF DENTAL BIOFILMS

By

AMIR RMAILE

ACADEMIC SUPERVISORS: DR PAUL STOODLEY, DR JULIAN WHARTON, DR PHILIPP THURNER

INDUSTRIAL SUPERVISORS: DR MARCELO ASPIRAS, DR MARILYN WARD, DR MARKO DE JAGER

THESIS SUBMITTED IN FULFILLMENT OF THE REQUIREMENT FOR THE DEGREE OF DOCTOR OF PHILOSOPHY

JULY 2013

Abstract

A literature review of dental plaque biofilms formation, progression and detachment mechanisms is presented in this thesis. Various strategies that have been employed to reduce or eliminate dental biofilms are discussed. The focus of the thesis was on the mechanical properties and disruption of dental biofilms, especially from hard-to-access areas of the oral cavity, such as the interproximal (IP) sites between the teeth. Various methods to measure mechanical properties of dental biofilms were investigated, and physical and chemical strategies to disrupt these biofilms were employed. *Streptococcus mutans*, the bacterium responsible for initiation of dental plaque biofilms, was used in our studies.

A uniaxial compressive test was utilized to characterize the mechanical behaviour of biofilms, while manipulating the chemical microenvironment. Initially, the mechanical properties of a dextran gel were characterized. The gel was used as an artificial dental plaque biofilm (Chapter 5). The elastic modulus of the gel was 17 kPa (± 12; n = 3), and the stress relaxation time was 25 seconds (± 18; n = 3), demonstrating a viscoelastic behaviour similar to that reported for real biofilms. After optimizing the technique with the gel, the mechanical properties of *S. mutans* biofilms were studied, the elastic modulus was 380 Pa (± 350; n = 30), and the stress relaxation time was 12 seconds (± 11; n = 10). The elastic modulus increased by increasing the sucrose percentage in the media, and decreased when the biofilms were treated with increasing concentrations of ethylene di-amine tetra acetic acid, EDTA. Treating the biofilms with different solutions of poly (ethylene glycol), PEG, resulted in behaviour similar to that previously observed for synthetic polymers.

The flow field and local hydrodynamics of high velocity water microdrops impacting the interproximal (IP) space of typodont teeth, and their influence on the structure and detachment of both surrogate dental plaque and *Streptococcus mutans* biofilms, were studied experimentally and computationally. Water droplets of 115 μL were produced by a prototype *AirFloss* (PT-*AirFloss*) device provided by Philips Oral Healthcare, bursting water at a velocity of 60 m/s into the IP space between the maxillary central incisors. High-speed imaging, was used to characterise the PT-*AirFloss* microburst of pressurized air and water micodrops, and demonstrated the removal mechanism of a

dental plaque biofilm substitute and the *S. mutans* biofilms. Using various microscopy and image analysis techniques, quantitative measurements of the removal rate and the percentage removal of biofilms from different locations in the IP space were obtained. Microcomputed Tomography (μ-*CT*) imaging was used to obtain 3D images of the typodont and the IP spaces. The shear stress distribution generated by the drop impacting the tooth surface was calculated by Computational Fluid Dynamics (CFD) simulations based on the finite element method (FEM). There was good agreement between experimentally measured biofilm removal and the pattern of predicted wall shear stress (τ_w) generated in the IP space by the microburst. High velocity water microdrops, with minimal fluid volume and time, effectively removed both the surrogate and the biofilm. The shear stress generated by the PT-*AirFloss* and its spatial distribution on the teeth surface played a key role in dictating the efficacy of biofilm removal. In addition, CFD models were used to predict optimal water drop or burst design with respect to more effective biofilm removal performance. Furthermore, the influence of fluid shear flow on the detachment of *Streptococcus mutans* biofilms inside microfluidic channels was studied using a commercially available flow-cell system. A critical biofilm detachment shear stress was estimated for the large biofilm-aggregates ($CDSS_{agg}$). The $CDSS_{agg}$ value was used in the CFD model to predict the spatial distribution of biofilm aggregates detachment from the IP surface caused by the PT-*AirFloss* microburst.

Next the effect of three biofilm matrix-degrading enzymes on the structure and detachment of *Streptococcus mutans* biofilms inside microtiter plates and on typodont teeth was studied experimentally. The enzymes used were: Bromelain (a protease), DNase, and RNase. The biofilms were treated with different enzymatic preparations, stained with Live/Dead and Crystal Violet, and the corresponding optical density (OD) and fluorescence intensity (FI) were measured by a microplate reader. The results detailed the degradation effect of each enzyme, separately and in combination. The three enzymes demonstrated different efficacies in degrading the biofilm in 6, 24 and 96 well-plates, as well as on the typodont teeth. Also, there was a large variability which could be explained by the heterogeneity of the biofilm. Using epifluorescence microscopy and image analysis, quantitative measurements of the percentage surface area coverage were obtained, and the preliminary results were consistent with the data

from the plate reader. Furthermore, pre-coating the plates with the three enzymes did not inhibit biofilm from formation and accumulation.

Lastly the use of a biocompatible copolymer of methylvinyl ether and maleic anhydride, with excellent mucosal adhesive properties and biocompatibility to improve enzymatic digestion by offering a prolonged contact of the enzymes with the teeth and oral tissues, was investigated. The rationale was to eliminate a major obstacle facing the efficacy of the enzymatic therapy which was the relatively short residence time of the enzymes at the site of administration. The adhesive copolymer could possibly enhance enzyme biofilm degradation. Combining the adhesive copolymer with the enzymes could potentially allow near total degradation of the laboratory-grown *S. mutans* biofilms.

Table of contents

ACKNOWLEDGEMENTS

I would like to express my deepest appreciation to everyone who helped me in the completion of this thesis. My supervisors, friends, family and wife: thank you!

First of all, I would like to express the deepest appreciation to my enthusiastic supervisor, Dr Paul Stoodley, who continually conveyed a spirit of ambition and excitement regarding research and teaching. The completion of this thesis would not have been possible without his persistent guidance and support. Thank you, Paul!

I would like to thank Philips Oral Healthcare (POH) for financially supporting my research for three years.

I would like to thank my other supervisors, Dr Philipp Thurner, Dr Julian Wharton, Dr Marcelo Aspiras, Dr Marko De Jager, and Dr Marilyn Ward for all the help and support, and for giving me the time whenever needed.

Many thanks to Dr Dario Carugo and Dr Lorenzo Capretto for their help with the computational work; Dr Maria Salta, Dr Jeremy Webb and Dr Xunli Zhang for the helpful discussions; and the late Dr Hans Schuppe for his help with the CSLM images.

I would like to thank Dr Stoodley's group members, Lianne, Natalya, and Stefania, as well as Dr Rob Howlin for the help and constructive comments.

I would like also to thank the amazing and sweet Dr Luanne Hall-Stoodley for the nice barbecues and cheerful hangouts.

I would like to thank all my Southampton friends for all the hangouts and fun time. They made my life in the UK very interesting.

I would like to thank the Faculty of Engineering and the Environment (FEE) and the national centre for advanced tribology at Southampton (nCATS) for all the support. I would also like to acknowledge the use of both the IRIDIS High Performance Computing Facility, and μ-VIS (CT centre), and associated support services at the University of Southampton, in the completion of this work.

I would like to thank my family for the overwhelming support and love. My parents, my two brothers and their families, and my sister: thank you!

Finally, a big “thank you” goes out to my amazing wife, Rim. She was always there for me to cheer me up and motivate me to keep going.

List of figures

Figure 4.1 A) Photograph showing the experimental setup for the uni-axial compression test. **B)** The diameter of the spherical sample of the dextran gel was estimated by comparing it to the known dimensions of a reference plunger tip.

Figure 4.2 A) Philips PT-*AirFloss* that was used to generate the microburst. **B)** Experimental setup used for studying the high velocity water impact on the dextran gel in the IP space of a typodont. **C)** The IP space used in the experiments viewed from the front and **D)** from the bottom (or top).

Figure 4.3 A) A representative load-versus-displacement plot for a *Streptococcus mutans* biofilm on a glass slide, showing the initial linear part followed by the curved region. **B**) The linear part of the plot (indicated by a best fit line) was used to estimate Young's modulus.

Figure 4.4 A representative force-relaxation curves for five different *S. mutans* biofilms.

Figure 4.5 Effect of nutrients, chelation, and osmotic pressure on the mechanics of *S. mutans* biofilms. **A)** Sucrose concentrations versus *E* of *S. mutans* biofilms. **B)** EDTA concentrations versus *E* of *S. mutans* biofilms. **C)** PEG-8000 concentrations versus *E* of *S. mutans* biofilms. Each data point represents the mean from three independent experiments (n = 5 in each, so n = 15 in total). Error bars indicate the standard deviation of the measurements (n = 15). One-way analysis of variance (ANOVA) and Tukey's honestly significant difference (HSD) test with a confidence level of 95% were used.

Figure 4.6 *E* of *S. mutans* biofilms as a function of hydrophobicity (measured by contact angle) of four different surface materials commonly used in dentistry or experimental models. Y-error bars indicate standard deviation (n = 5) and X-error bars indicate standard deviation (n = 3 for Ti and HA; n = 4 for SS and PE).

Figure 4.7 A) Three load-versus-displacement curves for the dextran gel. Panel **B)** A typical compression curve for dextran gel. Young's modulus was calculated by adopting Hertz theory for contact mechanics.

Figure 4.8 Three force-relaxation curves for the dextran gel representing repetitions of the test on the same sample.

Figure 4.9 Stack of consecutive images obtained by high-speed videography, showing the water, burst (stained with black food dye) from the PT-*AirFloss*. These images were used to calculate the velocity of the fluid exiting the PT-*AirFloss*. The total elapsed time was 1.8 ms (total number of frames = 29), corresponding to a travelled distance of 12 cm.

Figure 4.10 Stack of consecutive images obtained by high-speed videography, showing the PT-*AirFloss* burst (in the direction of the white arrow) impacting the IP space between the central incisors of the typodont, where the dextran gel was applied. These images were used to calculate the breaking strain of the surrogate. The white marks (x) represent the leading edge of the artificial plaque.

Figure 5.1 A) The Frasaco training typodont. B) Micro-CT image of the typodont of the upper jaw.

Figure 5.2 Experimental set-up and the position of each of the PT-*AirFloss*, high speed camera and light source with respect to the typodont.

Figure 5.3 CAD-based 3D rendering of the IP space.

Figure 5.4 A) The 3D meshwork showing the geometry of the proximal surface of the tooth (small panel) that was used for the computational simulations. B) Positioning of the PT-*AirFloss* with respect to the meshwork. ANSYS software was used to run the simulations.

Figure 5.5 Mesh independence study. The percentage area of the tooth where the fluid shear stress was > 1.7 Pa ($A_{1.7}$) was calculated at various mesh element sizes, between 0.125 mm and 0.25 mm. The onset of a plateau was detected at the mesh element size of 0.155 mm, which was selected for the numerical simulations described below.

Figure 5.6 Design of different nozzle tip shapes for comparative evaluations. (a) Circular, (b) Elliptical, (c) Square and (d) Triangular cross-sections (blue) were designed for this purpose and meshed with triangular elements for flow dynamic investigations.

Figure 5.7 Transmitted light images of *S. mutans* biofilms inside the microfluidic channels. The three images were taken, using the EVOS microscope with the 10 × objective, from three different channels. The large biofilm-aggregates are labelled "lba". Scale bars = 200 μm.

Figure 5.8 Microscopic images from a time-lapse sequence captured using transmitted light mode, of a *S. mutans* biofilm inside microchannels. The biofilm aggregate in the above images was exposed to an increased fluid shear stress, and the black arrow indicates the flow direction in the channel. As the sequence progresses, a small part of the cluster detached first, then the whole aggregate begin to roll and detach at 0.3 Pa for this particular sequence. Scale bar = 100 μm.

Figure 5.9 Percentage area coverage of the biofilm versus the shear stress (Pa). The percentage coverage was obtained by analysing selected images from the video sequences, using ImageJ. The lower curve (triangles) corresponds to the sequence in Figure 5.8 where the main detachment happened at a shear stress of 0.3 Pa, while the two upper curves correspond to other sequences where the main detachment occurred at 1.0 and 1.7 Pa, respectively. The three black arrows point to the part on each of the three corresponding curves where the main detachment event occurred. The different values obtained for the critical shear stress were used in our CFD simulations.

Figure 5.10 Stack of consecutive high speed images showing the PT-*AirFloss* burst (in the direction of the white arrow) impacting the IP space between the central incisors of the typodont, where the dextran gel was applied. The images show the mechanism of adhesive detachment from the tooth surface.

Figure 5.11 (a) Contours of τ_w distribution over the tooth surface, as determined from CFD simulations, with y being the location on the proximal side, starting from the labial to the lingual side. The vertical coloured scale on the left represents the values for the shear stress obtained by the simulations. (b) The y-axis represent the τ_w values (in kPa) along the tooth (or y/L on the x-axis, where L being the fixed distance from the labial to the lingual side) at a fixed nozzle tip z-position (z/H = 0.5). The black squares in (a) correspond to the ones in (b).

Figure 5.12 Effect of nozzle tip z-position (z/H) on τ_w spatial distribution over the tooth surface. The tip cross-section was circular with a diameter of 1.1 mm, and z/H was varied between 0.17 and 0.83 (a-c). The red arrow indicates the flow direction. The red area in (d-f) corresponds to the tooth surface area where τ_w is lower than $CDSS_{agg}$ = 1.7 Pa, for the different z-positions investigated.

Figure 5.13 Effect of nozzle z-position on the hydrodynamics within the interproximal space. Distributions of streamlines at z/H = 0.17 (a), 0.5 (b) and 0.66 (c) are reported. Streamlines correspond to the trajectories of massless particles released from the nozzle tip (i.e., inlet). Corresponding τ_w distributions on the tooth surface are shown in panels (d), (e) and(f).

Figure 5.14 Effect of nozzle tip shape on τ_w spatial distribution over the tooth surface. The red area corresponds to the tooth surface area where τ_w is lower than $CDSS_{agg}$ = 1.7 Pa, for the different tip shapes investigated (at a fixed z-position, z/H = 0.5).

Figure 5.15 (a) Percentage of tooth surface area where the fluid τ_w was > $CDSS_{agg}$ = 1.7 Pa ($A_{1.7}$), at different z-positions of the circular nozzle tip. (b) $A_{1.7}$-z/H trend for the different tip cross-sectional shapes investigated. (c) Calculation of the reliability factor (ϕ) defined as the surface area bounded by the $A_{1.7}$-z/H curve. (d) Reliability factor for the different tip cross-sectional shapes investigated. Values were normalised with respect to ϕ_{circle}.

Figure 6.1 (A) Photograph showing the typodont teeth (8 and 9) in a 6-well plate. Fresh media and a new bacterial inoculum were added daily, for 7 consecutive days, to grow the biofilm in the IP space. (B) Position of PT-*AirFloss* with respect to the typodont facing the labial side of the teeth. The photo has been rotated 180^{o} to show the position as it would be when applying the PT-*AirFloss* against the teeth of the maxillary dental arch in actual use.

Figure 6.2 Representative CLSM images of *S. mutans* biofilm on five different locations (A, B, C, D, and E) across the IP space at the level of the prototype *AirFloss* tip from the proximo-labial to the proximo-palatal side of a maxillary central incisor (the five locations are identified clearly in Figure 3). A_1, B_1, C_1, D_1 and E_1 are the images for the biofilm before the burst (on the untreated tooth), and A_2, B_2, C_2, D_2 and E_2 are the corresponding images after thresholding using ImageJ (the biofilm is in black in these images, while the white areas are biofilm-free regions). Meanwhile, A_3, B_3, C_3, D_3 and E_3 are the images for the biofilm on the treated tooth after the burst, and A_4, B_4, C_4, D_4 and E_4 are the corresponding thresholded images. The untreated samples (columns 1 and 2) and treated samples (columns 3 and 4) are not from the same specimens. The % removal was calculated by subtracting the amount of biofilm that remained after from the original amount of biofilm.

Figure 6.3 High speed camera frames show the removal of a *S. mutans* biofilm from the IP space under the influence of high velocity water droplets. Image analysis was used to subtract the "before burst" image in panel A from the "after burst" image in panel B. The result is shown in panel C. The biofilm that had detached (dashed red line in A) was quantified for four different videos, using ImageJ software.

Figure 6.4 (A) High speed video frames showing the detachment of a *S. mutans* biofilm from the IP space between the two upper central incisors. The major part of the aggregate was removed within 20 ms, and almost all of it was removed within 33 ms. The images show the elongation of the biofilm before detachment. **(B)** Four curves from four different videos for the percentage reduction of the surface area coverage of the biofilm over time.

Figure 6.5 % Removal of the biofilm quantified from the CLSM images at different locations on the tooth surface in the IP space. The schematic drawing (right) shows the proximal view of the upper central typdont incisor. The black squares represent the different locations where the CLSM images were taken to quantify biofilm removal.

Figure 6.6 (a) Contour map showing the spatial distribution of the fluid shear stress on the tooth surface (colour distribution), as calculated from numerical simulations (circular nozzle tip; z/H = 0.5). (b) τ_w on the tooth surface (in kPa) at different y-positions along the tooth (i.e. from labial to palatal side), at a fixed z-position (gingivo-incisal), as also calculated from numerical simulations. Empty squares correspond to the measurement points (squares) in (a). On the secondary y-axis, the percentage of biofilm removal measured experimentally in Figure 6.5 is plotted, with the 5 empty circles (denoted as A, B, C, D, and E) correspond to the same positions in the two figures.

Figure 6.7 Relationship between biofilm percentage removal (determined experimentally) and τ_w on the tooth surface (determined computationally). Data points were interpolated with a linear trend (red line).

Figure 7.1 Live/Dead fluorescence images of *S. mutans* biofilms grown in plates. Four images (A, B, C and D) were from different wells that were used as control (biofilm only), and were later used as controls to compare with images taken for enzyme-treated biofilms. Scale bar = 200 μm.

Figure 7.2 Figure 7.2 Final OD values for the three different enzymes, the control (biofilm only), and the combination of the three enzymes. The values represent two experimental runs (n = 4 in each). The bar graphs represent the average (± standard deviation in error bars). The two enzymes were sequentially added to the biofilm and incubated with 1 hour in between and two rinses with PBS or water after each enzyme application. All the 6 treatments had the same number of rinses.

Figure 7.3 Fluorescence intensity values (L/D) for the three different enzymes, and the control (biofilm only), for two independent experiments (n = 4 in each). The bar graphs represent the average (± standard deviation in error bars). The three enzymes and the control had the same number of rinses with PBS or water.

Figure 7.4 Final OD values (for Crystal Violet staining) for the three different enzymes, the control (biofilm only), and the combination of 3 enzymes. The values are for two independent experiments (n = 4 in each experiment). The error bars represent the standard deviation from the mean.

Figure 7.5 Fluorescence intensity values (L/D) for the three different enzymes, the three different combinations of the enzymes, and the control (biofilm only). The data are for two independent experiments (n = 5-11 in each experiment). Live1/Dead1 represents the data for the first run, while Live2/Dead2 represents the data for the second run. The error bars represent the standard deviation from the mean. The number of rinses was accounted for. The enzymes are applied following the sequence shown in the graph (e.g. DNase + Rnase + Bromelain means that DNase was applied first, followed by Rnase, and then Bromelain).

Figure 7.6 Final OD values for two biofilms (24 h and 48 h) stained with Crystal Violet (n = 5-11). The error bars represent the standard deviation from the mean. The plot includes the values for the treatments with the three different enzymes, the three combinations of the enzymes, and the control (biofilm only). The OD values for the 48 hr. biofilm (red) are overall higher than those for the 24 hr. biofilm (blue). However, the effect of the enzymes is comparable and follows similar trend for both biofilms.

Figure 7.7 Microscopic images showing a *S. mutans* biofilm on a typodont tooth A) before and B) after enzymatic treatment with Bromelain. The image was taken by EVOS microscope with the 20 × objective. The vertical (A) and horizontal (B) scale bars = 200 µm.

Figure 7.8 Live/Dead fluorescence images of *S. mutans* biofilms grown in wells treated with different enzymes. A) DNase B) Bromelain C) RNase D) Combination of

the enzymes Bromelain + (RNase and DNase). Two images for each treatment are shown here to demonstrate the heterogeneity of biofilms even when grown under the same conditions. The images were compared to the control images in Figure 7.1. Scale bar = 200 µm.

Figure 7.9 Low power microscopic images showing: the control (A), and the Bromelain-treated (B) wells. Each image is made of 5 images that were taken from the: centre, left, right, bottom and top sides of the well and put together. Scale bar = 1000 µm.

Figure 7.10 Percentage of surface area coverage of the biofilm in the 96-well plates. The values were obtained from the analysis of the EVOS microscopic images, and they represent an average of two image analysis methods (n = 7 in each).

Figure 7.11 Transmitted microscopic images of *S. mutans* biofilms grown in 24-well plates. Image A was taken for a biofilm grown in a well that was pre-coated with DNase enzyme, while image B was taken for the control well (no enzymatic coating, only biofilm). Both images showed complete biofilm coverage. Scale bar = 200 µm.

Figure 7.12 Biofilm surface coverage versus time after addition of the protease Bromelain. The biofilm was grown on a hydroxyapatite disc.

Figure 7.13 Biofilm surface coverage versus time, showing the degrading effect of an enzyme (Bromelain) on the biofilm, both alone and in the presence of the adhesive copolymer, where: B+PBS (biofilm+PBS = control 1)**,** B+Gtrz (biofilm+Gantrez = control 2)**,** B+Brom (biofilm+Bromelain)**,** B+Brom/Gantrez (biofilm+Bromelain/Gantrez mixture).

Figure 7.14 Biofilm surface coverage versus time, showing that the adhesive copolymer maintaining the effect of the enzyme for prolonged periods of time (triangles) when compared to the use of enzyme alone without the adhesive copolymer (crosses X).

List of tables

Nomenclature

AF	*AirFloss*
AFM	Atomic Force Microscopy
ANOVA	Analysis of Variances
ATCC	American Type Culture Collection
BHI	Brain Heart Infusion
BHI+S	Brain Heart infusion + Sucrose
CD	Compact Disc
CFD	Computational Fluid Dynamics
CLSM	Confocal Laser Scanning Microscopy
CT	Computed Tomography
CV	Crystal Violet
DAPI	4', 6-diamidino-2-pheylindole
DPBs	Dental Plaque Biofilms
DPBBs	Dental Plaque Bacterial Biofilms
EDTA	Ethylene-diamine-tetraacetic acid
EPS	Extrapolymeric Substances
EtOH	Ethanol
FEM	Finite Element Method
HA	Hydroxyapatite
IP	Interproximal
KPa	Kilo-Pascal
MPa	Mega-Pascal
nCATS	National Centre for Advanced Tribology at Southampton
OD	Optical Density
Oh	Ohnesorge's Number
Pa	Pascals
PBS	Phosphate Buffered Saline
PE	Polyethylene
PEG	Polyethylene Glycol
PI	Propidium Iodide
PMMA	Polymethylmethacrylate
PMT	Photomultiplier Tube

PPM	Part Per Million (μg mL^{-1})
PT	Prototype
Re	Reynolds Number
RFU	Relative Fluorescence Units
SS	Stainless Steel
S9	SYTO9
Ti	Titanium
τ_w	Wall Shear Stress
u_{exit}	Exit Velocity
UHMW	Ultra high molecular weight
VOF	Volume of Fluid
We	Weber's Number
μ-CT	Microcomputed Tomography

Presentations of the research embodied in the thesis

A. Rmaile, D. Carugo, L. Capretto, X. Zhang, P.J. Thurner, J. Wharton, M. Aspiras, M. Ward and P. Stoodley. "Mechanical Properties and Disruption of Dental Biofilms" Abstract submitted for a **Poster** presentation at the **Life Sciences Conference** in Southampton, UK (12th of September 2011).

A. Rmaile, D. Carugo, L. Capretto, X. Zhang, P.J. Thurner, J. Wharton, M. Aspiras, M. De Jager and P. Stoodley. "Mechanical Properties and Disruption of Dental Biofilms" Abstract submitted for an **Oral** presentation at the **17th Postgraduate PG conference** in Southampton, UK (October 2011).

A. Rmaile, D. Carugo, L. Capretto, X. Zhang, P.J. Thurner, J. Wharton, M. Aspiras, M. Ward and P. Stoodley. "Mechanical Properties and Disruption of Dental Biofilms" Abstract was submitted for an **Oral** presentation at the **Life Sciences internal seminar series** in Southampton, UK (November 2011).

A. Rmaile, D. Carugo, L. Capretto, X. Zhang, P.J. Thurner, J. Wharton, M. Aspiras, M. Ward and P. Stoodley. "Mechanical Properties and Disruption of Dental Biofilms" Abstract was accepted for a **Poster** presentation at the **Set for Britain (SfB) award competition** at the House of Commons in London, UK (March 2012).

A. Rmaile, D. Carugo, L. Capretto, X. Zhang, P.J. Thurner, J. Wharton, M. Aspiras, M. Ward and P. Stoodley. "Mechanical Properties and Disruption of Medically-Related Bacterial Biofilms" Abstract was accepted for an **Oral** presentation at the **4th UK - China Tribology symposium** Lubricated and Chemical Aspects of Wear, Southampton, UK (29th - 30th of March 2012). This presentation title was modified to "Microbial Antifouling in Medicine and Industry: Disruption of Bacterial Biofilms".

A. Rmaile, D. Carugo, L. Capretto, X. Zhang, P.J. Thurner, J. Wharton, M. Aspiras, M. Ward and P. Stoodley. "Mechanical Properties and Disruption of Dental Biofilms" Abstract was submitted for a **Poster** presentation at the **22nd European Congress of Clinical Microbiology and Infectious Diseases (ECCMID)** in London, UK (31st of March - 3rd of April, 2012).

A. Rmaile, D. Carugo, L. Capretto, X. Zhang, P.J. Thurner, J. Wharton, M. Aspiras, M. Ward and P. Stoodley. "Mechanical Properties and Disruption of Dental Biofilms" Abstract was accepted for a **Poster** presentation at the **IBBS conference** in Winchester, UK (11^{th} - 12^{th} of September 2012).

A. Rmaile, D. Carugo, L. Capretto, X. Zhang, P.J. Thurner, J. Wharton, M. Aspiras, M. Ward and P. Stoodley. "Utilizing High Velocity Water µ-Drops to Disrupt Dental Biofilms" Abstract was accepted for an **Oral** presentation at the **6^{th} ASM meeting** in Miami, USA (October 2012).

A. Rmaile, D. Carugo, L. Capretto, X. Zhang, P.J. Thurner, J. Wharton, M. Aspiras, M. Ward and P. Stoodley. "Effect of Mechanical Stress on Dental Biofilms: A Uni-axial Compression Study" Abstract was accepted for a **Poster** presentation at the **6^{th} ASM meeting** in Miami, USA (October 2012).

A. Rmaile, D. Carugo, L. Capretto, X. Zhang, P.J. Thurner, J. Wharton, M. Aspiras, M. Ward and P. Stoodley. "Utilizing High Velocity Water µ-Drops to Disrupt Dental Biofilms" Abstract submitted for a **Poster** presentation at the **1^{st} Postgraduate PG conference** in Southampton, UK (7^{th} of November, 2012).

A. Rmaile, D. Carugo, L. Capretto, X. Zhang, P.J. Thurner, J. Wharton, M. Aspiras, M. Ward and P. Stoodley. "Utilizing High Velocity Water µ-Drops to Disrupt Dental Biofilms" Abstract submitted for a **Poster** presentation at the **Biofilms 5 meeting** in Paris, France (10^{th} - 12^{th} of December, 2012).

A. Rmaile, D. Carugo, L. Capretto, M. Aspiras, M. Ward and P. Stoodley. "Utilizing High Velocity Water µ-Drops to Disrupt Interproximal Dental Biofilms" Abstract was accepted for a **Poster** presentation at the **IADR meeting** in Seattle, USA (March 2013).

A. Rmaile, D. Carugo, L. Capretto, M. Aspiras, M. Ward and P. Stoodley. "Disruption of Dental Plaque Bacterial Biofilms by Matrix-Degrading Enzymes" Abstract was

accepted for a **Poster** presentation at the **IADR meeting** in Seattle, USA (March 2013).

A. Rmaile, D. Carugo, L. Capretto, M. Aspiras, M. Ward and P. Stoodley. "Mechanical Characterization of the Viscoelastic Dental Plaque Bacterial Biofilms" Abstract was accepted for a **Poster** presentation at the **IADR meeting** in Seattle, USA (March 2013).

A. Rmaile, M. Aspiras, M. Ward and P. Stoodley. "Disruption of Dental Biofilms by Matrix-Degrading Enzymes" Abstract was accepted for an **Oral** presentation at the **BSODR meeting** in Bath, UK (9^{th} - 11^{th} of September, 2013).

A. Rmaile, D. Carugo, L. Capretto, M. Aspiras, M. Ward and P. Stoodley. "An Experimental and Computational Study of the Hydrodynamics of High-Velocity Water Drops for the Inter-Dental Cleaning" Abstract was accepted for a **Poster** presentation at the **Eurobiofilms meeting** in Ghent, Belgium (9^{th} - 12^{th} of September, 2013).

Papers of the research embodied in the thesis

A. Rmaile, et al., Microbial tribology and disruption of dental plaque bacterial biofilms, *Wear* (2013), http://dx.doi.org/10.1016/j.wear.2013.02.010

A. Rmaile, et al., An Experimental and Computational Study of the Hydrodynamics of High-Velocity Water Drops for the Inter-Dental Cleaning. (Manuscript is in preparation. To be submitted soon)

A. Rmaile, et al., Removal of Interproximal Dental Plaque Biofilms by High-Velocity Water Microdrops, *Journal of Dental Research* (2013, in press)

A. Rmaile, et al. Utilizing Fluids Hydrodynamics for the Detachment and Disruption of Dental Plaque Bacterial Biofilms (Invited review to be submitted to "Journal of Medical Microbiology")

A. Rmaile, et al. Dispersal of *Streptococcus Mutans* Biofilms by Matrix-Degrading Enzymes (Manuscript is in preparation)

Declaration of authorship

I, Amir Rmaile, declare that this thesis entitled "**Mechanical properties and disruption of dental biofilms**" is an account of the work carried out by me as part of the national Centre for Advanced Tribology, Southampton (nCATS), Engineering Sciences, Faculty of Engineering and the Environment, University of Southampton, UK.

The work presented in this thesis is my own, and has been generated by me as the result of my own original research. I confirm that:

- This work was done wholly or mainly while in candidature for a research degree at this University;
- Where any part of this thesis has previously been submitted for a degree or any other qualification at this University or any other institution, this has been clearly stated;
- Where I have consulted the published work of others, this is always clearly attributed;
- Where I have quoted from the work of others, the source is always given. With the exception of such quotations, this thesis is entirely my own work;
- I have acknowledged all main sources of help;
- Where the thesis is based on work done by myself jointly with others, I have made clear exactly what was done by others and what I have contributed myself;
- Parts of this work have been published as: see pages 15-18

Signed: ……..

Date: 30-07-2013

Chapter 1

1. General introduction

Dental plaque biofilms are defined as communities of microbial cells in the oral cavity that are embedded in an extracellular polymeric matrix [1] [2]. Dental plaque affects all humans worldwide. Failure to deal with plaque in the stage of early formation leads to the development and persistence of more severe diseases and health complications. Oral biofilms are among the most complex microbial communities in nature and are known to cause dental caries, gingivitis and periodontitis, and are also associated with low birth weight and endocarditis [3].

In the US, dental caries, or tooth decay, which is the direct outcome or result of accumulated dental biofilm (plaque), is the most common chronic childhood disease. According to the 2000 U.S. Surgeon General's report on oral health, dental caries was reported to be at least five times more common than asthma [4]. Worldwide, most children and an estimated 90 % of adults have experienced caries at different stages in their life [5]. Dental caries is caused by a number of pathogenic bacteria in the oral cavity. These bacteria, after accumulation, lead to the formation of dental plaque biofilms which could cause the inflammation of various tissues surrounding the teeth in the oral cavity: gingivitis (inflammation of gingival or gum tissue), periodontitis (inflammation of the periodontal ligament) [6], or osteomyelitis (inflammation of the bone marrow or bone tissue) [7]. These conditions are often accompanied by discomfort, pain, and infections. Total or partial tooth, or tooth material, loss is a common outcome of such cases. In severe and totally neglected cases, death could be the outcome. Periodontitis, for example, must always be highly considered as a significant risk factor for many systemic, and multi-factorial, diseases such as: cardiovascular diseases (endocarditis, myocardial infection, and angina pectoris), pulmonary infections, diabetes mellitus, stroke, brain abscess, and difficulties during pregnancy (premature birth, low birth weight, increased infant mortality) [8]. Thus, it

is crucial that these bacteria are kept under control in the oral cavity. The ideal way to achieve this purpose is to prevent the accumulation of the bacteria by preventing the first and primary steps of its existence: prevention of dental plaque biofilm formation by detaching it, or its most vital components, in the very early stages of attachment to the tooth surface. In order to achieve this goal, there should be a thorough understanding of the behaviour of these biofilms, an extensive study of their mechanical properties, and the development of novel ways to detach them accordingly.

While high percentages of *Streptococcus mutans* have been recovered from people with no carious lesions, and incidences of caries have been found without *S. mutans*, this acid-producing bacterium is widely accepted as one of the most significant etiologic agents in caries development. And while the contributions of all plaque flora must be considered when discussing the ecological nature of the development of caries, *S. mutans* have had strong association with caries development [9]. Although cariogenicity of *S. mutans* is due to several properties, the ability to form biofilm in the presence of dietary sugars is a crucial step in the development of caries. *S. mutans* causes the most damage to teeth in the presence of fermentable sugars such as sucrose, glucose or fructose [10] [11] [12]. *In vitro* biofilms grown from *S. mutans* were used in this experimental research to model an early stage cariogenic human dental plaque. This biofilm model has been widely used in research to study attachment, growth and mechanical properties, with the aim of developing novel detachment or disruption strategies [13] [14] [15]. It is crucial to extensively study such properties because they highly influence how biofilms will respond to external forces, cell dispersal and detachment from biofilms, and mass transfer into biofilms. A fundamental understanding of the mechanical properties of dental biofilms is required to help design more effective strategies for the manipulation and control of biofilm strength through physical, chemical and enzymatic targeting of the EPS matrix. Such an extensive knowledge can be beneficial for modelling of biofilm behaviour and development, for making predictions regarding treatment efficacy and the development of new medications.

Chapter 2

2. Aims, objectives and thesis structure

2.1. Aims and objectives

The first aim of this project was to fundamentally characterize the mechanical properties of biofilms grown from *Streptococcus mutans* bacteria while kept in a hydrated state. The main focus was on the viscoelastic parameters and fluid shear stress induced failure mechanism (i.e. both cohesive and adhesive failures) of biofilms. The second aim was to employ several biofilm detachment, alteration or disruption strategies, which might be used independently or in compliment to fluid forces. These strategies were based on chemical, mechanical/physical or enzymatic manipulation. The work was completed using *Streptococcus mutans* UA159 strain, American Type Culture Collection ATCC no. 700610 (www.atcc.org). *S. mutans* is one of the early colonizers of tooth surfaces along with other viridans streptococci and oral lactobacilli, and is not the most common species of research interest because of its cariogenicity. *S. mutans* UA159 is also well characterized and is used as a model biofilm former in many research studies [15] [16].

The aims were addressed by:

1. Growing *S. mutans* biofilms in the laboratory and measuring their mechanical properties (the elastic modulus and stress relaxation) using uniaxial compression techniques. This step was complemented by using Confocal Laser Scanning Microscopy CLSM and thus relating mechanical properties to structural changes (first aim). Secondly, the mechanical properties of the biofilm were manipulated by changing the concentrations of nutrients in the media (e.g. sucrose), or chemically cross-linking them to chelators (e.g. EDTA), or cations (single or multivalent), osmotic pressure stress agents (e.g. PEG). The influence these agents have on the biofilm mechanical properties were determined (second aim).

2. Using fluid flow delivered through a device to study the detachment of dental plaque biofilms using artificial biofilms on a testing model first, then real biofilms. A computational fluid dynamics CFD model was used to calculate the shear stresses generated around a tooth geometry using ANSYS Fluent software for comparison with experimental results. Using the micro-CT scanning technique, 3D simulations were obtained (first and second aims).

3. Disruption of biofilms, either mechanically by the use of oral healthcare devices (e.g. *AirFloss* or *Waterpik*), or by the enzymatic digestion of the EPS components (second aim):

    - Use specific staining to quantify the distribution of matrix components by CSLM, before and after treatment

    - Use Live/Dead staining to determine effect on structure and viability of any remaining biofilm

    - Use Crystal Violet Staining to quantify biofilm formation and degradation

2.2. Thesis structure

This thesis consists of nine chapters. The literature review can be found in Chapter 3 summarizing the current state of knowledge and scientific aspect related to this study. This chapter was divided into sections that were relevant to the current project such as i) dental biofilms formation, progression, detachment, and hydrodynamics ii) mechanical properties of biofilms, iii) methods to measure mechanical properties of biofilms, iv) *Streptococcus mutans* biofilms, v) hydrodynamics of high-velocity water µ-drops in the interproximal dental sites vi) computational fluid dynamics, and vii) enzymatic degradation of biofilms.

Chapters 4, 5, 6, and 7 were written in paper format since they were, or will, be submitted as manuscripts for publication in journals, where each chapter has its own introduction, materials and methods, results, discussion, conclusion and references sections. Some repetition may occur in these chapters when the same or similar techniques or methods were used.

In Chapter 4, the mechanical properties of both surrogate plaque and *S. mutans* biofilms were tested by uniaxial compression. Also, the effect of different factors on the biofilm strength was investigated. This chapter has already been published as a research paper in Wear Journal [17].

In Chapter 5, the hydrodynamics of high-velocity water µ-drops in the interproximal dental sites were studied experimentally and computationally using a surrogate plaque.

In Chapter 6, the prevention of IP dental biofilms build-up by high-velocity water µ-drops was studied. The study on *S. mutans* biofilms was based on the results obtained from the previous chapter. Chapters 5 and 6 were written as two manuscripts, one has already been submitted for publication in the "Journal of Dental Research", and the second will be submitted soon. The computational simulations reported in these two chapters were run with the help of Dario Carugo and Lorenzo Capretto.

In Chapter 7, the dispersal of *S. mutans* biofilms by matrix-degrading enzymes was investigated using different enzymes, and under different conditions. The data in this chapter are mainly preliminary results that need to be investigated further in future studies.

In Chapter 8, the overall conclusions obtained from this work are summarized.

Finally, suggested future work was presented in Chapter 9.

2.3. Novelty

The novelty of the present work lies in:

- The development of a model system to investigate the cleaning of dental biofilms using high velocity water drops with high speed imaging to elucidate and quantify the cleaning mechanisms. The experimental model was designed to be compatible with confocal microscopy to provide high resolution end point data for assessing efficacy of the cleaning process.

- The development of calcium cross-linked dextran gel that could be used as a surrogate to replace real dental plaque bacterial biofilms for rapid screening and for use in non-microbiological research settings.

- The recreation of a realistic geometry associated with the IP space by growing *S. mutans* biofilms on typodont and baby human teeth.

- The utilization of μ-CT to image the typodont in 3D and construct a model of the IP space that was used in subsequent CFD modelling.

- The utilization of CFD to calculate the shear stress distribution, caused by water drops generated from an oral hygiene device, on the tooth surface. ANSYS Fluent, the widely-used and well validated software, was used for that purpose.

- The estimation of a critical hydrodynamic shear stress required for *S. mutans* biofilm-aggregates detachment, which was used as a model input parameter for predicting the spatial distribution of biofilm removal.

- The determination of a direct numerical relationship between the fluid wall shear stress (τ_w) and biofilm detachment by comparing the values obtained from the numerical simulations for τ_w to the values obtained from laboratory experiments for the percentage removal of biofilms.

- The application of different combinations of matrix-degrading enzymes to disrupt or degrade *S. mutans* biofilms.

- The utilization of a film-forming adhesive copolymer which could potentially offer a prolonged contact of the enzymes with the teeth and oral tissues.

Chapter 3

3. Literature review

3.1. Biofilms

Microbial cells surrounded by extracellular polymeric substance (EPS) constitute communities that are known as biofilms [18]. Cells found in biofilms are protected against external physical and chemical attacks, such as antimicrobial agents and disinfectants, and have higher possibilities of survival in low-nutrient conditions than planktonic cells. Biofilms readily form on different surfaces and interfaces, and therefore biofilms are considered a preferred way of microbial existence.

The biofilm develops when bacterial cells come close to a surface and attach. Next, the cells proliferate utilizing sugars and nutrients from consumed food and produce a complex extracellular matrix that binds the cells to each other and to the surface [19]. Two fundamental characteristics are exhibited by bacteria within biofilms: production of an extracellular polymeric substance (EPS) matrix and increased resistance to antimicrobial treatment. The EPS usually consists of polysaccharides, proteins and DNA, depending on bacterial species in the biofilm [20] [21]. The EPS matrix, a hydrated sticky framework, is a collection of biopolymers that are usually produced by the bacteria themselves. This matrix represents the most common feature of all biofilms known to humans, and is essential for the formation of any biofilm as it provides structural integrity and enhanced resistance of the biofilm to various antimicrobial agents and environmental factors that might cause the biofilm disruption, removal, or disintegration. The matrix provides mechanical stability of biofilms, facilitates their adhesion to surfaces, and forms a three-dimensional polymeric network that immobilizes the biofilm bacterial cells and provides them with inter-communication means. While the microbial cells account for less than 10 % of the biofilm dry mass, the matrix can account for over 90 % of that mass. The EPS composition varies significantly between biofilms, depending on bacterial species, shear forces present, and nutrients available within a certain environment. After initial

attachment and later on biofilm development, bacterial cells may undergo significant phenotypic shifts. Such transformations include induction of different metabolic pathways, decrease in cell division rates, and increase in resistance to antibiotic concentrations which are usually fatal to planktonic bacteria. Biofilm development and formation is crucial in understanding the extent of bacterial phenotypic activity in response to varying environmental conditions and various growth conditions [21].

In medical and dental fields, biofilms play an important role in the development and persistence of infectious diseases [22]. Biofilm formation is thought to be the reason behind about 60 % of the bacterial infections reported in developing countries [23]. Urinary tract, catheters, middle-ear, dental plaque, gingivitis, coating contact lenses, endocarditis, cystic fibrosis, permanent indwelling devices (joint prostheses, heart valves) are some examples of infections that are biofilm-based in the medical field [22]. Oral biofilms, also known as dental plaque [24], are among the most complex microbial communities in nature and are known to cause dental caries, gingivitis and periodontitis. They are widely studied as model systems for bacterial adhesion, biofilm development, and biofilm resistance to antibiotics, due to their widespread presence and availability [25]. Biomaterial-related infections occur when microorganisms colonize on medical devices, such as prostheses and implants as biofilms [26] [27].

3.2. Dental biofilms

3.2.1. Formation and progression

1) Pellicle formation

Within seconds after cleaning the teeth, salivary phosphoproteins, such as histatin and statherin, immediately adhere to the bacteria-free tooth surface due to their high affinity to hydroxyapatite (Figure 3.1). The formation of the conditioning film precedes the formation of a biofilm on teeth surfaces since organic molecules are transported faster to the surface than bacteria. This thin conditioning film is in fact a proteinaceous layer termed “the acquired enamel pellicle” [28]. Ionic interactions, van

der Waals forces, and in particular, hydrophobic interactions are the main forces behind the formation of this proteinaceous pellicle. This pellicle mediates and facilitates the interactions between the tooth surface, oral fluids and bacteria by altering the properties of the surface. The microorganisms interact directly with the constituent molecules of this thin film, which include adsorbed proteins (including enzymes), glycoproteins, and other macromolecules. The pellicle strongly affects surface properties, such as surface charge, wettability and surface free energy which has been shown to subsequently affect bacterial colonisation [29] [30] [31]. The second stage of dental plaque formation starts few minutes after the pellicle formation. Due to continuous adsorption of biomolecules from the oral fluids, the pellicle formation continues. Parotid protein aggregates, of 150 nm diameter and with a negatively charged surface layer, cause a fast increase of the pellicle's thickness within 30 – 120 min. The pellicle has multiple components that serve as specific receptors for bacterial adherence, and thus facilitates bacterial attachment to the surface. Some of these components include proline-rich proteins, amylase, lysozyme, Mucin MG 2, and fibrinogen. At this stage, adhesion is considered reversible or irreversible [32] [33] [34].

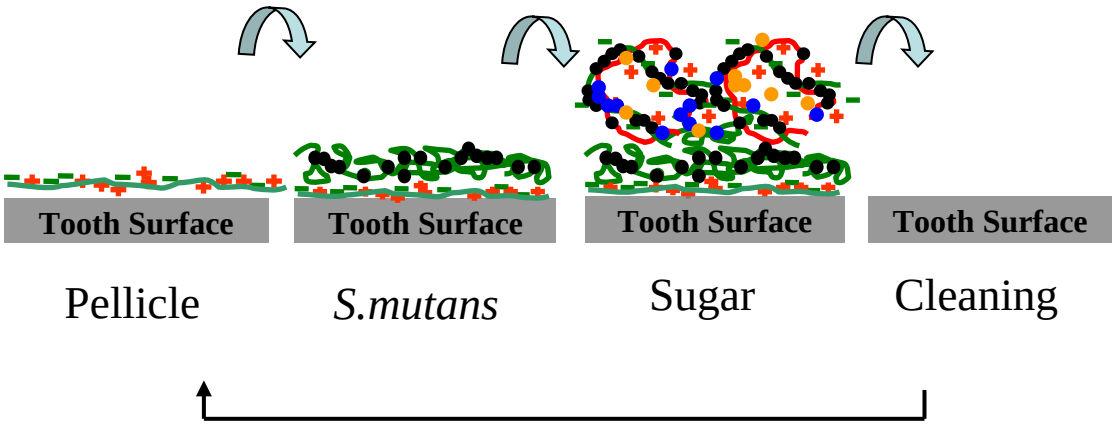

Figure 3.1 Process of dental plaque formation and attachment to tooth surfaces. The green line represents the salivary pellicle proteins, and the plus/minus signs represent the charges associated with the proteins. The black circles represent early bacterial colonizers such as *S. mutans*. The circles with other colours represent later bacterial colonizers that attach to already existing bacteria, after the latter make the

environment suitable for the former, usually in the presence of sugar which is utilized by *S. mutans* to produce acid. Daily oral hygiene procedures help remove the plaque and keep the tooth surface clean. This dynamic process takes place on a daily basis.

2) General Mechanisms of bacterial attachment

Bacterial adhesion to a hard substratum in general, and to the tooth surface in particular, is a multi-level process which includes cell transport, initial bacterial attachment (irreversible and reversible) followed by adhesion and colonisation of the surface by bacterial cells [19]. These steps are described briefly here.

i) Transport

Three different modes of transport define the initial movement of cells to a substrate: Brownian motion, active movement and convective motion (Figure 3.2).

a. *Brownian motion (diffusion):* Under no-flow conditions, the bacteria are passively transported by Brownian motion (average displacement = 40 μm h^{-1}) [35]. This motion allows their passage through the diffusion layer beyond which no convection exists. Transport by diffusion is several orders of magnitude slower than transport by convection.
b. *Active motion*: some bacterial species of the oral cavity bacteria are active swimmers [36], to allow movement on small spatial scale, demonstrating a chemotactic response towards a gradient (of small concentrations, 10^{-6} M) of chemical cues in the interfacial region [37].
c. *Convective motion*: Under fluid flow conditions, the bacteria are transported by this motion, which maybe faster than the Brownian motion by several orders of magnitude. But in certain cases the final step before encountering the surface (passage though the diffusion sub-layer) is diffusion controlled [38].

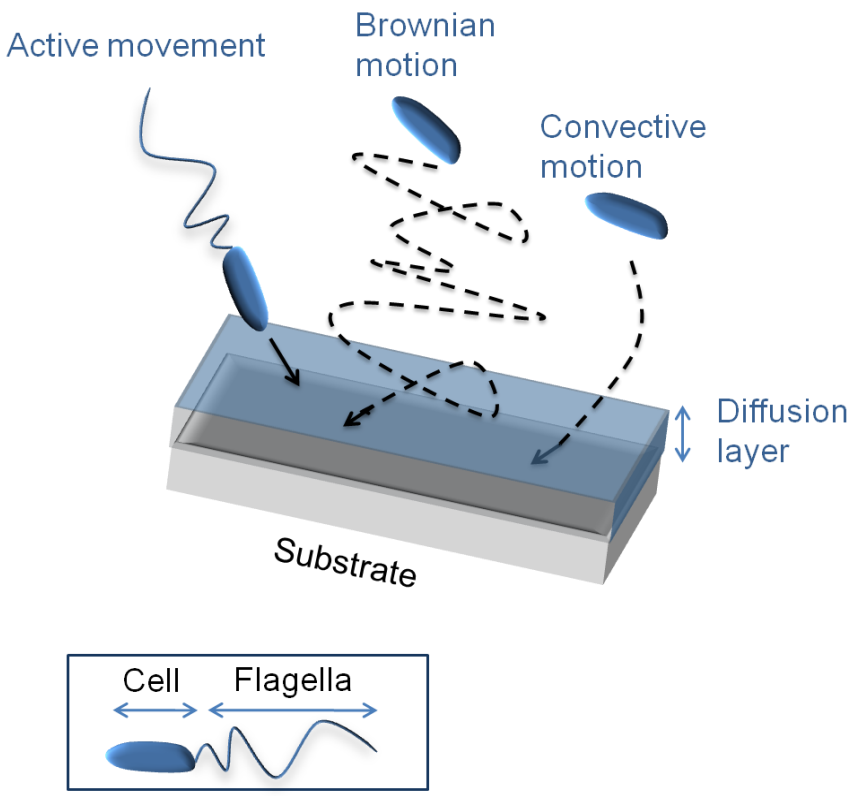

Figure 3.2 Bacterial cell transport mechanism on a substrate (courtesy of Dr. Maria Salta, and was originally adapted from Van Loosdrecht et al. 1990 [38]).

ii) Initial adhesion of bacteria

The main forces determining physical adhesion are electrostatic and dispersive (van der Waals) interactions [39] and the Derjagiun, Landau, Verwey and Overbeek (DLVO) theory [40] describes adhesion on the basis of these interactions. The DLVO theory, which was initially created to explain the behaviour of colloids, states that the total energy of any system made of two closely positioned surfaces equals the sum of the energies of their electrostatic and dispersive interactions. In order for adhesion to happen, the bacterium must be positioned at distances of either 10 - 15 nm or 0.5 - 1 nm, corresponding to secondary and primary energy minimum, respectively.

The ionic strength of the surrounding medium manipulates the total Gibbs free energy (G_{tot}) between the bacterium cell and the hard substratum. In low ionic strength conditions, the electric double layer is large thus electrostatic repulsion dominates and G_{tot} has a positive maximum preventing bacteria from adhering in the primary

minimum. In intermediate ionic strength conditions, the electric double layer decreases and the maximum G_{tot} is low enough for the bacteria containing sufficient thermal energy to overcome the barrier allowing for slow irreversible adhesion, with the aid of EPS and other bacterial cells components such as flagella, fimbrie and pilli [41] [35]. Under high ionic strength conditions, all bacterial cells can reach the primary minimum.

When the distance is between 10 - 15 nm, the shallower secondary minimum exists under the intermediate ionic strength conditions. Systems having a larger van der Waals attraction and larger particles, such as bacteria, demonstrate this shallower secondary minimum. Bacterial presence within the secondary energy minimum range does not ensure adhesion to the surface. Van der Waals interactions only slightly exceed the electrostatic repulsions in this case. The bacterium may be detached due to external alterations or bacterial locomotion. Adhesion is faster in the primary minimum area when the bacterium is less than 1 nm away from the surface. These energy minima (Figure 3.3) correspond to the reversible and irreversible forms of adhesion [42]. EPS and other cellular components such as flagella, fimbriae and pili [41] [35] may facilitate the adhesion of the cells "hovering'' on the surface to the underlying substrate.

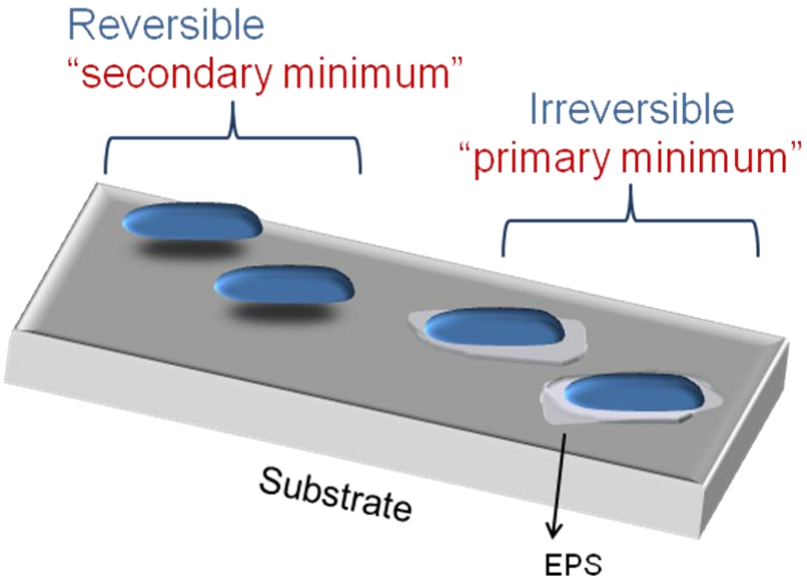

Figure 3.3 Initial bacterial adhesion on a substrate (courtesy of Dr. Maria Salta, and was originally adapted from Van Loosdrecht et al. 1990 [38])

iii) Bacterial attachment

After the irreversible adhesion, structures on the bacterial cell surface such as fimbriae, other proteins, lipo-polysaccharides (LPS), flagella, and EPS all have a role in bacterial attachment. Bacterial cell surface nonpolar polymers, such as fimbriae, play a major role in attachment to hydrophobic surfaces. EPS and LPS are more important in attachment to hydrophilic materials. Fimbriae help by overcoming the initial electrostatic repulsion barrier that exists between the bacterial cell and the substratum. Flagella play a role in attachment by overcoming repulsive forces rather than acting as adsorbents or adhesives [1] (Figure 3.4).

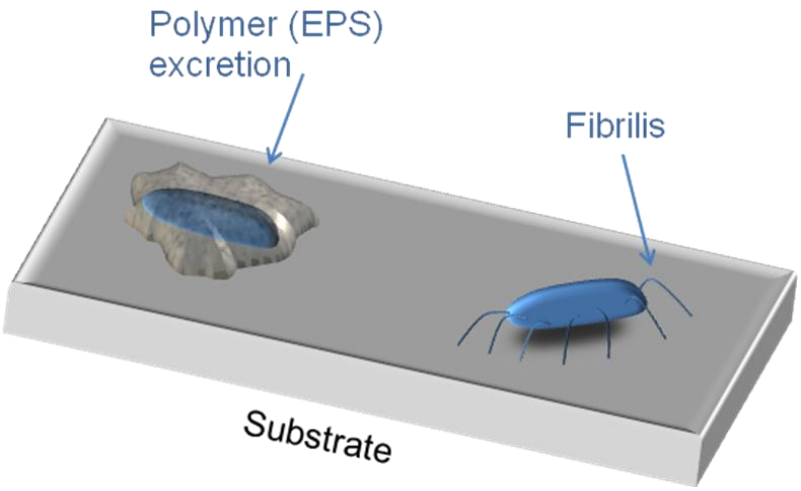

Figure 3.4 Bacterial attachment on surfaces (courtesy of Dr. Maria Salta, and was adapted from Van Loosdrecht et al. 1990 [38]).

iv) Biofilm growth

Bacterial cells exhibit several patterns of growth depending on attachment mode on a substrate. Bacteria are either irreversibly attached to the surface (*e.g.* EPS) but not to each other, forming a monolayer of cells on surface, or they irreversibly attached to the surface and to each other, resulting in a three-dimensional biofilm [38] (Figure 3.1).

One of the early colonizers, or pioneer bacterium, of the tooth surface is *Streptococcus mutans.* This Gram-positive, facultative anaerobic bacterium is considered a part of the normal human oral flora (Figure 3.5). The primary colonizers of dental biofilms [43], also including other viridans streptococci and oral lactobacilli, are of great significance in the later stages of biofilm formation and effect on the oral health of humans. *S. mutans* role in dental plaque formation and in tooth decay was described in more details in the next section. Biofilms grown *in vitro* from *S. mutans* were the study models that were discussed in this thesis and proposed for future experiments.

Streptococcus mutans

S. mutans is capable of growth by aerobic respiration if oxygen is present, but also capable of switching to fermentation in the absence of oxygen. *S. mutans* has gained significant interest in recent years because of its role in dental caries, or tooth decay (Figure 3.5) [44]. *S. mutans* is widely considered as a main etiologic agent in the development of dental caries.

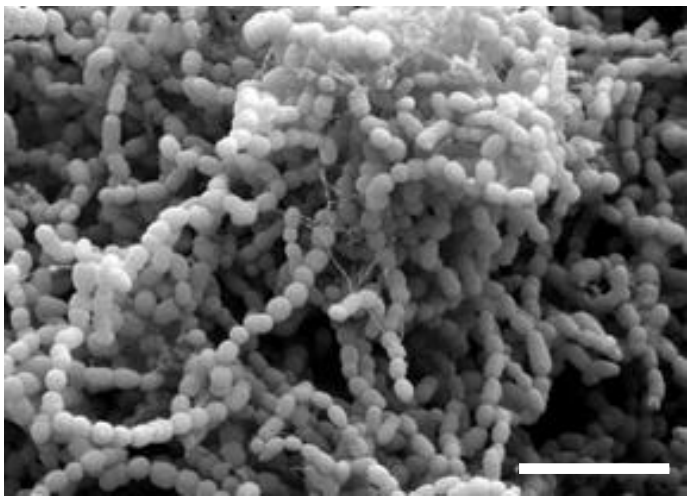

Figure 3.5 Scanning electron micrograph of *S. mutans* [45]. The scale bar is 5 µm.

This acid-producing bacteria cause the most damage to teeth in the presence of fermentable sugars, such as fructose, glucose and mainly sucrose [46]. Normally in the oral cavity, there is a dynamic and constant state of remineralisation and demineralization between teeth, which are primarily mineral in content (~ 98 % [wt / wt] hydroxyapatite [HA]), and saliva. Any decrease in the pH on the teeth surface below 5.5 will automatically trigger an increase in the demineralization rate over the remineralisation rate. This will lead to teeth decay. *S. mutans* ferments sugars into lactic acid, which increases the acidity on the teeth surface leading to demineralization of the teeth surfaces: enamel, dentine and cement [47]. The longer these bacteria remain attached to tooth surface, the more dissolution of minerals will take place, and the more the damage or decay will be. Once the demineralization progresses, enough mineral content will be lost, and the soft organic tissue will

disintegrate, which leads to cavities. The effect of lactic acid could be neutralized by using mouthwashes or fluoride toothpastes with water, which favours the remineralisation process [48].

S. mutans is a highly specialized organism that uses specific receptors on its bacterial wall to help in the adhesion to tooth surface. There receptors, or cell surface adhesins, facilitate the interactions with the acquired pellicle and primary colonizing bacteria. P1 antigen, also known as antigen I/II, Pac, MSL-1, SpaP, and antigen B [49], is the most important adhesin which binds to salivary glycoproteins [50]. Primary colonizers such as *S. gordonii* bind to *S. mutans* via several proteins, by attaching to receptors on the *S. mutans* cell wall and helping to facilitate initial binding to the biofilm.

S. mutans, which is a cariogenic (capable of forming dental caries) bacterium, utilizes the energy in sucrose to produce an extremely sticky and adhesive extracellular substance called dextran polysaccharide via the enzyme *dextransucrase*, which belongs to the family of glucosyltransferases (Gtfs). Gtfs, which are also found in other oral streptococci, lactobacilli, and lactococci, contain a signal peptide that is common to all Gram positive bacteria as the N-terminus. Just downstream of the signal peptide there is a variable domain of unknown function, and downstream of this variable domain is the catalytic core. This is core contains an active site with 3 Asp residues about 500 amino acids from the N-terminus [51]. The C-terminal is responsible for keeping the enzyme attached to the growing glucan polymer. In addition to the Gtfs, four non-Gtf glucan-binding proteins are also made by *S. mutans*, and they assist the process in different ways: GbpA and GbpD that both contain a region which is homologous to the dextran-binding domains of the Gtfs, GbpC provides the property of dextran-dependent aggregation when the conditions become stressful, and GbpB which has a primary role in cell-wall metabolism but also possesses dextran-binding properties.

Dextran provides *S. mutans* with the ability to cohere to each other, and to adhere and stick to the biofilm on the tooth. Conversely, *S. mutans* utilizes other sugars such as fructose, glucose and lactose to produce lactic acid. This dual process of producing biofilm and acid through two different routes is what makes this organism a very

unique one. It is the combination of acid and plaque that leads to tooth decay and dental caries. Another trait that also separates *S. mutans* from the rest of the bacteria in the dental plaque is the ability to accumulate in large numbers in the presence of dietary sucrose. This ability requires both the cohesion among the dividing cells, and the adhesion to the tooth surface of to the colonies of the dental plaque [52] [53]. These adhesion and cohesion activities allow *S. mutans* to densely populate, which helps in activating mutacin genes (also known as bacteriocins) through quorum sensing two-component systems. *S. mutans* produces at least four of these mutacins (MutI, II, III, and IV). MutI, II, and III are lantibiotics that kill a wide range of Gram-positive bacteria, and MutIV is a non-lantibiotic that kills streptococcal species such as *S. Gordonii* [54]. This is another important tool that is utilized by *S. mutans* bacteria to kill off competing oral bacterial species when trying to colonize the tooth surface.

The acid that *S. mutans* produces is the main reason leading to dental caries. The ability of *S. mutans* to withstand low pH levels sets it apart from most other dental plaque species. This acid tolerance ability in *S. mutans* is mainly due to a robust acid tolerance response (ATR), which includes multiple genes that are up-regulated under low pH conditions. At pH levels where *S. mutans* stops growing, *S. mutans* continues to ferment carbohydrates and generate ATP which drives the F-ATPase proton pumps [55] [56]. Components of the general stress response, such as DNA Recombinase A, *S. mutans* Exonuclease, and DNa repair enzymes, are all up-regulated under conditions of low pH levels and thus they all contribute to the *S. mutans* acid tolerance ability [55].

The ability of *S. mutans* to ferment a wide array of carbohydrates, coupled with the aciduric properties, namely the acid tolerance response, favour *S. mutans* within dental plaque which leads to higher proportions of *S. mutans*, which in turn leads to increasing the demineralization rates of the dental enamel, and ultimately increasing the risk of developing dental caries.

S. mutans has been isolated from the blood of patients with the life-threatening disease *infective endocarditis* or IE [57] [58] [59], which is a microbial infection of the endothelium of the heart. In Japan, recent studies showed that streptococci are

behind 50 % of IE cases. These bacteria enter the bloodstream either through routine clinical dental procedures, or through daily oral hygiene practice, such as flossing and brushing [60].

3) Microbial co-adhesion

The next step in dental plaque formation is the co-adhesion of later colonizers to already attached pioneer bacteria. Late colonizers, such as *Aggregatibacter actinomycetemcomitans*, *Prevotella intermedia*, *Treponema spp*., *Eubacterium spp*., and *Porphyromonas gingivalis* [61], adhere, via their adhesins, to receptors of the already present early colonizers. As more late-colonizing species adhere to the plaque developing community, they facilitate the way for more species to integrate through co-aggregation interactions. The number of various microbial species increases via continuous integration and cell multiplications, contributing to an increase in biomass and production of exo-polymers to form more biofilm matrix [21]. Metal ions and other macromolecules and proteins can also be incorporated in the matrix to reinforce the structure and integrity of the biofilm.

3.2.2. Formation of dental plaque in hard-to-access sites

Interproximal (IP) space

The interpromixal (IP) space between teeth is defined as the space between two neighboring teeth (Figure 3.6). This IP space, or site, is considered, for purposes of oral hygiene, one of the most hard-to-access areas in the human dentition. The IP spaces offer the environment that facilitates the formation and development of dental biofilms. Food debris and bacteria accumulate more easily in such sites because of the tight geometry minimizing the cleansing effect of salivary flow, or tongue and oral muscles. Food impaction, or the forceful wedging of food into the IP spaces by the action of tongue, lips and cheeks, helps in developing dental plaque and providing it with enough nutrients for survival. Currently, the use of various flossing techniques on a daily basis to minimize or completely remove biofilms in the IP spaces is the best available method. In this thesis, the experiments will focus on the biofilms formed in

the IP spaces, and methods for detaching or disrupting them will be studied extensively.

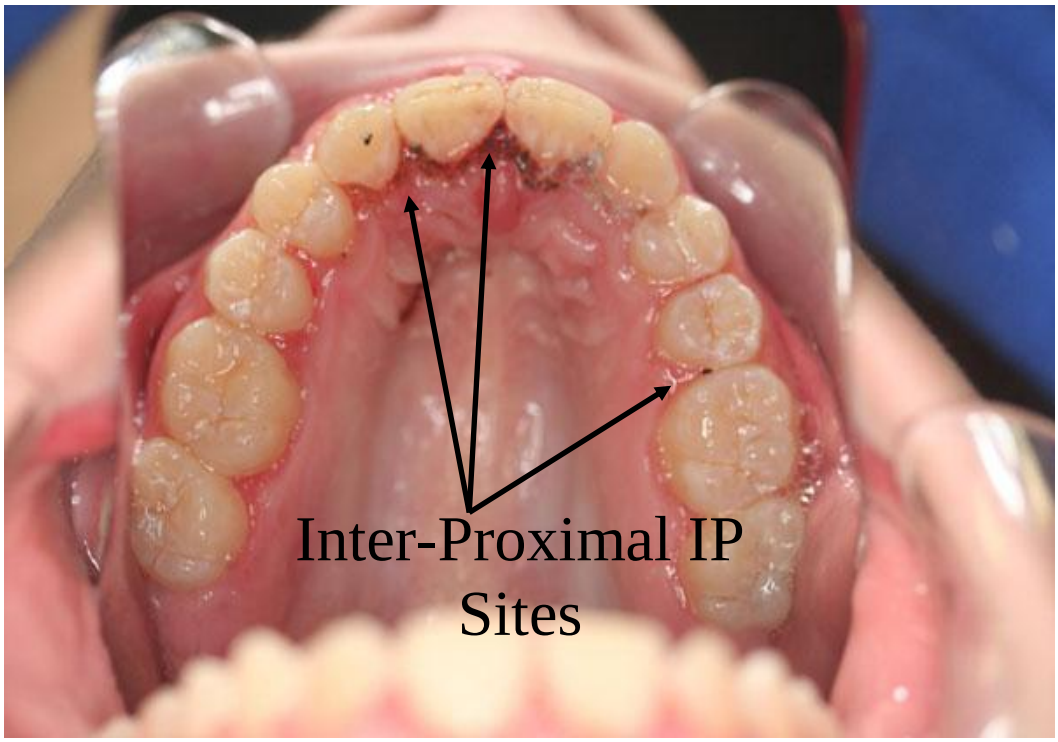

Figure 3.6 Intra-oral photograph taken for an upper jaw of a patient in a dental clinic. The three arrows point to the IP spaces between corresponding teeth, where dental plaque is clearly detected and seen between the teeth and the gingiva.

3.3. Biofilm detachment

As the biofilm forms, stability or balance is achieved among the component species in this biofilm, due to microbial interactions which play a major role in maintaining this balance [62]. Although the biofilm might be subjected to environmental changes, such as daily tooth brushing, food intake, or changes in salivary flow rate, the biofilm succeeds to maintain its microbial homeostasis, as long as these changes do not exceed the threshold that is compatible with this microbial community stability.

However, the interaction between a flowing liquid and attached biofilms may result in the complete or partial detachment of the biofilm. Under moderate flow conditions, the forces created by the fluid may be unable to dislodge the biofilm. In fact, biofilms have been shown to be able to deform their shape in reaction to the flow and may even grow in a streamlined profile in order to resist shearing forces [63]. When the shear forces overcome the restoring forces within the biofilm, portions of the biofilm break free and become loose, where they might either get washed out of the system or colonize a new site [63].

The detachment process is important because it has a clinical implication. For example, the detachment of dental biofilms could potentially transmit pathogens into the blood stream and cause bacteraemia and endocarditis [58]. Hence, the need to study the detachment process of these biofilms, both experimentally and computationally, to better understand how to effectively clean nascent biofilms keeping them in check.

3.4. Benefits of dental plaque biofilms for the microbial organisms

Microbial organisms gain many benefits when they all together work in synergy and constitute such complicated communities as dental biofilms. The existence of a large number (over 700) of different bacterial species in one place increase the tolerance to antimicrobial and inhibitory agents and increase the resistance to the host defence system (e.g. protective shield and diffusion limitation) [64]. Also, metabolism is improved and becomes more diverse and efficient. The metabolic waste products of one species could become nutrients for another species (syntrophism). Genetic exchange and lateral gene transfer is also one of the advantages that bacteria gain from forming a biofilm [62].

Causing a disease requires a wide range of virulence traits by an organism, and this becomes more feasible when different organisms interact together, or what is called “pathogenic synergism” [62] [65]. For example, in the human mouth, and in order for a gingival or periodontal disease to develop, bacterial cells should attach to teeth or gum, receive nutrients from the surrounding tissues and multiply, defeat or overcome

the host defence system, invade healthy cells and cause tissue damage. Working alone, many subgingival bacteria cannot do all these missions on their own and do not stand a chance against the human defence system. On the other hand, when different bacteria combine forces and form a more virulent association, then causing a disease becomes much easier [62] [66]. Because of all these benefits, it is clear now why bacteria have adapted to survival pressure to live in communities rather than as individual cells.

3.5. Mechanical properties of biofilms

Modelling biofilms and trying to control their formation and detachment necessitates the characterization of their mechanical properties. The EPS matrix determines to a large extent the mechanical properties of biofilms. The matrix is considered as a non-rigid substance, and is highly hydrated [21]. The EPS components are kept together by physicochemical interactions such as electrostatic interactions, van der Waals forces and hydrogen bonding in addition to biopolymers' entanglements which also contribute to the matrix mechanical stability [67]. Overcoming both cohesive and adhesive forces of the EPS is a major requirement in the detachment or removal process of dental biofilms. Shear forces influence the mechanical properties of biofilms and cause them to undergo phenotypic adaptation [68]. Polymer science predicts that the network arrangement of the EPS matrix as well as the EPS chemistry will determine the biofilm mechanical properties [20] [21]. Manipulation of biofilm mechanics will provide insight into future research aiming at looking into methods to disrupt and/or detach biofilms. Currently, the control of dental plaque biofilms is attempted through physical disruption in daily routine oral hygiene practices such as brushing, flossing, and rinsing with mouthwashes. Though these techniques are effective in disrupting plaque and killing bacteria (in case of mouthwashes and toothpastes that contain antimicrobial agents such as chlorhexidine gluconate), to a certain degree it has been shown that their penetration over physiologically relevant time periods is limited and bacteria at the basal layers of the plaque biofilm remain alive and active [22].

The interaction of inorganic ions with EPS can greatly alter the biofilms mechanical properties. The presence of multivalent ions, such as calcium, improved the mechanical stability of biofilms. For example, Korstgens and co-workers reported that the addition of calcium ions influenced the yield strength and modulus of elasticity of *P. aeruginosa* biofilms [67]. Also, it was reported that the cohesive strength of biofilms was influenced by the addition of calcium ions [69].

1) Viscoelasticity

The study of the plastic or elastic behaviour of biofilms has been seldom addressed in the literature. Viscoelasticity is the property that has been mostly reported in research conducted on biofilm mechanics. Preliminary studies using spinning disk rheometry have shown that from a mechanical point of view *S. mutans* biofilms, behave as viscoelastic polymers [70]. This viscoelastic behaviour of biofilms was also demonstrated in the rheological *in-situ* measurements of biofilm "streamers", where particles embedded in a biofilm were tracked and their response to changes over time in response to elevations in liquid shear stress was observed [71] [68]. Depending on the forces acting on their EPS matrix, biofilms show both reversible elasticity and irreversible deformation. When exposed to compressive forces, the biofilms undergo an elastic-solid-like behaviour phase until a break point is reached, then they start behaving like a viscous fluid [67] (Figure 3.7). Short-timescale stimuli results in elastic response, i.e. absorbing stress energy through deformation, from biofilms. On the other hand, long-timescale stimuli results in viscous response [72]. These phenomena describe the time dependent behaviour of the material which may be analysed in the frame of the theory of linear viscoelasticity [73]. This theory states that the relation between the stress resulting at any time ($t>0$) from an imposed history of strain is represented by Boltzmann's equation [74].

Characklis was the first to report on the biofilms viscoelastic properties [75] using cone-and-plate rheometer capable of measuring both viscous and elastic responses. Viscous flow is measured by a tangential force that is caused by resistance to flow when the cone turns with respect to the plate, while elasticity is measured by a normal force perpendicular to the plane of rotation. Tensile and shear adhesion strength of biofilms were studied by Ohashi and Harada who reported that both strengths

decreased with the aging of the biofilm [76]. A combination of controlled fluid shear and digital time lapse microscopy was used by Stoodley to conduct creep and stress-strain experiments on biofilms [77]. The results proved the viscoelastic behaviour of biofilms that was reported by Characklis. Similar results about the biofilms viscoelasticity was also reported by Klapper et al [78].

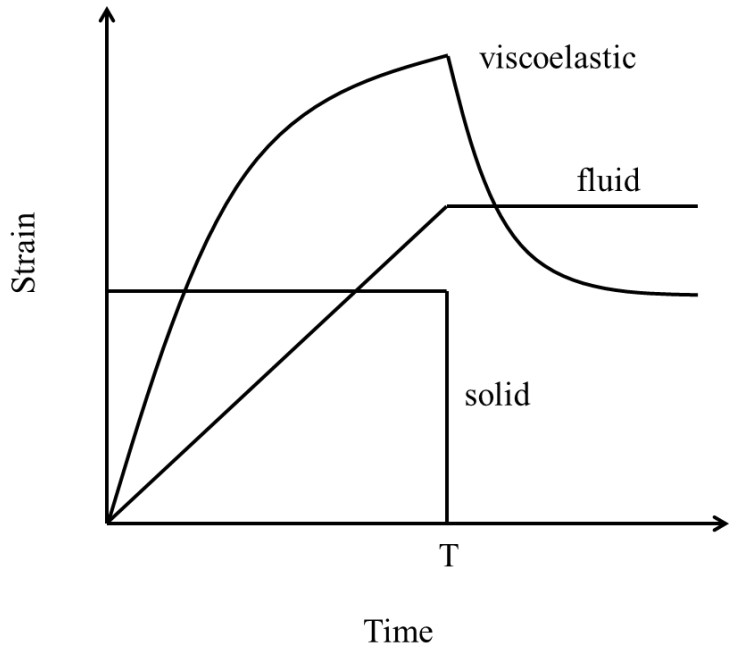

Figure 3.7 Schematic depicting the behaviour of a viscoelastic material subjected to stress. The three curves represent the response of three different types of materials to the same applied stress: ideal solid response (elastic), ideal liquid response (viscous), and viscoelastic response. The viscoelastic curve is a combination of both (adapted from Shaw et al. 1990 [79]).

2) Failure

Another important mechanical property that will be studied in this thesis is failure of biofilms. From a practical point of view, knowing how and when a biofilm might fail is considered significant in the study of biofilm mechanics because this will allow better prediction of accumulation and detachment which are key processes required in the understanding of the structure and function of biofilm systems. Two types of

failure most relevant to biofilms are cohesive and adhesive. Cohesive failure is defined as the failure that occurs within the biofilm and leads to removal of parts of the biofilm while other parts are still intact. This failure occurs when loading exceeds the ultimate strength of the biofilm. Cohesive failure in biofilms is usually site specific, probably due to the fact that biofilm has a heterogeneous structure leading to the loads being unevenly distributed over the biofilm. This "structural heterogeneity" of the biofilm refers to the fact that the EPS matrix is interspersed with water channels and pores, [80] and the density variations within the same biofilm [81]. Meanwhile, adhesive failure is defined as the failure that occurs at the interface between the biofilm and the substrate on which the biofilm grows. Adhesive failure usually leads to the detachment of larger parts of the biofilm, or even the whole biofilm. This kind of failure depends largely on the property of the interface between the biofilm and the substrate. For biofilm removal strategies, adhesive failure is more desirable, since cohesive failure only leads to removal of small parts of the biofilm, and thus can leave underlying biofilm to regrow rapidly.

3.6. Methods to measure mechanical properties of biofilms

Although measuring various mechanical properties of biofilms and interpreting the data is considered quite a challenging task due to the biological and structural heterogeneity of biofilms, their small size and because they are attached to surfaces, many methods have been attempted to achieve those goals. Data regarding some of these properties, e.g. cohesive strength, vary significantly depending on the method used for measuring. Though there is a consistency in the qualitative viscoelastic responses of biofilms to shear stresses [68], the quantitative data regarding their viscosity, stress relaxation, and elastic modulus vary greatly [82]. The main mechanical properties that are of interest would include modulus of elasticity or the stress/strain relation, ultimate strength (i.e. the stress leading to failure of the specimen), failure strain, and toughness. It is a challenging process to determine the mechanical properties of biofilms because they are typically thin, relatively soft and fragile, and desiccation is always a problem should they be removed from solution. Some examples for research conducted on biofilm mechanics include the work done by Chen *et al* who measured the strength of adhesion between biofilms and surfaces

using a micromanipulator [83], and Korstgens *et al* who used compression testing to study mechanical behaviour of biofilms [84].

The methods used to assess the material characteristics of biofilms are broadly classified into two categories. The first category include methods which use a directly applied and controlled loading force, in which the biofilm is affected directly by a mechanical force, usually without hydrodynamic flow, such as microcantilevers [85], indenters [86], or T-shaped probes [83]. The second category includes methods which use hydrodynamic loadings in which biofilms are subjected to a fluid flow such as in flow cells [77].

3.6.1. Methods using a direct applied force

Methods which test biofilms using a directly applied force are classified according to the type of effort that is sustained by the bacterial biofilm into three categories. The biofilm can be subjected to a tensile force, a compressive force or a shear force. The tensile testing techniques include centrifugation [76], tensile test device using biofilm-attached tubes, and microcantilever technique [87]. The compression testing methods include uniaxial compressive test [84] and microindentation [86], and they will be discussed in details in this chapter. The shear testing techniques include spinning disc rheometry [70] [88], and pulling testing shear [83].

Nanoindentation, atomic force microscopy, and uni-axial compression are three techniques that are used to study mechanical properties of biological samples. But our focus here will be on the uniaxial compression that was used in our study. The dental biofilms were subjected to uniaxial compression while in their physiological environment, and their mechanics and behaviour when applied to various agents and/or chemicals was investigated. The ability to use this technique at our school, and its unique advantages over many other techniques, allowed us to use in our study.

Uniaxial compressive test

Uniaxial compression tests can be used to measure mechanical properties of biofilms [89]. Such tests are usually conducted using indenters. Rheometers, which are capable

of measuring force as a function of gap thickness as biofilm is "squeezed" between two plates, are also used for compression tests [70] [84]. A stress-strain curve is obtained by uniaxial compression experiments. Mechanical parameters such as Young's modulus, shear modulus, or the yield strength are determined from that curve. The fact that the biofilm is a viscoelastic material means that during the timescale of the deformation some relaxation processes take place, and these are based on conformational changes of polymers segments. This means that the slower the indentation test the greater the contribution of viscous flow to the deformation. The main advantage of this technique is that it is relatively quickly and easily performed. The device is relatively simple, can be assembled in-house, and inexpensive. During measurement, the biofilm is kept in its physiological, hydrated state, which is another advantage of this method.

The apparatus for such test usually consists of a linear positioning stage connected to a moving upper plate, while a stationary bottom plate is fixed to a load cell (Figure 3.8), and interfaced to a computer for control, signal acquisition and data analysis. Biofilms are grown on glass slides which are in turn placed on the stationary bottom plate. During compression, the biofilms are deformed as a certain rate, and many parameters are recorded, such as the applied load and the resulting strain (σ). The stress (ε) exerted, or the force exerted per unit area of a biofilm, is calculated by normalizing the load applied over the cross-sectional area of the plunger area. Biofilms are compressed until the required strain is reached, at which point the compression is stopped because further deformation will only lead to the compaction of the biofilms. Multiple measurements will be done for each sample and the average of these measurements will be calculated and used for further analysis. Information about the *S. mutans* biofilms strength will be provided from the stress-strain curves obtained from their measurements. The modulus of elasticity (E) is calculated from Hooke's law as follows:

$$E = \varepsilon / \sigma \qquad (1)$$

Where (σ) is the resulting strain, and (ε) is the stress exerted, or the force exerted per unit area of a biofilm. Compressive strength is defined as the stress at the point of a

stress-strain curve where the linear relationship between stress and strain ends and the curve begins to bend, indicating the start of permanent deformation of the biofilm.

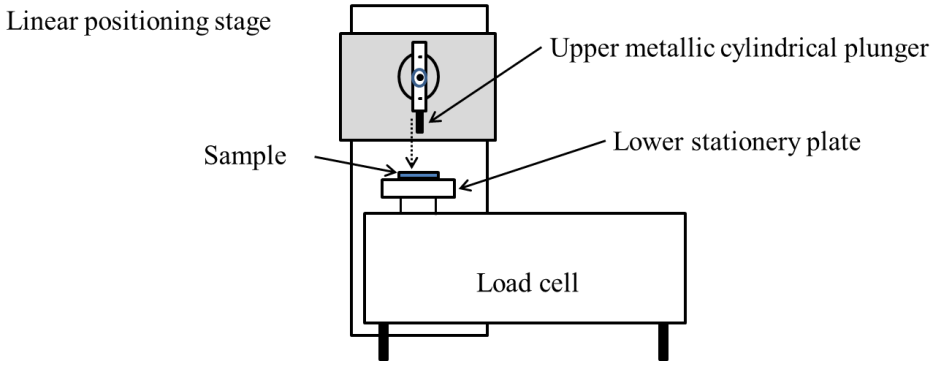

Figure 3.8 Schematic representing the frontal view of a uniaxial compression tester, showing the main components of the system. The dashed arrow indicates the direction of the force (Figure adapted from Paramonova et al 2007 [89]).

3.6.2. Methods using hydrodynamics

Multiple methods have been used to study mechanical properties of biofilms using hydrodynamic loading [68] [77] [90]. Two common approaches have been used to impose a hydrodynamic load. The first is to impose a movement to the biofilm, by rotating the biofilm for example (rotating disk biofilm reactor). The second one is achieved by controlling the speed of the flow and thus controlling the hydrodynamic flow.
This latter will be discussed in this chapter.

Imposed hydrodynamics flow (Flow-Cell)

One method for conducting simple stress-strain and creep tests on mixed and pure culture biofilms in situ is by observing the structural deformations caused by changes in hydrodynamic shear stress [77]. The principle of this flow cell method is simple: growing a biofilm under steady flow and then, by changing the flow, a hydrodynamic load is imposed. A microscope is used with this method to observe biofilm structural deformation and detachment. This resulted in heterogeneous biofilms that consisted of filamentous streamers that were readily deformed by changing the wall shear stress.

The advantages of this method are: simplicity, cheap to operate, and can be used on attached biofilms to perform simple stress-strain and creep tests by using the flow rate to vary the shear stress. Young's modulus has been estimated using this technique [78], viscoelastic effects have been reported [71] [77], and strength values have been approximated. Digital Images Correlation has been used to characterize the mechanics of biofilms in response to τ_w using digital video micrographs taken from biofilm flow cells.

3.7. Effect of surface roughness and hydrophobicity on the biofilm colonisation

The surface characteristics of the solid substrate are important in the biofilm colonization process. As the surface roughness increases, Characklis et al [91] showed that microbial colonization is higher due to the increase in surface area on rougher surfaces, and thus shear forces are diminished. Pons et al [92] concluded that surface roughness does not affect biofilm coverage by simply augmenting the geometric surface area available for adhesion, but in fact promotes bacterial settlement. In other studies, surface roughness did not appear to significantly influence biofilm formation, [93] nor influence caries lesion formation [94]. The data of 24 papers dealing with surface roughness impact on plaque formation in vivo was reviewed by Teughels et al [95]. The conclusion provided was that rougher surfaces accumulate and retain more plaque, and teeth with rough surfaces are more frequently surrounded by an inflamed periodontium.

Ionic interactions, van der Waals forces, and in particular, hydrophobic interactions are the main forces behind the formation of the proteinaceous pellicle. The term "hydrophobic interaction" loosely refers to the propensity of hydrocarbons to minimize their contact with water by associating. The generally accepted model of hydrophobic hydration invokes a cage of water molecules around the nonpolar solute molecule. Hydrophobic interactions (also termed "bonding") are generated when multiple nonpolar solutes, or fragments of molecules, associate to minimize the structuring of water around them [96]. Multiple, relatively weak, hydrophobic interactions are crucial to the formation of the pellicle. Hydrophobicity influences biofilm development [97], and bacteria attach more rapidly to hydrophobic, nonpolar

surfaces such as Teflon and other plastics than to hydrophilic materials such as glass or metals [98] [99] [100]. Although much contradictory results are obtained in such studies because no standardized methods exist for determining surface hydrophobicity, it is widely agreed upon that hydrophobic interactions occur between the bacterial cell surface and the substratum which enable the cell to overcome the repulsive forces active within a certain distance from the substratum surface and irreversibly attach.

3.8. Enzymatic disruption of *Streptococcus mutans* biofilms

There has been a growing interest recently in studying the enzymatic degradation of biofilms. Enzymes are highly selective and they cause the disruption of the structural stability of the EPS matrix of biofilms. As mentioned before, polysaccharides and proteins are the dominant components in the EPS, and they play a major structural role. Enzymatic degradation studies have focused on these two components, and various enzymatic combinations targeting proteins and polysaccharides have been used aiming to detach biofilms. Few advantages of enzymes that caused new technologies to utilize them for biofilm removal studies include their biodegradability, low toxicity, selectivity and specificity. However their insufficient stability, activity under specific conditions, and high price represent major drawbacks that limit their use.

Enzymes that have the ability to degrade biofilm matrix, by targeting specific molecules in the matrix, have been shown to inhibit biofilm formation or detach already establish biofilms. A number of enzymes have been used to target specific molecules involved in the biofilm matrix. For example, the presence of DNaseI disrupts the biomass and further accumulation of *Streptococcus mutans* biofilms by targeting the extracellular DNA (or eDNA), which plays a role in adhesion and surface aggregation [16] [101]. In this thesis, the effect of different enzymatic combinations on early-stage *S. mutans* biofilm formation and development was evaluated by determining their effects on the biofilm matrix.

3.9. Computational fluid dynamics (CFD)

Computational fluid dynamics can be used to numerically simulate biofilms mechanics. The process of impinging water droplets on *Streptococcus mutans* biofilms was studied experimentally and numerically, and the shear stress and pressure on the surface were determined and compared [102]. Key mechanical parameters can be determined using CFD software in combination with experimental data or input. Such parameters include:

- Maximum wall shear stress ($\tau_{w\,(max)}$) which is the maximum value of the shear stress measured on the tooth surface.

- Critical detachment wall shear stress which is a key determinant of biofilm removal from the tooth surface. Higher shear stresses are thus expected to cause more detachment and removal of biofilms.

- Wall shear stress spatial distribution which is the distribution of the shear stress on the tooth wall (and not just the absolute value of the shear stress). It can provide relevant information on the capacity of the fluid jet to provide a spatially distributed biofilm removal (not only localized in certain sites of the tooth surface).

- Normal stresses on the tooth surface may also play a significant role in biofilm removal or altering its 3D spatial arrangement.

CFD has been used in other types of biofilm studies to predict detachment. Xavier et al modelled the enzymatic disruption of the EPS in biofilms [103]. Boel et al modelled fluid-structure interactions in biofilm systems in order to simulate biofilm detachment as a result of mechanical processes [104]. Zhu eh al simulated saliva flow in order to investigate the salivary dynamic characteristics of plaque retention and periodontal status around appliances during orthodontic treatment [105]. Combining CFD with experimental work for validation is a powerful tool for biofilm research with regards to understanding biofilm-fluid interactions.

Chapter 4

4. Microbial tribology and disruption of dental plaque bacterial biofilms

ABSTRACT

We investigate tooth wear in the context of cleaning away dental plaque biofilms from tooth surfaces using high velocity water droplets. A laboratory model system was designed using a dextran gel as a biofilm surrogate and a typodont model to reproduce the geometry of the mouth. Using uni-axial compression, the elastic modulus of *Streptococcus mutans* biofilms was 380 Pa (± 350; n = 30), and the relaxation time was 12 seconds (± 11; n = 10). The type of surface, concentration of sugar in nutrients, chelation and osmotic pressure all had significant effects on biofilm stiffness. However, there was no direct relationship between biofilm stiffness and surface hydrophobicity and roughness. The elastic modulus of the gel was 17 kPa (± 12; n = 3), and the relaxation time was 15 seconds (± 12; n = 3) which was in the reported viscoelastic range of real bacterial biofilms.

High velocity 115 μL water drops travelling with an exit velocity of 60 m/s were generated using a prototype interdental cleaning device (Sonicare *AirFloss*). High-speed imaging showed that the gel was removed within approximately 6 ms of impact by adhesive failure from the tooth surface and within approximately 26 ms of impact by cohesive failure.

4.1. INTRODUCTION

Biotribology is the interdisciplinary field of research that combines physics, chemistry, biology, materials science and engineering [106]. Traditionally biotribology has focused on the various mechanisms employed by creatures such as flies, snails and geckos, to attach, stick and move around on surfaces [107], or the interactions between biological surfaces and fluids within an organism such as exemplified by a human joint. Here we define microbial tribology as a branch of biotribology, which focuses on the adhesion, disruption, mechanics and removal of microorganisms on different surfaces and the impact that they may have on the tribological performance of these surfaces. Bacteria and other microorganisms are capable of forming attached sessile communities known as biofilms, embedded in a matrix, on virtually every surface exposed to a non-sterile aqueous environment [22] [108]. This biofilm mode of life reduces antimicrobial susceptibility and can increase tolerance of the residing bacteria up to 1,000-fold, substantially diminishing antimicrobial efficacy, making biofilms extremely difficult to control in dental, medical and industrial settings [109] [110]. Biofilm-associated diseases have been cited by the Centres of Disease Control and Prevention as two of the main seven major healthcare challenges faced by the medical community [111]. Biofouling by biofilms is important in many industrial settings. Biofilms grow inside pipelines transporting water, oil, chemicals or fire extinguishing agents [112] [113]. In marine settings, microscopic biofilms play a major role in reducing the hydrodynamic efficiency of ships and propellers by increasing hydrodynamic drag [114]. Every year, the processes of cleaning, disinfection and replacement of biofilm-contaminated material cost hundreds of billions of dollars worldwide [111].

Bacteria in biofilms produce a matrix of extracellular polymeric substances (EPS) made up of carbohydrates, proteins, nucleic acids, and lipids/phospholipids [62] [21]. The EPS proportion in biofilms is generally estimated to constitute 50-90 % of the total organic matter [16]. These microorganisms become embedded in this matrix which protects them and is responsible for their structure, cohesiveness, physico-chemical properties and mechanical stability [20]. The community lifestyle of this three-dimensional, gel-like, highly hydrated EPS enables the biofilms to accumulate

and contribute to the persistent infections that can develop on soft and hard tissues, including the teeth and gums of the oral cavity [115]. Dental plaque is a biofilm that causes dental caries, gingivitis and periodontitis [6]. One of the early colonizers of the tooth surface is *Streptococcus mutans (S. mutans),* which is the bacterium responsible for initiation of dental plaque bacterial biofilms (*DPBBs*). *S. mutans* is a Gram-positive, facultative anaerobic bacterium that causes tooth damage in the presence of fermentable sugars such as sucrose, glucose or fructose by producing acid in the fermentation process [11] [12]. *In vitro* biofilms grown from *S. mutans* are widely used to model early stage cariogenic human dental plaque [62] [116] [52]. This model has been widely used in research to study biofilm attachment, disruption and mechanics, with the aim of developing novel detachment strategies [13] [14] [15].

An understanding of the mechanical behaviour of *DPBBs* is critical in order to enable the implementation of new strategies for the disruption and removal of these biofilms. Yet experiments and methods for the characterization of mechanical properties of biofilms remain challenging due to the need to establish a relationship between constitutive assumptions and experimental conditions. Mechanical removal by tooth brushing, flossing or water flow, during which multiple forces are applied from different directions, remains the most efficient way to disrupt and detach *DPBBs* from tooth and gum surfaces. These externally applied forces are compressive and shear [117]. In this paper, we describe the development of a dental typodont research model for testing the efficacy of mechanical removal of DPBB from the front, back and interproximal tooth surfaces. A uni-axial compressive test [118] was utilized to characterize the mechanical behaviour of model and real biofilms. The test was also used to characterize the effects of surface and liquid chemistry on biofilm properties. The first step was to make and characterize the mechanical properties of a dextran gel, which was used as a dental plaque surrogate, thus avoiding the time required to grow real biofilms and the issues of variability in biological systems. Dextran, the glucan produced by *S. mutans,* and which represents the major component of *DPBBs*' matrix [119] [120], was used to prepare the gel. The mechanical properties of the surrogate were characterized and compared to equivalent properties of *S. mutans* biofilms. The influence of different factors on the elastic modulus and relaxation behaviour of *S. mutans* biofilms was studied to test whether these factors can be used to manipulate the mechanical properties of the biofilms or if they demonstrate anti-biofilm

properties. The effect of changing the sugar concentration in the growth media was assessed. The osmotic pressure effect of polyethylene glycol (PEG-8000) on the biofilms was investigated. The effect of a chelating agent, ethylene di-amine tetra acetic acid (EDTA), was also studied. In addition, we assessed the effects of contact angle and surface roughness of four different materials, namely hydroxyapatite, titanium, stainless steel and polyethylene, on the elastic modulus of *S. mutans* biofilms.

Normally, wear in dentistry is considered in the context of physical wear of the hard surfaces of the teeth and dental implants from either attrition, abrasion or chemical erosion from acidic foods or acid production from dental plaques [88, 89]. However, here we investigate wear in the context of cleaning away the dental plaque biofilm, a viscoelastic material [78], from hard interproximal tooth surfaces using high-speed velocity water droplets. The effect of impact pressure of these droplets generated using a prototype Sonicare *AirFloss* was investigated as another mechanical approach for controlling biofilm build-up. The influence that the hydrodynamic pressure has on the failure and detachment of the surrogate dental plaque in the interproximal space (IP) of the upper central incisors of a typodont model was studied experimentally. High-speed imaging techniques, followed by image analysis, were used to visualize and quantify the detachment process.

4.2. MATERIALS AND METHODS

4.2.1 Bacteria and growth media

Biofilms were grown from *Streptococcus mutans* UA159 (ATCC 700610). Stock cultures of *S. mutans* were stored at -80^{o} C in 10 % glycerol in physiological buffered saline (PBS). Biofilms were cultured using sucrose supplemented brain heart infusion (BHI+S) medium (Sigma-Aldrich, The United Kingdom) and incubated at 37^{o} C and 5 % CO_2. Sucrose, a nutrient used for the bacteria, was added in 2 % wt/vol in water.

4.2.2. Compression testing of *Streptococcus mutans* biofilms

Flat-punch indentation using a small-scale mechanical tester (ElectroForce3200, Bose, Eden Prairie, MN, USA) was used to characterize mechanical properties of the *S. mutans* biofilms (Figure 4.1 A). Biofilms were grown on the bottom of 9 cm diameter polystyrene Petri dishes (Fisher Scientific, UK) under static conditions. The Petri dishes were inoculated with autoclaved (BHI+S) media, before an overnight culture of *S. mutans* was transferred. The biofilms were allowed to grow for 48h under static conditions, with the media changed once after 24h. The biofilms were rinsed with PBS to remove loosely attached bacteria. The Petri dishes with the attached biofilms were glued (commercial superglue) to the lower stationery base of the Bose with a curing time of approximately 15 seconds. The upper metallic cylindrical plunger (d = 7.72 mm) approach rate was set to 0.005 mm/s or 0.05 mm/s and the resulting force was recorded by a 5 N capacity load cell (Honeywell Sensotec, Columbus, OH, USA) as the biofilm was compressed by the plunger. A Hertz contact model was used to fit the resulting force (F) – displacement (d) curve to calculate E. Typical Poisson's ratio values are 0.2 for concrete, ~ 0.3 for stainless steel and ~ 0.5 for rubbers or polymers. Biofilm materials are expected to behave similarly to polymers, thus the value of 0.5 was assumed [78]. All tests were repeated on 5 different locations of the same biofilm sample and the average force-displacement data points were used to calculate Young's modulus (E). The experiment was repeated 6 times (n = 30). The stress exerted, or the force exerted per unit area of a biofilm, was calculated by normalizing the load applied over the cross-sectional area of the plunger. Biofilms were compressed up to a maximum deformation of 10 % at which the compression was stopped because further deformation would only lead to the compaction of the biofilms. Stress relaxation tests were performed by measuring force reduction for 30 - 60 seconds after 10 % deformation was reached, and relaxation time was defined when this 10 % drop has occurred. The testing was conducted on the biofilms while they were submerged in either media or buffer.

Young's modulus (E) of the *S. mutans* biofilms was calculated by adopting Hertz theory for contact mechanics for a cylindrical plunger compressing a thin film [121]:

$$F = \frac{2rEd}{\left(1-\nu^2\right)} \quad (1)$$

$$\text{then } E = \frac{slope \cdot \left(1-\nu^2\right)}{2r} \quad (2)$$

Where F is the loading force, r is the radius of the cylindrical plunger (r = 3.86 mm), ν is the Poisson's ratio, d is the displacement, and the slope (F/d) is obtained from the linear interpolation of the resulting force-versus-displacement data points.

4.2.3. Effect of nutrients, chelation, and osmotic pressure on the mechanics of *Streptococcus mutans* biofilms

Flat-punch indentation with the mechanical testing apparatus was further used to study the individual effects of chelation, changing the sugar concentration in the growth media, as well as exposing the biofilms to an osmotic pressure stressing agent, on the stiffness of the *S. mutans* biofilms.

Biofilm growth and the effect of different sucrose concentrations in media

The biofilms were grown on the bottom of petri plates as previously described. In this test, the sucrose was added in concentrations of 1 %, 2 %, 4 % and 8 % wt/vol of de-ionized and sterilized water. After the growth period of 48 h at static conditions, the *S. mutans* biofilms were rinsed twice with PBS to remove loosely attached bacteria, before starting the compressive testing as previously described in section 4.2.2.

Chelate effect

To assess the effect of cross-linking on the mechanical stability of biofilms we used a chelating agent, ethylene di-amine tetra acetic acid (EDTA), which is known for its ability to sequester metal ions. In this experiment, the biofilms were grown on the bottom of petri plates as previously described. After the growth period of 48 h under static conditions, the *S. mutans* biofilms were rinsed with PBS then exposed either to

0, 0.1, 1, 10, or 100 mM solutions EDTA (Sigma Aldrich, UK) for 20 minutes each, before running the uni-axial compression test.

Osmotic pressure effect

To test the effect of osmotic pressure on drawing water molecules out of the nano-channels and nano-pores inside the biofilm matrix, which may influence the mechanical stability of biofilms, and after the growth period of 48 h under static conditions, the biofilms were rinsed with PBS then exposed to different high-molecular-weight polyethylene glycol (PEG-8000) (Sigma Aldrich, UK) concentrations of 0, 10, 15, 20, 25 and 30 % wt/vol in water, for ten minutes at each concentration.

4.2.4. Effect of contact angle and roughness of different material surfaces on biofilm mechanics

Growth and mechanical properties of Streptococcus mutans biofilms

The biofilms were grown under the same conditions as previously described, but this time on flat circular coupons (1.1 cm diameter, and 0.2 - 0.4 cm thick) (Biosurface Technologies Corporation, Montana, USA) made from four different materials: commercially pure, grade 2 titanium (Ti) (98.9 % titanium content), hydroxyapatite (HA) (95 % purity), stainless steel (316L SS) and ultrahigh molecular weight polyethylene (UHMWPE), to test the effect of changing the surface material on the elastic modulus of the biofilms. The coupons were placed in the petri plates, with replicate coupons of each material in a different plate.

Contact angle measurements

Static contact angles on coupons made from the four materials were measured at room temperature and ambient humidity using the sessile drop method with a Drop Shape Analysis System (DSA 100) (Kruss, Germany). A 1 μL sessile drop of deionized water was placed on the coupons from a needle on a microsyringe at a rate of 100 μL/min. After the drop was set onto the coupon, a picture was captured. The circle-

fitting method was used to calculate the contact angle, where the drop contour was fitted to a segment of the circle. Measurement was repeated three times at each test site for reproducibility evaluation.

Average surface roughness (R_a)

In order to assess the effect of surface roughness on the mechanics of the biofilms, measurements of the average surface roughness (R_a) for the four surfaces were achieved by using Infinite Focus microscopy (Alicona, UK). High-resolution three dimensional images were captured at a 100 × magnification resulting in a field of view of 145 × 110 μm, with a sampling area of 90 × 90 nm^2 (1624 × 1232 points), and a deactivated polarizer. The measurements were done twice for each surface: dry and conditioned with media containing 2 % sucrose for 15 minutes. Alicona 3.1 software was used for image acquisition and measurement of average surface roughness. Four images were acquired for every surface. Four measurements of average surface roughness were taken at random locations. R_a values presented in this paper were the average of all the measurements performed.

4.2.5. Dextran gel as surrogate biofilm

To prepare the surrogate plaque, 1 g of dextran (Sigma-Aldrich, UK) was dissolved in 4 mL of de-ionized water (Millipore, UK) at room temperature. 0.25 g of calcium chloride ($CaCl_2$) (Sigma-Aldrich, UK) was added to the solution as a cross-linking agent. Agar (Fluka, UK) was then incrementally added to achieve a final concentration of 0.3 % wt/vol solution of agar in water, which had a viscosity of 3.1×10^5 $Pa\cdot s^{-1}$ [122]. The solution was stirred and heated on a hot plate at 80^o C until all particles were dissolved, then left for 2 hours to cool down at room temperature. Dry weight measurements were conducted on the resulting dextran gel by weighing a portion of the gel before and after heating on a plate for 120 seconds; this allowed complete removal of water. The dry mass of the dextran gel was 30 % (± 15; n = 10) of the total mass.

4.2.6. Compressive testing of the dextran gel

Compression testing using the mechanical testing apparatus was utilized to characterize the mechanical properties of the dextran gel (Figure 4.1 A). One drop of the gel was placed on a glass slide, which was glued to the stationery base of the Bose apparatus. The compression speed was set to 0.005 mm/s, and the resulting force (N) was recorded as the gel was compressed by using a 5 N capacity load cell. A Hertz model was used to fit the resulting force (F) – displacement (d) curve to calculate E, up to 25 % deformation (corresponding to d = 1 mm). The sample geometry has been approximated with a sphere with a diameter D = 4 mm estimated from digital camera images by calibration with a known reference dimension (Figure 4.1 B). Poisson's ratio of 0.5 for rubbers and polymers was used for the gel. The thickness of the gel was initially measured by a stereo microscope and the gel samples were compressed up to 10 % deformation. Three measurements were conducted on the gel by placing a fresh drop on the slide each time. In addition, stress relaxation tests were performed by monitoring force reduction for 30 - 60 seconds after 10 % deformation was reached.

E was calculated by adopting Hertz theory for contact mechanics between a cylindrical plunger and a spherical body [92]:

$$F = \frac{4/3 R^{1/2} E d^{3/2}}{(1 - \nu^2)} \quad (3)$$

$$\text{then } E = \frac{3/4 \times slope \times (1 - \nu^2)}{R^{1/2}} \quad (4)$$

While F, v, d are the same parameters defined previously, R is the radius of the gel droplet (~ 4 mm), the slope (F/d) was obtained from the linear interpolation of the resulting F versus $d^{3/2}$ data points.

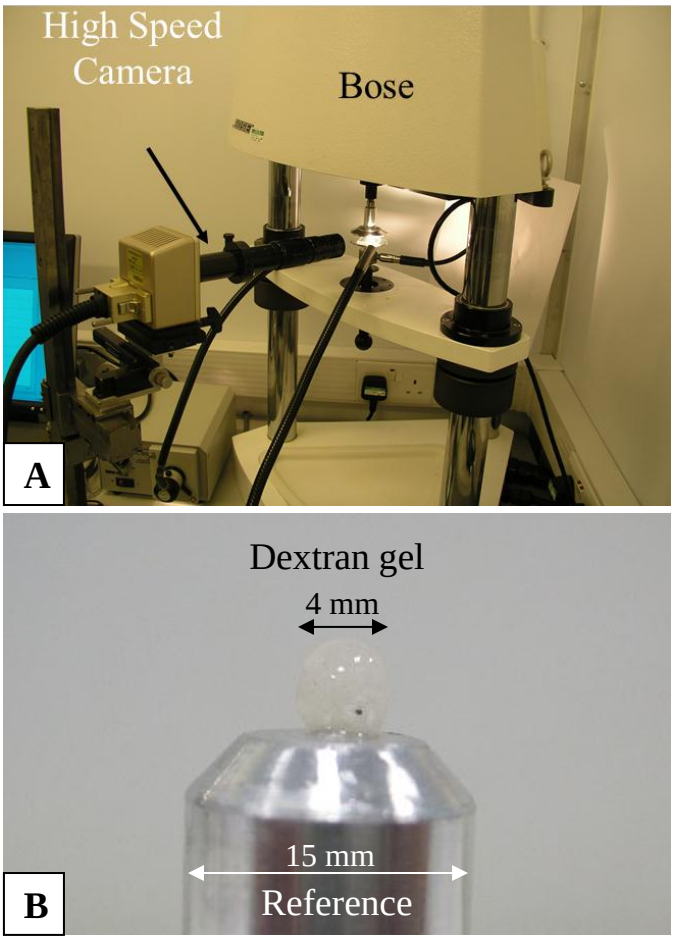

Figure 4.1 A) Photograph showing the experimental setup for the uni-axial compression test. **B)** The diameter of the spherical sample of the dextran gel was estimated by comparing it to the known dimensions of a reference plunger tip.

4.2.7. High-speed videography and microburst

High velocity water µ-drops with an average volume of 115 µL (± 50; n = 30) were generated using a prototype Sonicare *AirFloss* (provided by Philips Oral Healthcare (POH), Seattle), (Figure 4.2 A) which has a different nozzle shape, tip diameter, and different water volume per burst compared to the commercially available product, the Sonicare HX8111 *AirFloss* (POH, Seattle). The PT-*AirFloss* was designed to remove interproximal plaque (IP) by rapid bursting of pressurised water droplets and air through the interproximal spaces between teeth. The PT-*AirFloss* was modified in-

house so that it could be triggered remotely to avoid disturbing its position by pressing the activation button (as for normal operating conditions). A high-speed CCD camera (Ultima 512, Photron Inc., San Diego, CA, USA), equipped with a KC lens, with a KC-AUX and 1X, 3X or 4X magnifying lenses mounted on top of it (IF-1, IF-3 and IF-4, Infinity, Boulder, CO, USA) depending on the required magnification [118], was used to capture the bursting process of the PT-*AirFloss* (Figure 4.2 B). The high-speed camera can record up to 32,000 frames/s. A high-speed camera was required since the μ-burst was too fast to be seen with the naked eye, as it takes approximately 1/30 second for the complete process to occur. Videos were recorded with inter frame time intervals (or frames per seconds, fps) of 6.25×10^{-5} s (16,000 fps) and 1.25×10^{-4} s (8,000 fps). The camera field of view was 512 × 64 pixels (at a 4 × magnification) over a physical area of 200 × 20 mm^2. We captured a burst shooting in air to measure the initial exit velocity and calculate the impact pressure later on. The average exit velocity was found from images taken from duplicate experiments.

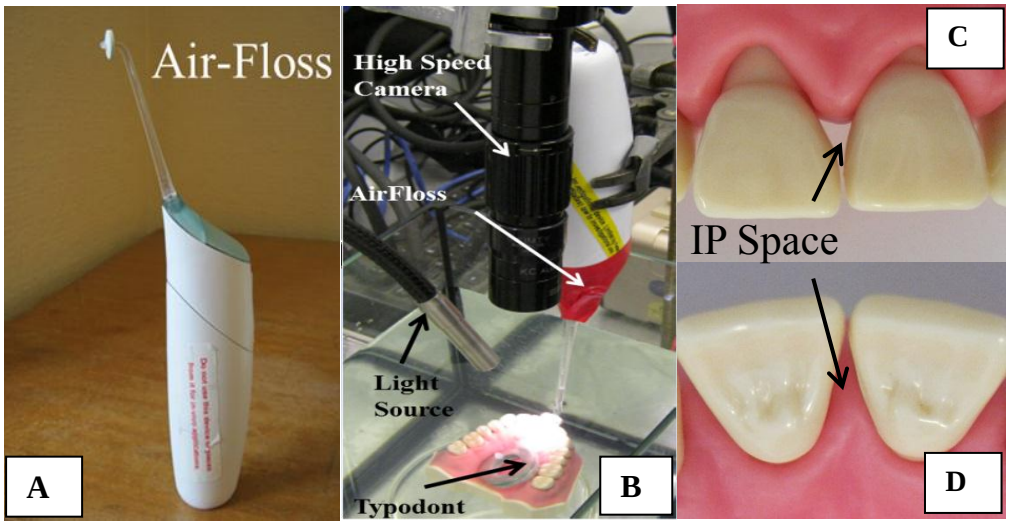

Figure 4.2 A) Philips PT-*AirFloss* that was used to generate the microburst. **B)** Experimental setup used for studying the high velocity water impact on the dextran gel in the IP space of a typodont. **C)** The IP space used in the experiments viewed from the front and **D)** from the bottom (or top).

4.2.8. Water impact on the surrogate in the IP space of a typodont

The PT-*AirFloss* was positioned in a clamp facing the IP space between the upper central incisors of a typodont in accordance with the manufacturers' recommendations (Figure 4.2 B). The typodont was illuminated from the front using optical fibre light sources (MH-100, Dolan Jenner Industries Inc., Lawrence, USA). The dextran gel was applied in the IP space between the upper central incisors of the typodont (Figures 4.2 C and D) and was kept hydrated by pipetting few drops of water every few minutes while setting up the high-speed camera to capture the bursts. The specifications for the high-speed camera used for this set of videos were mentioned in the previous section. Image analysis of the resulting videos allowed the estimation of the strain that the dextran gel undergoes before it finally breaks.

The impact pressure (P_w) exerted by the burst fluid on the dextran gel was calculated using [123]:

$$P_w = \frac{25\rho V_o^2}{\left(\frac{y}{D}\right)^2} \qquad (5)$$

where ρ is the density of water at 20^o C (998 kg/m^3), V_o is the initial velocity (or nozzle exit velocity in this case), y is the distance from the nozzle tip to the impacted surface (i.e. gel) which was measured to be 3 mm, and D is the diameter of the tip which was measured by microscopic images (D = 1.011 mm).

4.2.9. Statistical analyses

Data were reported as the arithmetic mean and one standard deviation from the mean. Statistical comparisons were made by comparing means using One-Way analysis of variance (ANOVA) by applying Levene's test of homogeneity of variance and the Tukey multiple-comparisons test, using Microsoft Office Excel (Microsoft Corporation, Redmond, CA). All tests were performed with a confidence level of 95%.

4.3. RESULTS

4.3.1. Mechanical characterization of the *Streptococcus mutans* biofilm

A typical load-versus-displacement curve for *S. mutans* biofilms is shown in Figure 4.3 A. *E* was calculated from the initial linear region of the curve up to (Figure 4.3 B) using Equations (1) and (2), and was 380 Pa (± 350; n = 30). The relaxation time was 12 seconds (± 11; n = 10), and typical force relaxation curves for *S. mutans* biofilms are shown in Figure 4.4. The wide variability obtained in the results for both *E* and relaxation time was expected, and attributed to the vast heterogeneity associated with biofilms. The mechanical characterization of the biofilms demonstrated their viscoelastic behaviour reported previously [78]. When compressed, the biofilms demonstrated both elastic and viscous behaviour.

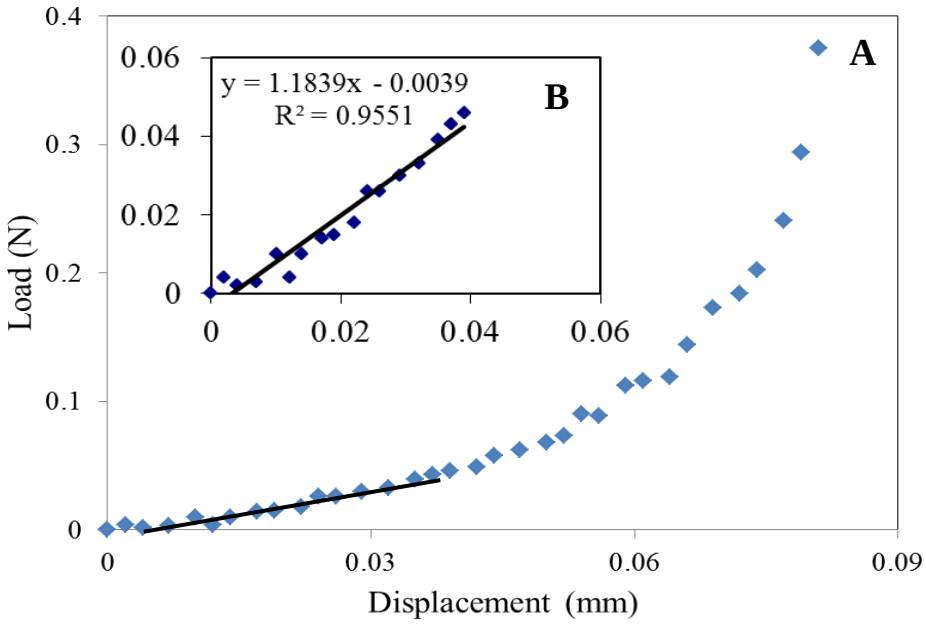

Figure 4.3 A) A representative load-versus-displacement plot for a *Streptococcus mutans* biofilm on a glass slide, showing the initial linear part followed by the curved region. **B**) The linear part of the plot (indicated by a best fit line) was used to estimate Young's modulus.

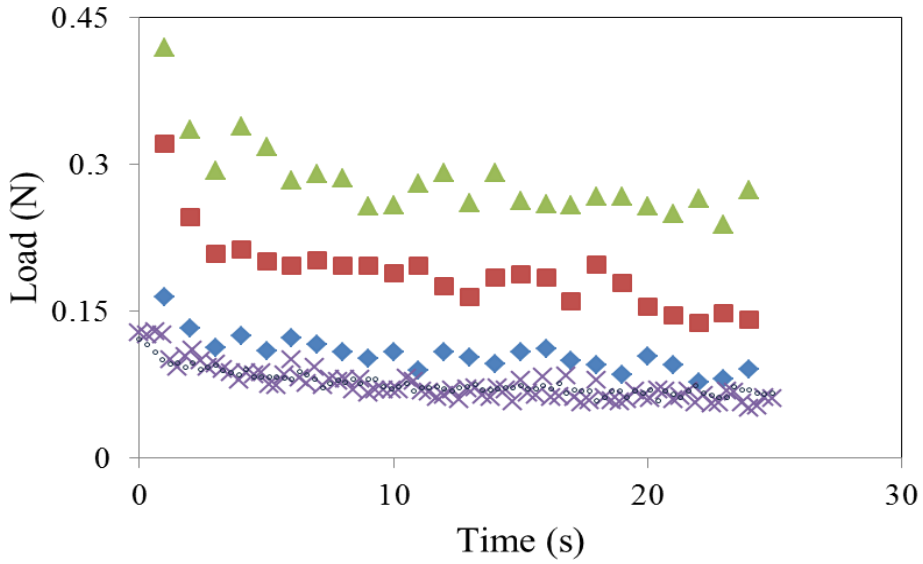

Figure 4.4 A representative force-relaxation curves for five different *S. mutans* biofilms.

4.3.2. Effect of sucrose on biofilm stiffness

Increasing the sucrose concentration in the media caused the biofilms to be stiffer with the average *E* increasing from 0.16 kPa (± 0.08, n = 15) at 1 % sucrose to 0.25 kPa (± 0.1, n = 15) at 8 % sucrose (Figure 4.5 A). A plateau was obtained between 4 % and 8 % sucrose. Statistically, the differences between the five data points on the graph were significant, except when comparing between 1 % and 2 %, or between 4 % and 8 %.

4.3.3. Chelate effect

The addition of the chelating agent, EDTA, to the biofilms reduced the average *E* from 0.41 kPa (± 0.25, n = 15) at 0.1 mM EDTA to 0.1 kPa (± 0.05, n = 15) at 100 mM EDTA (Figure 4.5 B). The five EDTA concentrations used were: 0, 0.1, 1, 10, and 100 mM. A plateau was reached after 10 mM EDTA. Statistically, there was no significant change in *E* when the biofilms were treated with 0.1 mM EDTA, but decreased significantly at 1 and 10 mM EDTA.

4.3.4. Effect of osmotic pressure on biofilm stiffness

The addition of PEG-8000, an osmotic stressing agent, to the biofilms caused an increase in Young's modulus from 0.22 kPa (± 0.2, n = 15) at 0 % PEG to 0.39 kPa (± 0.11, n = 15) at 25 % PEG wt/vol, after which no significant change was noticed and a plateau was reached (Figure 4.5 C). The differences between the data points on the graph were significant from 0 to 20 %, but insignificant between 20, 25 and 30 %. Similar behaviour was observed for polyelectrolyte thin films made from synthetic polymers when exposed to different PEG-8000 solutions [96].

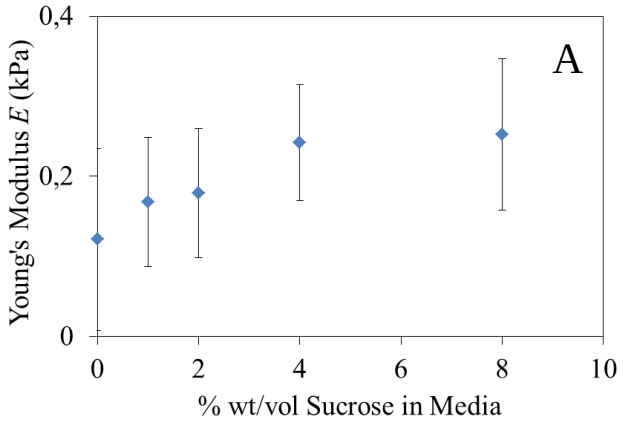

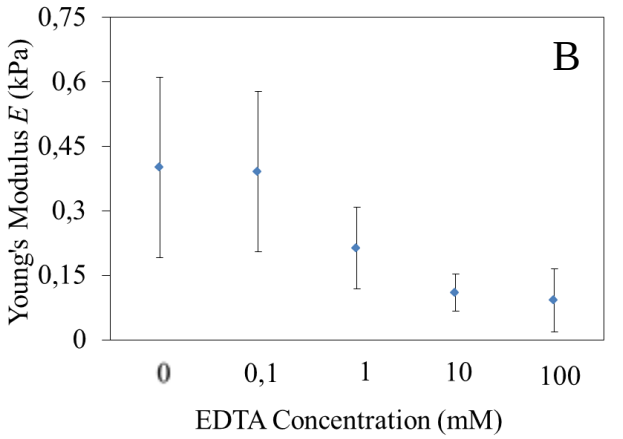

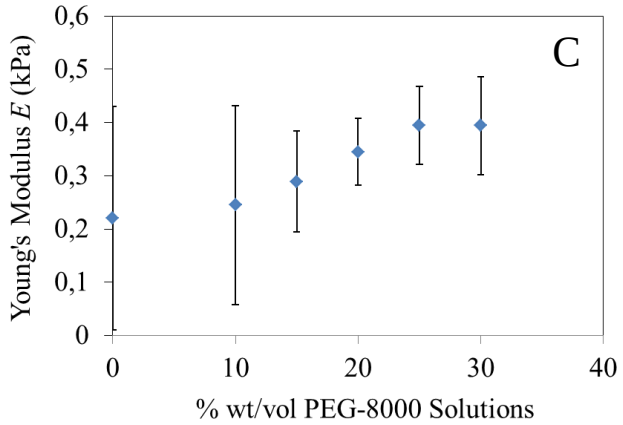

Figure 4.5 Effect of nutrients, chelation, and osmotic pressure on the mechanics of *S. mutans* biofilms. **A)** Sucrose concentrations versus *E* of *S. mutans* biofilms. **B)** EDTA concentrations versus *E* of *S. mutans* biofilms. **C)** PEG-8000 concentrations versus *E* of *S. mutans* biofilms. Each data point represents the mean from three independent experiments (n = 5 in each, so n = 15 in total). Error bars indicate the standard deviation of the measurements (n = 15). One-way analysis of variance (ANOVA) and Tukey's honestly significant difference (HSD) test with a confidence level of 95% were used.

4.3.5. Effect of contact angle and roughness of different surface materials on biofilm mechanics

The elastic moduli calculated for the biofilms on the four different surfaces (Ti, HA, PE, and SS) gave different results: biofilms on HA had the smallest *E* value of 0.045 kPa (± 0.019, n = 6), while the ones on UHMWPE gave the highest *E* value of 0.191 kPa (± 0.028, n = 6) (Figure 4.6).

Contact angle measurements showed that HA and Ti surfaces were both hydrophilic with contact angles at 43.9 ^{o} (± 10.2; n = 3) and 53.9 ^{o} (± 2.9; n = 3) respectively. Meanwhile, SS and PE had respective contact angles of 89.4 ^{o} (± 4; n = 3) and 97 ^{o} (± 4.9; n = 3), demonstrating their hydrophobicity. The relationship between the contact angle of the surface material and the elastic modulus of the biofilm on this surface is plotted in Figure 4.6. The two hydrophilic surfaces, HA and Ti, had biofilms with lower elastic moduli compared to those grown on the hydrophobic surfaces, SS and UHMWPE.

The measurements of (R_a) of the four different materials provided mean values of 7.5 nm (± 15) for SS, 25 nm (± 14) for Ti, 274 nm (± 35) for HA, and 337 nm (± 26) for PE. Each value is an average of four measurements on the dry coupons. After conditioning the surfaces, the new R_a values were 6.4 nm (± 6) for SS, 18 nm (± 8) for Ti, 166 nm (± 55) for HA, and 207 nm (± 38) for UHMWPE. These values indicate that R_a for the four surfaces decreased by 28 % for Ti, 35 % for SS, 39 % for HA, and 39 % for PE, after conditioning. However, no correlation was found between roughness and the elastic modulus of the biofilms grown on these surfaces.

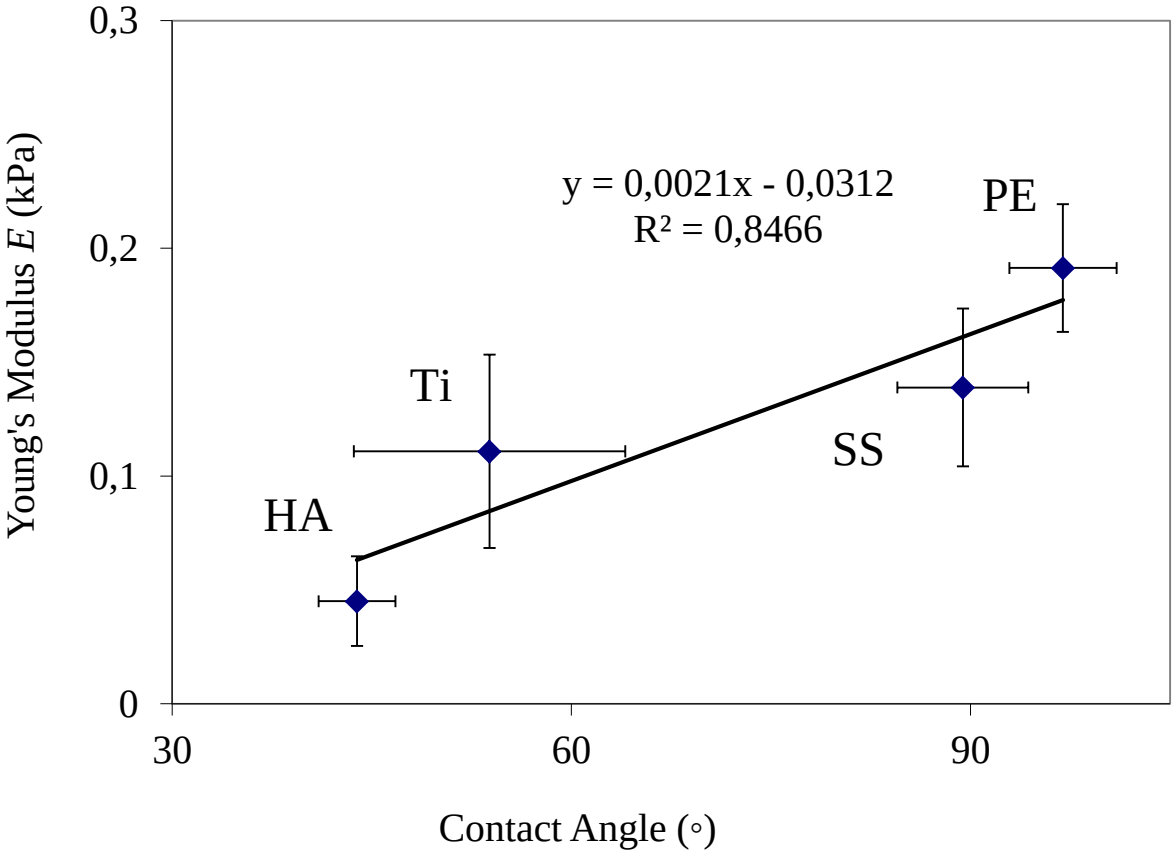

Figure 4.6 *E* of *S. mutans* biofilms as a function of hydrophobicity (measured by contact angle) of four different surface materials commonly used in dentistry or experimental models. Y-error bars indicate standard deviation (n = 5) and X-error bars indicate standard deviation (n = 3 for Ti and HA; n = 4 for SS and PE).

4.3.6. Dextran gel mechanical characterization

A typical behaviour of viscoelastic material was demonstrated in the load-versus-displacement curve for the dextran gel (Figure 4.7). The three plotted curves (Figure 4.7 A) showed similar trends: an initial linearity followed by an ascending curve, together forming the loading part of the test, and a descending unloading curve when the load was removed. *E* was 17 kPa (± 12; n = 3), calculated from the linear region of the curve using Equations (3) and (4). The loading and unloading parts of each curve

did not impose over each other, and the difference in-between being proportional to the energy dissipated as heat in the gel in one cycle of dynamic testing, or hysteresis.

Viscoelastic materials are characterized by a well-documented phenomenon which is stress relaxation. Three typical force relaxation curves for the dextran gel are shown in Figure 4.8. The asymptomatic decay was observed in the three curves. The drop from the maximum load to the plateau level was smallest in the third compression test (triangles), and largest in the first compression test (diamonds) of the gel. The larger the drop in load during force relaxation is, the smaller is the viscous component of the gel, and the smaller the drop the bigger its viscous component. This test was repeated three times, with three individual compressions on the same sample each time. The relaxation time for the dextran gel was 15 seconds (± 12; n = 3), which was calculated by considering the first value at which the curve started to plateau, followed by multiplying this value by 0.9. The beginning of the plateau phase was defined as the time at which the stress reached 10 % difference from the final value. In other words, stress relaxation time was defined as the time at when 90 % of the full relaxation was reached from the initial instant of loading [124].

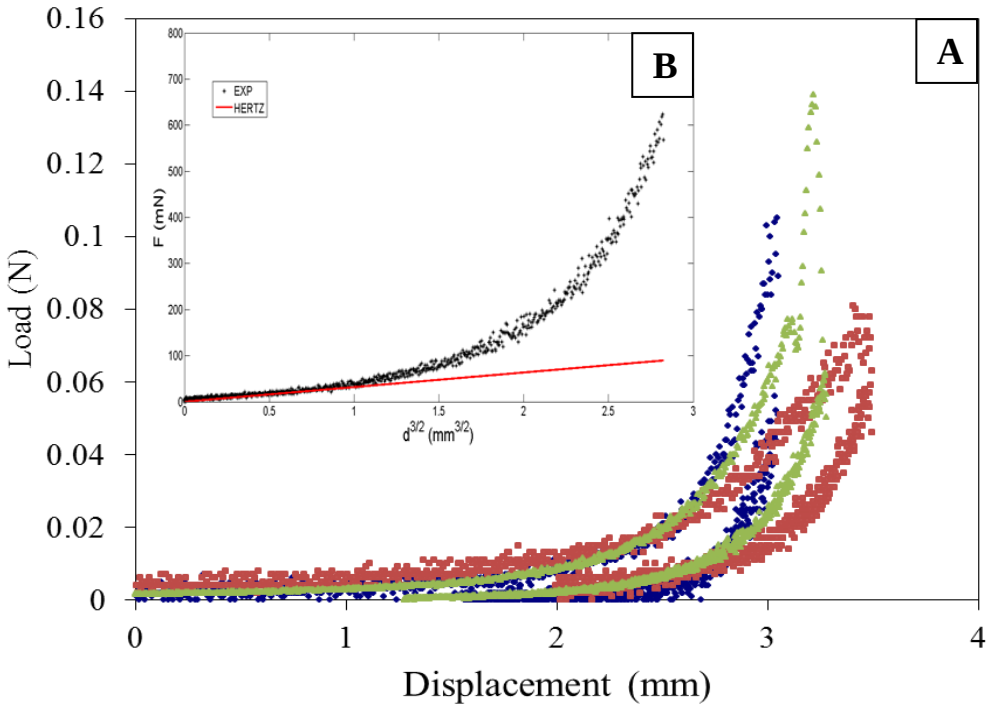

Figure 4.7 A) Three load-versus-displacement curves for the dextran gel. Panel **B)** A typical compression curve for dextran gel. Young's modulus was calculated by adopting Hertz theory for contact mechanics.

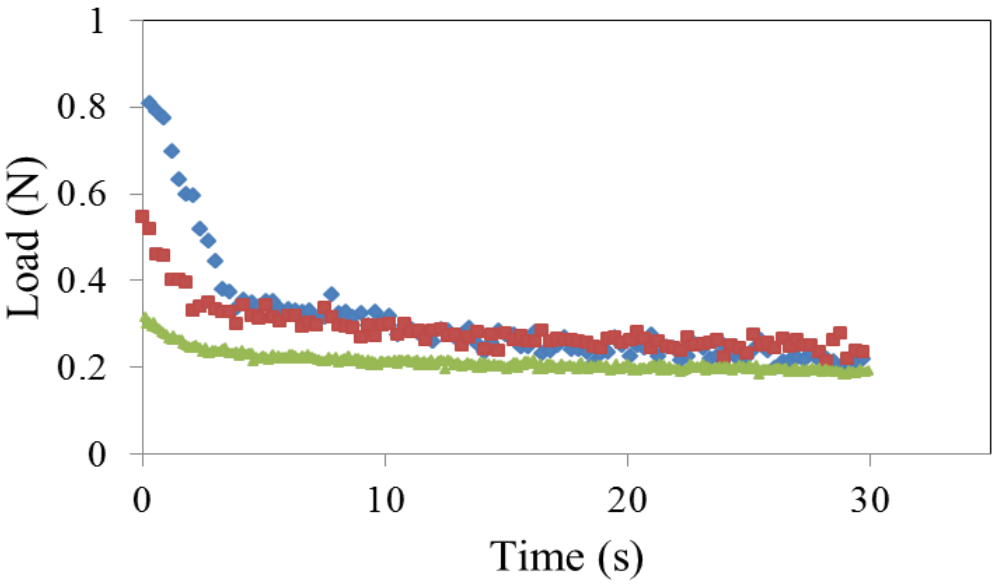

Figure 4.8 Three force-relaxation curves for the dextran gel representing repetitions of the test on the same sample.

4.3.7. Exit velocity and characterization of the microburst

Using high-speed imaging, the exit velocity of the fluid from the nozzle was calculated using the NIH software ImageJ (http://rsb.info.nih.gov/ij/), by measuring the distance travelled by the leading edge of the fluid burst between two consecutive frames in which the fluid was first seen exiting the nozzle (Figure 4.9). The water stream had an exit velocity (*Vo*) of 60 m/s (± 9; n = 8) from the tip which was estimated from eight independent movie sequences. The total duration of one burst was ~ 40 ms (supplementary video 1). We estimated from the images that ~ 90 % of the water was ejected in the first 10ms. Within this time interval, flow visualization of the burst showed an initial continuous stream of water which broke up into drops at approximately 8 mm from the tip exit according to Rayleigh breakup [125]. The steady stream from the tip was later on interrupted by air bubbles produced by the device.

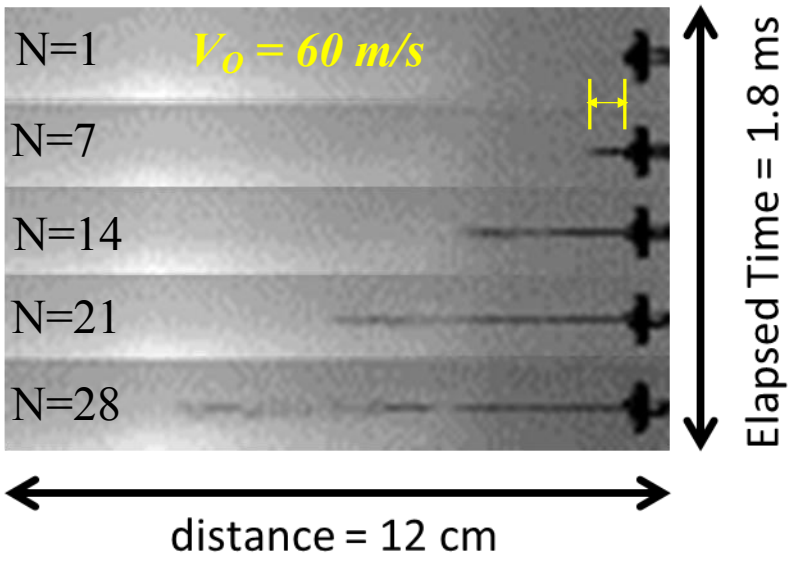

Figure 4.9 Stack of consecutive images obtained by high-speed videography, showing the water, burst (stained with black food dye) from the PT-*AirFloss*. These images were used to calculate the velocity of the fluid exiting the PT-*AirFloss*. The total elapsed time was 1.8 ms (total number of frames = 29), corresponding to a travelled distance of 12 cm.

4.3.8. Visualization of the dextran gel detachment caused by water impact

The detachment of the dextran gel caused by the burst mechanism of the water droplets from the PT-*AirFloss* was also recorded by the high-speed camera (Figure 4.10). In the first 10 ms, the impact of the water opened a hole through the middle of the gel and as the stream flowed through it dragged the gel with it stretching the gel which initially remained connected to the back of the corresponding teeth. The gel was elongated to more than 900 % (± 100; n = 3) of its original length at rest, before breaking. The impact pressure exerted on the gel was 10.22 MPa calculated using Equation (5) [123]. The video of the detachment is provided on a CD (supplementary video 3).

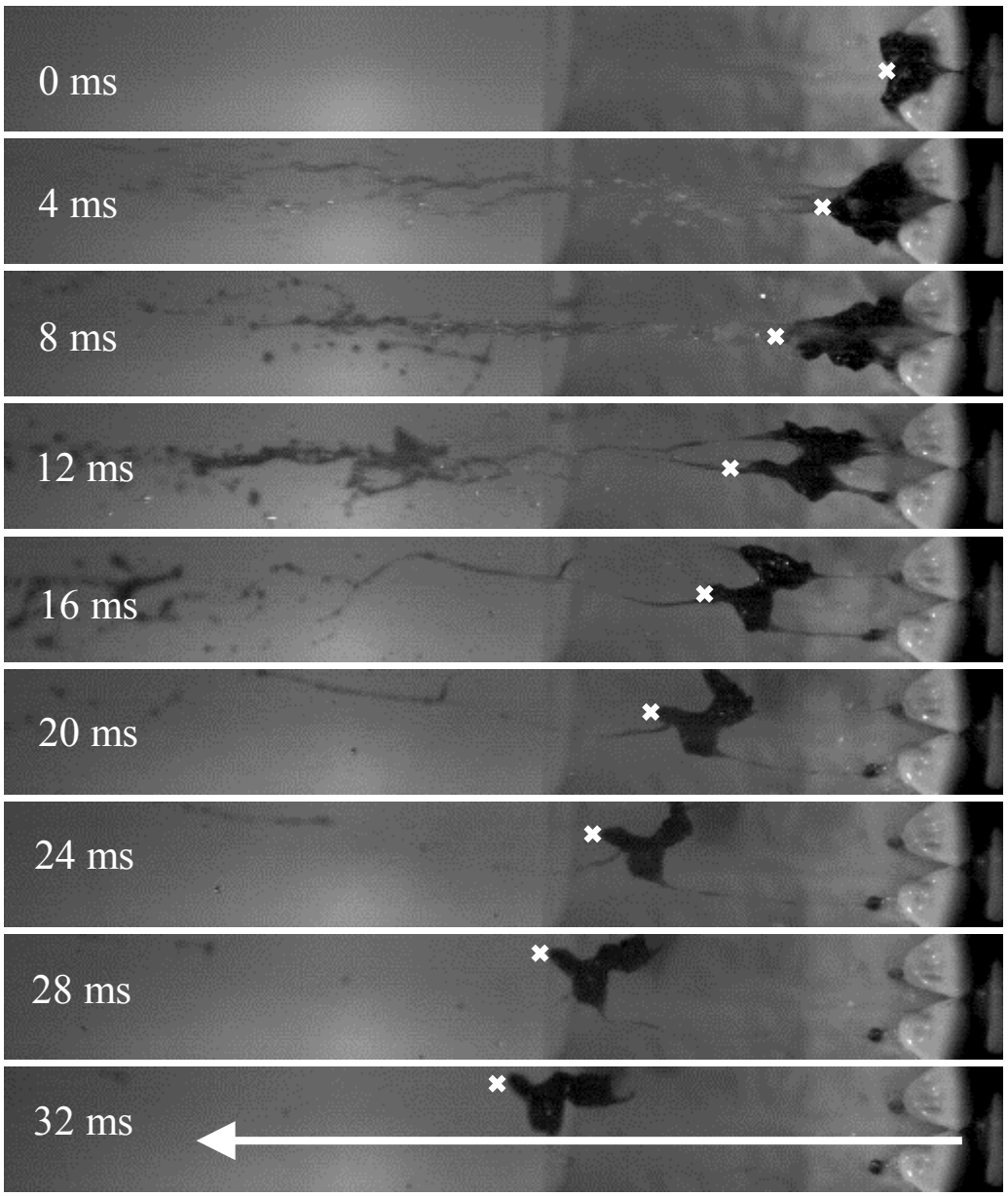

Figure 4.10 Stack of consecutive images obtained by high-speed videography, showing the PT-*AirFloss* burst (in the direction of the white arrow) impacting the IP space between the central incisors of the typodont, where the dextran gel was applied. These images were used to calculate the breaking strain of the surrogate. The white marks (x) represent the leading edge of the artificial plaque.

4.4. DISCUSSION

4.4.1. Viscoelasticity of bacterial biofilms

The force versus displacement curves obtained from the uni-axial testing (Figure 4.3) demonstrated the viscoelasticity of *S. mutans* biofilms. Applying Hertz theory for contact mechanics enabled the calculation of the elastic modulus of the biofilms. The values obtained are in agreement with values reported previously in literature [78]. The wide range of *E* values obtained confirmed the known heterogeneity that is associated with biofilms. The stress relaxation test further confirmed the viscoelasticity of the biofilms (Figure 4.4). Stress relaxation is a well-documented property of viscoelastic materials. The cross-links existing in biofilms matrix produce a viscoelastic network. When a constant displacement is applied to deform the biofilm, the free energy of the molecular segments will increase, and the chains respond by readjusting themselves (viscous-like flow) to relieve the ensuing force or load. The force will decrease each time a segment moves to a new, lower free energy state. The greater the cross-linking, the less the chains can diffuse and the extent of stress relaxation decreases dramatically [126]. The heterogeneity associated with bacterial biofilms, including the monospecies types, is evident when comparing stress relaxation curves in Figure 4.4. Even though the biofilms were grown under the same conditions and in the same environment, all the curves had a similar general trend, but none of them overlapped.

4.4.2. Effects of Sucrose, EDTA and PEG-8000 on biofilm mechanics

Changing the nutrient concentration in the growth medium affected the stiffness of the biofilms (Figure 4.5 A). Introducing more sucrose led to stiffer biofilms, which can be explained by the ability of the bacteria to utilize the sugar as a nutrient and produce more biomass with higher concentrations of glucan per biofilm matrix.

The effect of a chelating agent, EDTA, on the biofilm strength was also studied. Increasing the EDTA concentration produced biofilms with lower elastic modulus (Figure 4.5 B). EDTA binds to metals in the EPS of the biofilm, mainly calcium (Ca^{2+}) and iron (Fe^{3+}), forming soluble, complex molecules. This causes inactivation of the ions so that they cannot react normally with other elements or ions to produce

precipitates, which leads to breaking up the cross-links in the biofilm matrix. This significantly affects the cohesiveness of the biofilm.

The addition of PEG-8000, an osmotic stressing agent, caused the drawing out of water molecules and the stiffening of the biofilms. PEG-8000, a neutrally charged but highly water-soluble polymer, does not diffuse inside the biofilms from solution due to excluded volume restrictions, but rather creates an osmotic pressure capable of pulling water out of the biofilms. This makes the biofilms more compact and stiffer (Figure 4.5 C). PEG-8000 can be used to disrupt the water balance inside biofilms, and potentially disrupt the biofilms environment and equilibrium.

4.4.3. Effect of different surface materials on biofilm mechanics

Almost every surface in nature, in diverse environments, can be targeted by bacteria and colonized to produce a biofilm. Four materials were used to study the mechanics of biofilms on different surfaces: HA, Ti, SS and UHMWPE. HA is naturally found within teeth and bone in the human body, while Ti, SS and UHMWPE are commonly used as the material of choice for implants in the human body. Ti and SS in particular are widely used for dental implants and prosthetics, and orthodontic appliances. The effect of these four different materials on the mechanics of oral biofilms was studied. Mechanical testing demonstrated that biofilms on these different materials had different elastic moduli, proving the structural heterogeneity associated with biofilms. Under the same conditions and in the same environment, the monospecies *S. mutans* biofilms showed different mechanical properties on different surfaces. Ti and HA surfaces allowed the growth of biofilms with lower *E* than biofilms grown on SS and PE. Contact angle measurements showed that the surfaces of the Ti and HA coupons we used were hydrophilic, while those of SS and PE were hydrophobic. The contact angle results were in agreement with our mechanical testing data as demonstrated in the linear relationship in Figure 4.6. Biofilms on the hydrophilic surfaces were softer than the ones on hydrophobic surfaces. The roughness measurements showed that the two metallic coupons we used, Ti and SS, were smoother than either PE or HA. Although the results showed no relationship between material roughness and biofilm stiffness, they were in agreement with the Wenzel equation [127] which indicates that the water contact angle of the surface decreases with increasing surface roughness when the surface is hydrophilic. The rougher HA had a lower contact angle than the

smoother Ti, both being hydrophilic. Also, conditioning the surfaces with media made them smoother by an average of 35 % (± 7; n = 4) for the four materials used.

4.4.4. Effect of impact pressure on the detachment of the surrogate biofilm

Mechanical indentation tests enabled us to characterize the mechanical properties of *S. mutans* biofilms and their surrogate, the dextran gel. The dextran gel demonstrated viscoelastic behaviour and the validity of using it to replace real biofilms in bacteria-free research in different settings. In the loading/unloading graph of the dextran gel (Figure 4.7), hysteresis was evident, proving the viscoelasticity of the gel. Hysteresis is defined as the difference between the strain energy required to generate a given stress in a material and elastic energy at that stress. It is the energy dissipated as heat in a material in one cycle of dynamic testing [128]. Hysteresis can be determined by evaluating the area between the loading and unloading curves. Elastic recovery is defined by the ratio of the strain corresponding to first reaching zero stress during retraction to the fixed maximum strain. In Figure 4.8, the three force-relaxation curves demonstrated the viscoelasticity of the gel, whose mechanics resemble those previously reported for bacterial biofilms [78].

The high velocity water droplets released from the PT-*AirFloss* device were too fast to be seen by the naked eye. Their flow motion was captured using the high-speed videography techniques which enabled us to generate novel footage showing the entire µ-burst mechanism (supplementary video 1). By analysing the footage, we were able to calculate the exit velocity of the water µ-drops from the PT-*AirFloss* (Figure 4.9). Videos of the detachment of the surrogate plaque under high velocity water drops were also recorded. The device bursts a mixture of air and water, and the recorded videos demonstrated the presence of two phases: a) an initial continuous behaviour of the water flow of the burst (duration: 10 ms) and b) the ejection of air bubbles causing the water droplets to split into nanodrops (duration: 35 ms). In the presence of the dextran gel in the IP space (supplementary video 3), the impact of the burst water droplets caused the substrate to be stretched before becoming completely detached from the tooth surface and carried away within the fluid stream (Figure 4.10). Exposed to an impact pressure of 10.22 MPa, the gel was elongated to more than 9 times its original length at rest, before breaking. The removal process of the dextran gel by bursting pressure-driven high velocity water droplets can be characterized by

two phases. First, the stream impacts the plaque causing its immediate detachment at the impact site while creating a hole. This is more commonly termed as cohesive failure. After that, the water droplets penetrate through the hole creating a shear stress within the surrogate, while dragging it along its stream, causing it to elongate before breaking away from the tooth surface. This phase is known as the adhesive failure. This behaviour is typical of a viscoelastic material, such as bacterial biofilms [78].

4.5. CONCLUSION

The mechanical properties of the viscoelastic *S. mutans* biofilms were studied using uni-axial compression. These properties could be manipulated by growing the biofilm at different sucrose concentrations, or by subjecting pre-grown biofilms to different solutions of chelating and osmotic pressure stressing agents. The mechanical properties of biofilms on four different surfaces, 316L stainless steel, titanium, hydroxyapatite and polyethylene were also compared. Surface hydrophobicity and roughness had minimal effect on the mechanical properties of the biofilm.

The mechanical properties of a surrogate gel, that could be used to replace real biofilms in bacteria-free research settings, were also characterized and they matched those of real biofilms. The homogeneity and reproducibility of the surrogate, and the ability to prepare large amounts of it in minimal time provided us with the option to use it in our study instead of the time-consuming growing of the heterogeneous bacterial biofilms.

The detachment of biofilms with high velocity water μ-drops delivered by an interdental cleaning device prototype was investigated in the laboratory using the surrogate plaque. An experimental setup was built and a methodology was developed to characterize and visualize the μ-burst. The impact pressure of the water drop was high enough to cause sequential cohesive and adhesive viscoelastic failure contributing to the detachment process.

Chapter 5

5. Hydrodynamics of high-velocity water microdrops in the interproximal dental sites: an experimental and computational study

ABSTRACT

The flow field and local hydrodynamics of high velocity water microdrops impacting the interproximal (IP) space of typodont teeth were studied experimentally and computationally. Water droplets of 115 μL were experimentally produced by prototype *AirFloss* (PT-*AirFloss*) bursting pressurized air and water microdrops at a velocity of 60 m/s into the IP space of the maxillary central incisors. Using high-speed imaging techniques, clear footage was generated that showed the details of the PT-*AirFloss* microburst, and demonstrated two removal mechanisms of a laboratory-made dental plaque biofilm surrogate. Microcomputed Tomography (μ-CT) imaging was used to obtain 3D images of the typodont and the IP spaces. The shear stress distribution generated by the drop impacting the tooth surface was calculated by Computational Fluid Dynamics (CFD) simulations. Results demonstrated that the shear stress generated by the PT-*AirFloss* and its spatial distribution on the teeth surface plays a key role in dictating the efficacy of biofilm removal in the IP space. In addition, it was shown that CFD models could be potentially used to optimize water drop or microburst design towards a more effective biofilm removal performance. Furthermore, the influence of fluid shear flow on the detachment of *Streptococcus mutans* biofilms inside microfluidic channels was studied experimentally, and a critical detachment shear stress ($CDSS_{agg}$) was estimated for the removal of large biofilm-aggregates. This ($CDSS_{agg}$) was used in the CFD model to predict the spatial distribution of biofilm-aggregates detachment from the IP surface caused by the microburst.

5.1. INTRODUCTION

Good oral hygiene practice maintains a healthy oral cavity, controls the progress of dental plaque biofilms (*DPBs*) and calculus, and prevents further complications such as gum diseases and tooth decay [116]. The challenge of dental care products is to efficiently and quickly remove *DPBs* from hard-to-access areas in the mouth such as the interproximal (IP) spaces between the teeth. Mechanical removal of IP *DPBs* by traditional dental flossing products, such as dental flosses, dental floss picks, inter-dental brushes, and dental tapes, have been accompanied with bleeding, stuck or shredded floss, and prolonged flossing time [129]. Fluid shear stress is an alternative mechanical approach for controlling biofilm build-up. Previous studies have demonstrated that if sufficiently high fluid shear stress can be generated, this alone can stimulate biofilm detachment [90] [130] [131]. Impinging water droplets [102] and entrained air bubbles [132] have also been shown to be able to remove bacteria and biofilms from surfaces utilizing the additional effect of generating a "surface-tension force" away from the surface by the passage of an air/water interface [133]. An advantage of using fluid forces to remove biofilms is that mechanical forces can be projected beyond the device itself by generating currents in the fluid surrounding the teeth by powered brushing [134] or through the generation of water jets by oral irrigation [135]. However, continuous water jets have a disadvantage of requiring large reservoirs and can be messy to use because of the large volumes of water involved. More recently the Sonicare™ *AirFloss* device has been introduced for removing IP *DPBs*. The *AirFloss* shoots a small volume (115 μL) of water and some entrained air at high velocity between the IP space between teeth in a discrete burst, thus creating high shear stress and high impact pressure over short periods of time minimizing water volume and cleaning times.

In the previous chapter we studied the influence of a high velocity water microdrop impact on the detachment of artificial plaque from the IP space between the upper centrals of a typodont model by applying a laboratory-developed surrogate plaque model made from dextran to the typodont to visualize the flow over the teeth geometry and to demonstrate how a real biofilm might detach [17]. In this chapter, an experimental and computational study of the hydrodynamics of a water drop burst from a PT-*AirFloss* is presented, and the flow of the high velocity water droplets is

characterized using various digital image analysis techniques. Using high speed digital videography [118], the microburst from the PT-*AirFloss* and the detachment process of the surrogate plaque, which included both adhesive and cohesive failure, were captured. X-ray microcomputed tomography (µ-CT) was used to image the typodont in 3D in order to produce an anatomically correct reconstruction of a representative IP space. Computational fluid dynamics (CFD) numerical techniques were employed to model and predict the spatial distribution of fluid shear stress over the tooth surface, and investigate how this distribution is affected by varying the PT-*AirFloss* nozzle shape and placement. Finally, experiments to study the influence of fluid shear flow on the detachment of *Streptococcus mutans* biofilms inside microfluidic channels were conducted, and a critical biofilm detachment shear stress ($CDSS_{agg}$) was estimated for the large biofilm-aggregates. This $CDSS_{agg}$ value was used in the CFD modelling to predict where these aggregates would detach from the IP surface given the shear stress distribution caused by the microburst.

5.2. MATERIALS AND METHODS

5.2.1. µ-CT Geometry reconstruction of the typodont model

X-ray microcomputed tomography (μ-CT) was used to image a training typodont (A-PZ periodontal dental model 4030025, Frasaco GmbH, Germany) in 3D and construct a model of the IP space to be used in subsequent computational fluid dynamics modelling. Images were obtained using an X-Tek Benchtop160Xi scanner (X-Tek Systems Ltd, Tring, Hertfordshire, UK), equipped with a Hamamatsu C7943 X-ray flat panel sensor (Hamamatsu Photonics, Welwyn Garden City, Hertfordshire, UK). The scans were performed using "shuttle" mode, in which the scanner table moves back and forth, at 80 kV and 100 µA, with no filter. The reconstructed volume was 1999 × 2000 × 1540 voxels with 0.0456 mm voxel edge size. The source-to-object distance was 261 mm, the source-to-detector distance was 1140 mm, and the detector size was 2000 × 2000 pixels with 0.2 mm pixel edge size. The exposure time was 2000 ms (4 × gain, no binning). After removing the metallic screws from the typodont, the hard thermosetting plastic teeth, with the elastic silicone rubber gums and the plastic holder base of the typodont were readily distinguishable due to differences in

X-ray attenuation by the different materials, so that the individual typodont components could be constructed using CT-PRO 2.0 (Metris X-Tek, UK) and visualized using VG Studio Max 2.0 (Volume Graphics, Heidelberg, Germany) to show various aspects of the assembled typodont and the individual teeth while maintaining their spatial relationship (Figure 5.1 A-B).

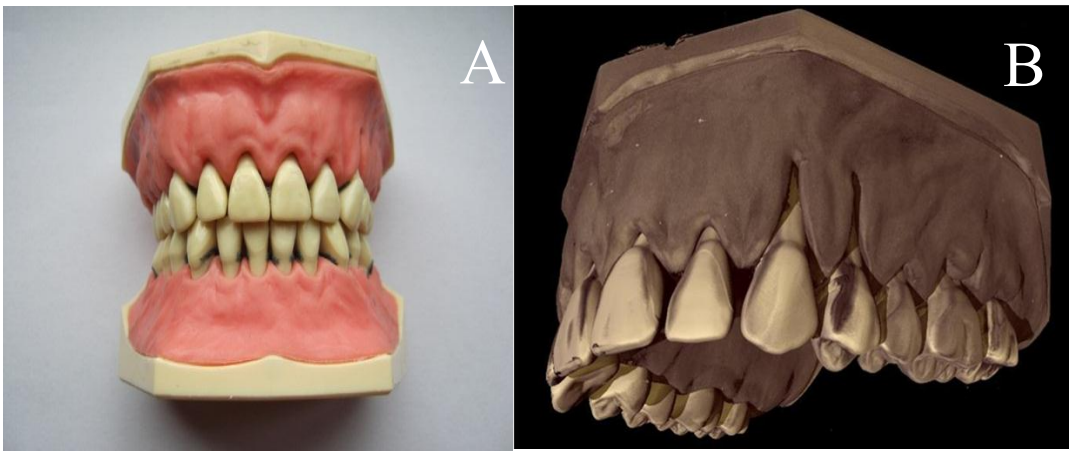

Figure 5.1 A) The Frasaco training typodont. B) Micro-CT image of the typodont of the upper jaw.

5.2.2. High-speed videography

High velocity water μ-drops with an average volume of 115 μL (± 50; n = 30) were generated using a Sonicare PT-*AirFloss* (provided by Philips Oral Healthcare (POH), Seattle), (Figure 5.2) which has a convergent nozzle diameter of 1.011 mm, measured by microscopic images. The PT-*AirFloss* was modified in-house so that it could be triggered remotely to avoid disturbing its position by pressing the activation button (as for normal operating conditions). A high-speed CCD camera (Ultima 512, Photron Inc., San Diego, CA, USA), equipped with a KC lens, with a KC-AUX and 1X, 3X or 4X magnifying lenses mounted on top of it (IF-1, IF-3 and IF-4, Infinity, Boulder, CO, USA) depending on the required magnification, was used to capture the bursting process of the PT-*AirFloss*. The high-speed camera can record up to 32,000 frames/s. A high-speed camera was required since the μ-burst takes approximately 1/30 second for the complete process to occur. The typodont was illuminated from the front using optical fibre light sources (MH-100, Dolan Jenner Industries Inc., Lawrence, MA, USA). Videos were recorded with inter frame time intervals (or frames per seconds, fps) of 6.25×10^{-5} s (16,000 fps) and 1.25×10^{-4} s (8,000 fps). The camera field of view

was 512 × 64 pixels (at a 4 × magnification) over a physical area of 200 × 20 mm^2. We first captured the microburst of the PT-*AirFloss* shooting in air to characterize the type of flow. Then we captured the µ-bursts when the tip was positioned in the IP space of a clean typodont. The exit velocity was calculated by measuring the distance travelled by the leading water drop edge between consecutive frames. The average exit velocity was found from images taken from duplicate experiments. Finally, dextran gel was prepared as described previously, and then applied in the IP space between the upper central incisors of the typodont and was kept hydrated by pipetting few drops of water every few minutes while setting up the camera. Videos showing the detachment mechanism of the dextran gel were captured, and the resulting images were analysed to extract quantitative description of the removal process.

Figure 5.2 Experimental set-up and the position of each of the PT-*AirFloss*, high speed camera and light source with respect to the typodont.

5.2.3. Microburst characterization

The density, ρ (998 $kg.m^{-3}$), viscosity η ($8.90x10^{-4}$ $Pa{\cdot}s^{-1}$) and surface tension γ (γ air/water = 0.072 $N.m^{-1}$) of water at 20^{o} C, the exit velocity (*Vo*) of the water stream from the tip, and the diameter (*D*) of the tip which was measured by microscopic images (*D* = 1.011 mm) were used to calculate the Reynolds number (*Re*) of the emerging water burst, the hydrodynamic Weber number (*We*), and the Ohnesorge number (*Oh*) [136], where:

$$\mathrm{Re} = \frac{Vo\rho D}{\eta} \quad (1)$$

$$We = \frac{Vo^2 \rho D}{\gamma} \quad (2)$$

and

$$Oh = \frac{\sqrt{We}}{\mathrm{Re}} \quad (3)$$

Re characterizes the relative importance of inertial and viscous forces in a flow, and is used to predict the flow regime. *We* is the measure of relative importance of fluid inertia compared to its surface tension (water/air surface tension in this case), and *Oh* is the ratio between viscous forces to the inertial and surface tension forces. Both *We* and *Oh* are used to predict the microburst break up [137].

The impact pressure exerted by the burst fluid on the dextran gel was calculated using:

$$P_w = \frac{25\rho V_o^2}{\left(\frac{y}{D}\right)^2} \quad (4)$$

Where, *Vo* is the initial velocity (or exit velocity in this case, u_{exit} = 60 m/s), *y* is the distance from the nozzle tip to the impacted surface which was estimated to be 3 mm, and *D* is the diameter of the tip which was measured by microscopic images (*D* = 1.011 mm).

5.2.4. Critical shear stress for *Streptococcus mutans* biofilm removal

1) Bacteria and growth media

Biofilms were grown from *Streptococcus mutans* UA159 (ATCC 700610). Stock cultures of *S. mutans* were stored at -80^{o} C in 10 % glycerol in physiological buffered

saline (PBS). Biofilms were cultured using sucrose (2 % w/v) supplemented brain heart infusion (BHI+S) medium (Sigma-Aldrich, The United Kingdom) and incubated at 37^{o} C and 5 % CO_2.

2) Streptococcus mutans biofilms inside microfluidic channels

To estimate a critical hydrodynamic shear stress required for *S. mutans* biofilm detachment, which could be used as a model input parameter for predicting the spatial distribution of biofilm removal, a BioFlux^{TM} 1000 device (Fluxion Biosciences, South San Francisco, CA, USA) was used. The BioFlux^{TM} 1000 uses pneumatic pressure to drive liquid through microfluidic channels (channel depth: 70 μm; channel width: 350 μm) so that biofilms can be grown and subjected to precisely controlled wall shear stresses. The bottom of the channels consists of a standard 180 μm coverslip glass, which allows microscopic observations to be made. The channels connect pairs of wells, one serving as a reservoir from which fresh medium was pumped through the channels and conveyed into the discharge wells, where the spent medium accumulated [138]. Six channels were each primed with 100 μL BHI+S growth medium until they were completely filled. Then 100 μL of bacterial solution of *S. mutans* in BHI+S, whose concentration was adjusted so that the optical density at 600 nm [OD_{600}] in medium was 0.1, was added to the discharge wells by pumping for 2 sec at 93 μL·h^{-1} to achieve a shear stress of 0.1 Pa. The chamber was positioned on the stage of an inverted microscope (AMG EVOS fl) equipped with digital image capture. Once even coverage of bacteria in the channel was obtained (4 x 10^{6} cells·cm^{-2}, as estimated from microscopic images), the flow was stopped and the bacteria were left to attach for 90 min in the incubator at 37^{o} C and 5% CO_2. After the attachment phase, excess solution in the effluent discharge wells was removed while the inlet wells were filled, and 40 μL of 1% virkon solution in water were added to sterilize the discharge wells to prevent back growth. After 10 minutes, 30 μL of the virkon solution were removed, leaving 10 μL in the outlet well. For the biofilm growth phase, 1 mL of fresh medium was added to the inlet wells and left for 18 hours in the incubator to grow at 9.3 μL·h^{-1} (corresponding to a wall shear stress of 0.01 Pa). This flow rate was selected based on the volume required for the desired biofilm growth period, and for the shear detachment assay given the 1.25 mL media volume capacity of the system. After 18 hours, biofilm clusters had formed in all the six channels, and one channel was chosen

for time-lapse microscopy. For the shear detachment assay the fluid shear stress at the microchannels walls was increased from 0.01 Pa to 2.0 Pa, with an increment step of 0.1 Pa, every 2 minutes. The shear induced detachment process was captured by taking 1 frame every 20 seconds; corresponding to a total number of 6 frames for each shear stress value. The experiment was repeated in triplicate, each time selecting the largest cluster in the frame to monitor the detachment process. The resulting three video sequences were analysed by ImageJ (http://rsb.info.nih.gov/ij/) to quantify the progress of detachment over time, and to estimate the critical detachment shear stress of biofilm-aggregates ($CDSS_{agg}$). Three $CDSS_{agg}$ values of 0.3, 1.0 and 1.7 Pa were obtained from the recorded videos, at which the selected aggregates were detached from the flat glass surface. However, the single bacterial cells and the smaller colonies rolled over the surface but did not detach, suggesting that higher values of shear stress were needed to cause complete detachment. The shear stress value of 1.7 Pa was used as the $CDSS_{agg}$ for the computational simulations, which was the highest value achieved under our experimental conditions. Previous determinations of the critical shear stress for the detachment of biofilms of other bacterial species are in a close range (5-12 Pa) [68] [139].

5.2.5. Computational fluid dynamics simulations

To model the dynamic behaviour of the microburst created within the IP space, the tomography obtained from μ-CT was converted to a 3D computer aided design (CAD) geometry (Figure 5.3) using Amira software (Mercury Computer Systems, Berlin, Germany, http://www.amira.com/). The computational domain, represented by the IP space, was discretized with software Gambit 2.4.6 (Simmetrix Inc., U.S.A.) using tetrahedral meshing scheme (Figure 5.4 A). A cell size of ~155 μm was chosen which led to a total number of 143985 mesh elements. Since the IP space was symmetrical, only half of the IP space was modelled, reducing computational cost.

CFD simulations based on the finite element method (FEM) were performed using ANSYS Fluent 12.1.4 software (ANSYS Inc., Canonsburg, PA, USA), which allowed for the determination of the flow field within the IP space and τ_w generated on the tooth surface. The air-liquid interaction resulting from the water burst moving within an air-filled space was simulated by adopting a Volume of Fluid (VOF) multi-phase

model, with surface tension (γ) between air and water set to 0.072 $N.m^{-1}$. VOF models are commonly used to perform simulations involving free surface flows with sharp interfaces. In this method, in addition to quantities such as pressure and velocity, a scalar quantity is introduced for each grid element, which represents the fraction of the two phases, air and water. If an element is filled entirely with water, the VOF fraction is equal to 1; if an element is filled completely with air, the VOF fraction is instead equal to 0. For elements that are partially filled with water, the VOF scalar takes a value between 0 and 1, in accordance with the water fraction. The VOF fraction was transported by means of the advection equation [140]. A steady-state model was used for solving the Navier-Stokes equations within the IP space. The robust and time-effective *k-ε* model was observed to provide the best convergence of the solution, and was selected for the present numerical study [141]. The experimentally-assessed value of 60 $m.s^{-1}$ for the exit velocity was used as a velocity boundary condition. Atmospheric pressure was set as a boundary condition at the outlet sections of the fluidic domain. The teeth and gum surfaces were modelled as rigid walls. The physical properties of water at 20^{o} C were used as previously described.

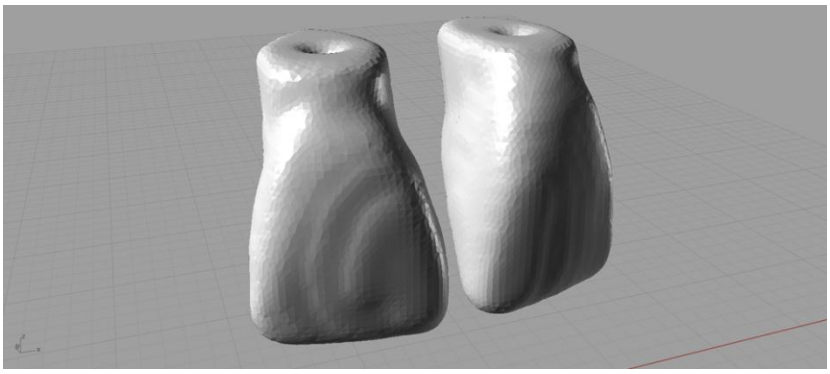

Figure 5.3 CAD-based 3D rendering of the IP space.

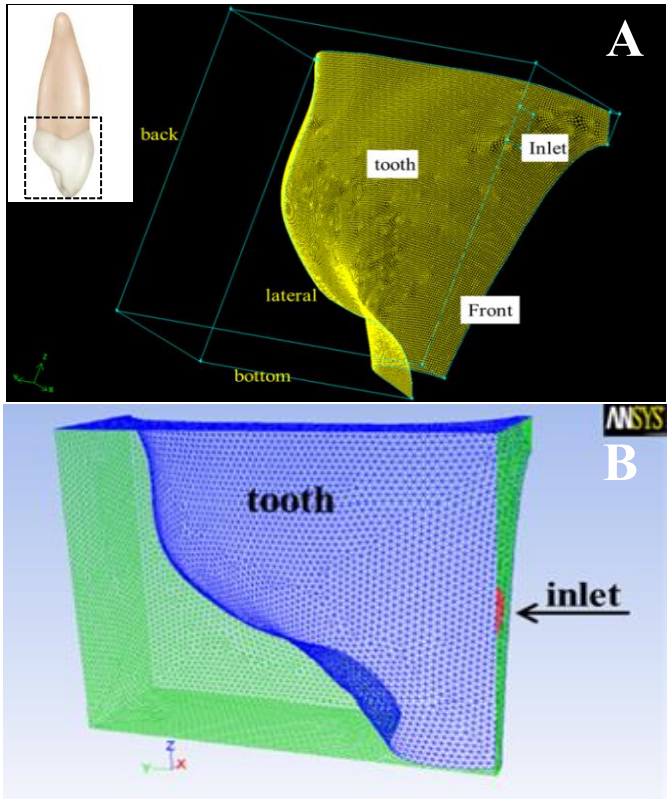

Figure 5.4 A) The 3D meshwork showing the geometry of the proximal surface of the tooth (small panel) that was used for the computational simulations. B) Positioning of the PT-*AirFloss* with respect to the meshwork. ANSYS software was used to run the simulations.

Simulations were carried out on Iridis 3, a Linux-based cluster composed of 1008 Intel Nehalem compute nodes with two 4-core processors. A mesh independence study was performed in order to select the appropriate element size, and determine the optimal compromise between solution accuracy and computational time (Figure 5.5). As a critical response for the study and using an in house developed MATLAB-based code (The Mathworks Inc., US), we estimated the tooth coverage area ($A_{1.7}$ %, calculated as a percentage of the total area) in which the wall shear stress was greater than 1.7 Pa which is the highest $CDSS_{agg}$ value measured experimentally (1.7 Pa), and which was selected as a critical biofilm detachment shear stress to illustrate where on the tooth detachment was expected to occur for all the remaining simulations.

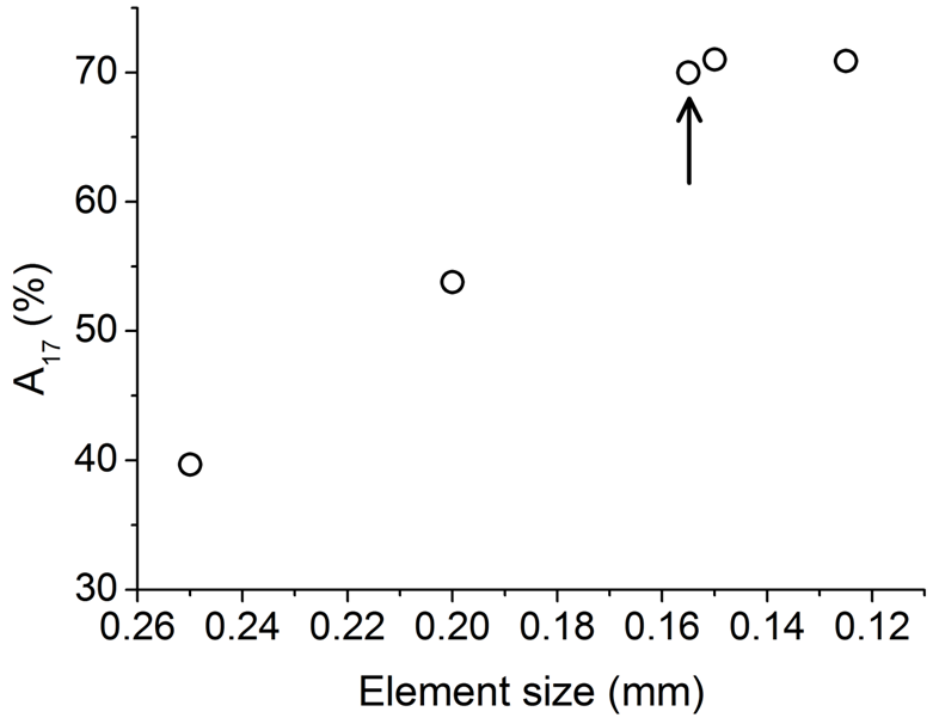

Figure 5.5 Mesh independence study. The percentage area of the tooth where the fluid shear stress was > 1.7 Pa ($A_{1.7}$) was calculated at various mesh element sizes, between 0.125 mm and 0.25 mm. The onset of a plateau was detected at the mesh element size of 0.155 mm, which was selected for the numerical simulations described below.

In the first series of simulations, the flow dynamics of the PT-*AirFloss* in the IP space was investigated. In particular, fluid velocity fields within the IP space, τ_w spatial distribution on the tooth surface, and tooth coverage area were quantified.

In a second series of simulations, the effect of changing the PT-*AirFloss* position (z-position) and the nozzle shape (Figure 5.6) on τ_w distribution was studied.

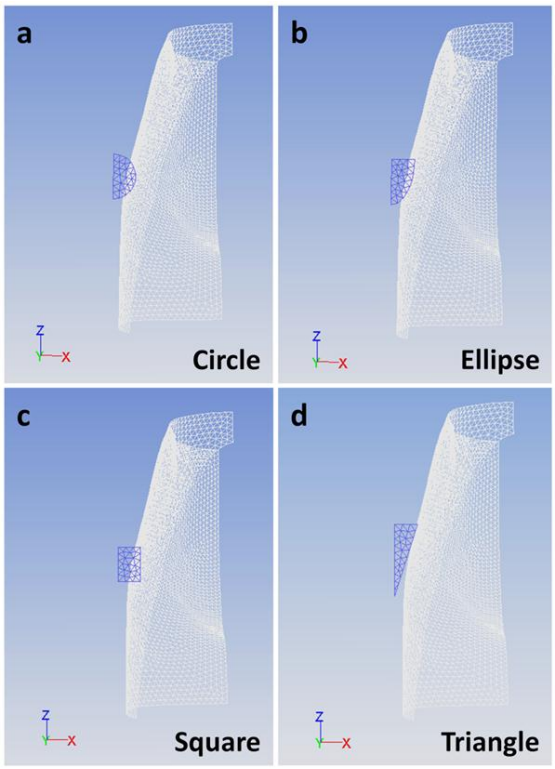

Figure 5.6 Design of different nozzle tip shapes for comparative evaluations. (a) Circular, (b) Elliptical, (c) Square and (d) Triangular cross-sections (blue) were designed for this purpose and meshed with triangular elements for flow dynamic investigations.

5.3. RESULTS

5.3.1. 3D imaging of typodont model

High resolution 3D images detailing the microarchitecture of the typodont were obtained using *μ-CT*. Due to differences in the density, the individual typodont components: the plastic teeth, the elastic silicone rubber gums and the plastic holder base of the typodont, were readily distinguishable (Figure 5.1). Because we were able to distinguish the individual components we could computationally disassemble the typodont maintaining the relevant juxtaposition between the individual teeth. Computational meshes of the individual teeth were created without interference from the other typodont materials (gums, base plate or screws).

5.3.2. Characterization of the microburst

Using high speed imaging, videos were recorded showing the burst mechanism of the water µ-drops from the PT-*AirFloss* (supplementary video1). The water stream had an exit velocity of 60 m/s from the tip. Applying this value in equations [1], [2] and [3] we obtain *Re* = 60420 predicting turbulent fluid flow, the *We* was 50449 predicting that the PT-*AirFloss* provided continuous jet flow, and *Oh* was 0.0037 implying negligible fluid viscosity effects on liquid breakup. The total duration of one burst was ~ 40ms. We estimated from the images that ~ 90 % of the water was ejected in the first 10ms. Within 40 ms, flow visualization of the burst showed an initial continuous stream of water which broke up into drops at approximately 10 mm from the tip exit according to Rayleigh breakup [125]. After approximately 10 ms, the steady stream from the tip was later on interrupted by air bubbles produced by the device.

5.3.3. A critical shear stress for biofilm-aggregates detachment

The morphology of the biofilms in the BioFlux^{TM} 1000 microfluidic channels varied markedly between one channel and the other, and also within the same channel (Figure 5.7). Structural heterogeneity is a common feature of biofilms. One common feature was the presence of individual bacteria and the biofilm clusters of different sizes, as seen by the microscopic images.

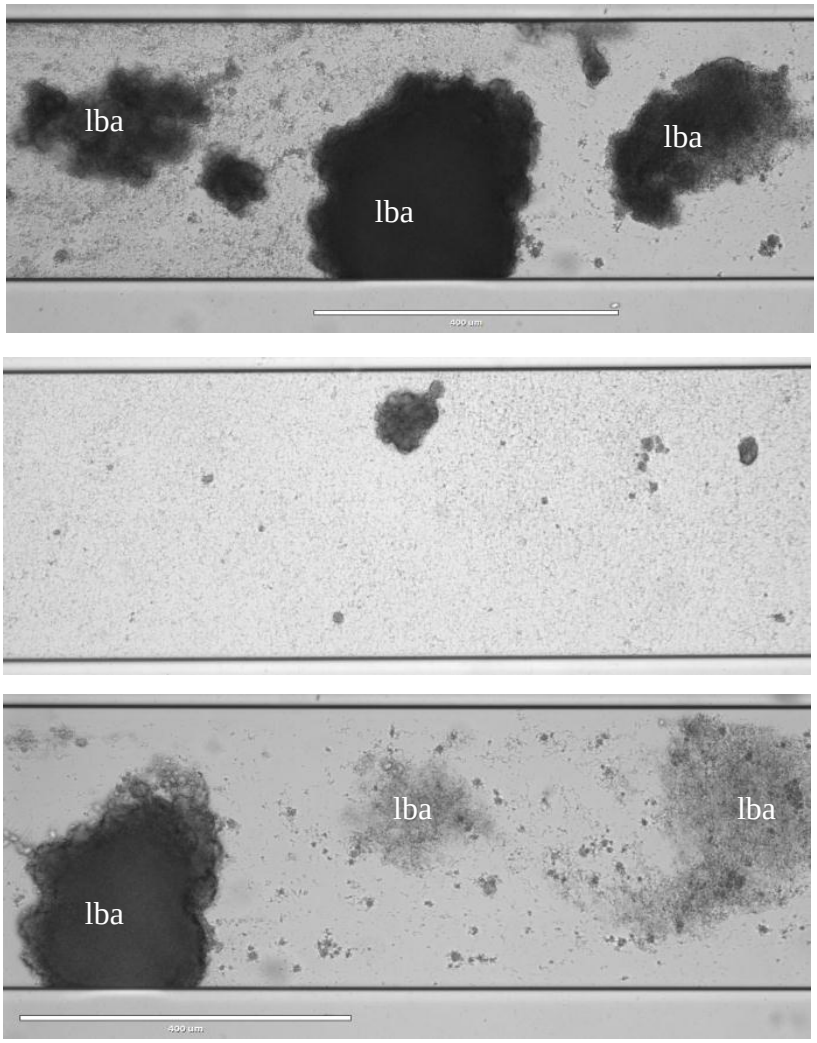

Figure 5.7 Transmitted light images of *S. mutans* biofilms inside the microfluidic channels. The three images were taken, using the EVOS microscope with the 10 × objective, from three different channels. The large biofilm-aggregates are labelled "lba". Scale bars = 200 μm.

When the fluid wall shear stress was increased from 0 to 2 Pa, there was a slight increase in the overall detachment rate of the biofilm (Figures 5.8 and 5.9). Overall, there was a minimal detachment of the biofilm (individual bacteria and the small aggregates) over the applied elevated shear stress. However, the detachment of the larger biofilm clusters (with diameters over approximately 50 μm) occurred when the shear stress reached a shear stress which ranged from 0.3 to 1.7 Pa. From these data we used a conservative "critical biofilm-aggregates detachment shear stress" ($CDSS_{agg}$) of 1.7 Pa for the computational modelling. Above 2 Pa the smaller biofilm

clusters still appeared to be firmly attached to the substrate, and remained attached even after increasing the shear stress to 3 Pa.

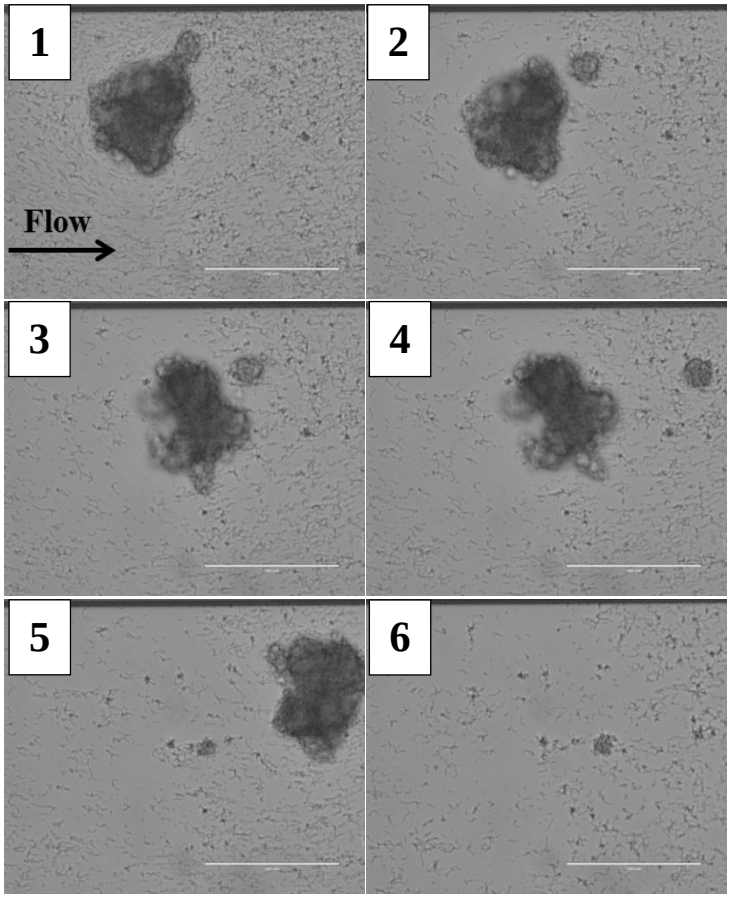

Figure 5.8 Microscopic images from a time-lapse sequence captured using transmitted light mode, of a *S. mutans* biofilm inside microchannels. The biofilm aggregate in the above images was exposed to an increased fluid shear stress, and the black arrow indicates the flow direction in the channel. As the sequence progresses, a small part of the cluster detached first, then the whole aggregate begin to roll and detach at 0.3 Pa for this particular sequence. Scale bar =100 μm.

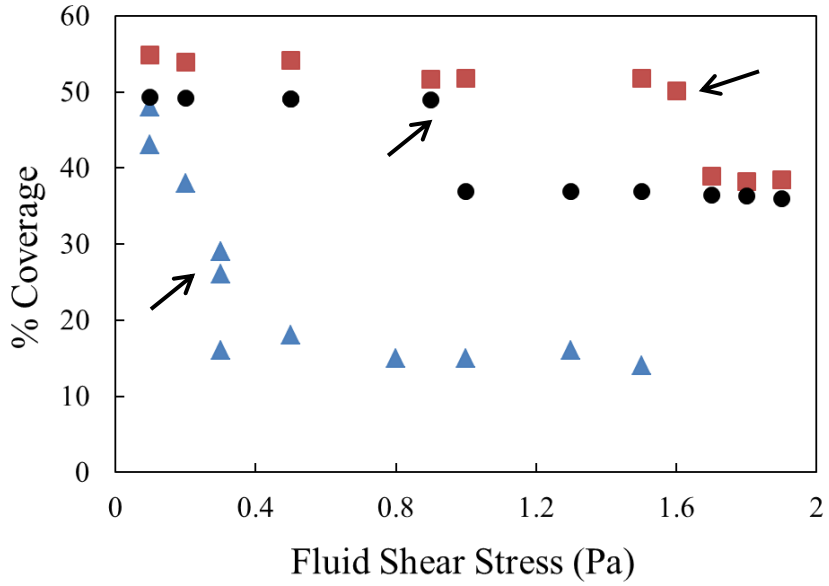

Figure 5.9 Percentage area coverage of the biofilm versus the shear stress (Pa). The percentage coverage was obtained by analysing selected images from the video sequences, using ImageJ. The lower curve (triangles) corresponds to the sequence in Figure 5.8 where the main detachment happened at a shear stress of 0.3 Pa, while the two upper curves correspond to other sequences where the main detachment occurred at 1.0 and 1.7 Pa, respectively. The three black arrows point to the part on each of the three corresponding curves where the main detachment event occurred. The different values obtained for the critical shear stress were used in our CFD simulations.

5.3.4. Visualization of the dextran gel detachment

Videos were recorded showing the burst mechanism of the water µ-drops from the PT-*AirFloss* causing the detachment of the dextran gel (supplementary video 3). The videos demonstrated two detachments mechanisms of the surrogate biofilm. The impact of the water burst caused either the whole surrogate to be fully detached from the surface (Figure 5.10), or opened a hole through the middle of the surrogate and as the stream flowed through it dragged the gel with it stretching the gel which initially remained connected to the back of the corresponding teeth, as we have shown previously [17]. The gel was elongated to more than 900 % (± 100; n = 3) of its original length before breaking. The immediate impact pressure exerted on the gel was estimated as 10.22 MPa calculated using equation [4].

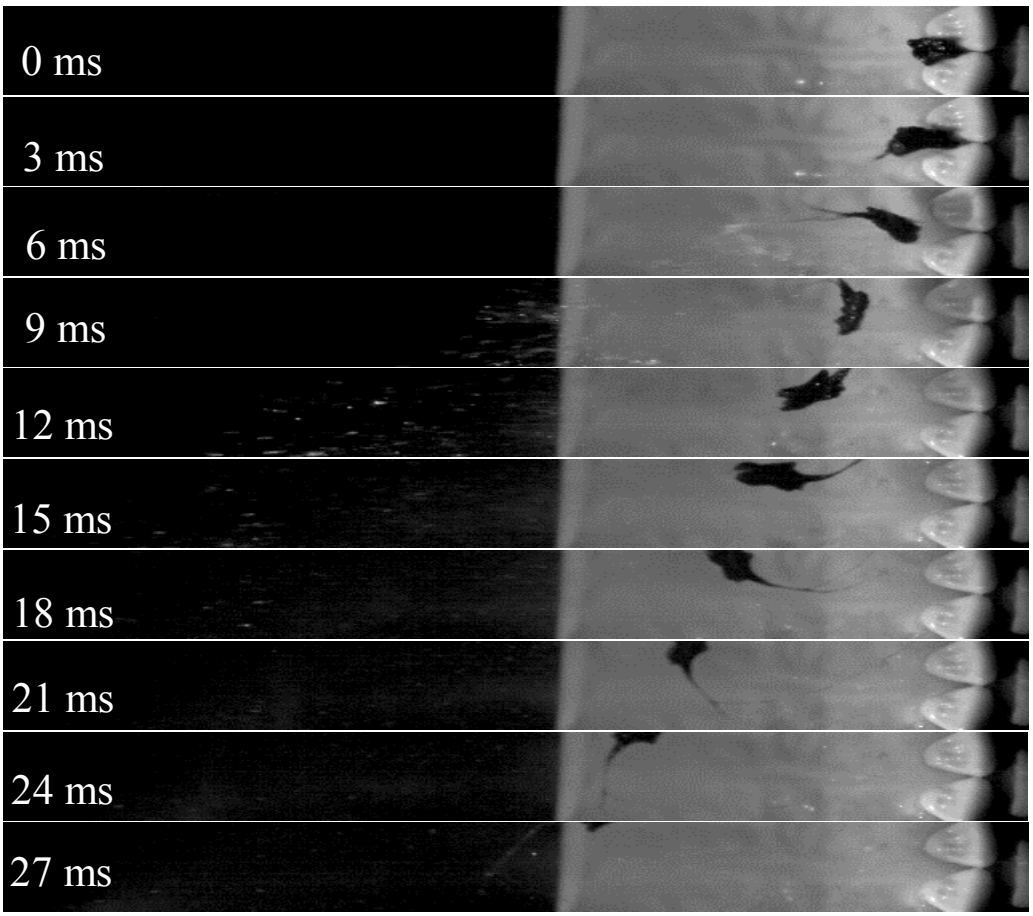

Figure 5.10 Stack of consecutive high speed images showing the PT-*AirFloss* burst (in the direction of the white arrow) impacting the IP space between the central incisors of the typodont, where the dextran gel was applied. The images show the mechanism of adhesive detachment from the tooth surface.

5.3.5. Numerical Simulations

1) Mesh independence study

A mesh independence study was performed in order to investigate the effect of the mesh element size (or total number of elements) on the calculated numerical solution. Five different meshes were designed for this purpose; the element size was varied from 0.25 mm (coarse mesh) to 0.125 mm (fine mesh).

A parameter of interest was quantified at the different mesh element sizes investigated, which corresponded to the surface area (in percentage of total area) of the tooth where the fluid shear stress was > 1.7 Pa ($A_{1.7}$). A circular nozzle tip cross-section was designed for this purpose. The tip was located at a relative z-position, z/H = 0.5.

The analysis showed that $A_{1.7}$ reached a plateau level at 0.155 mm element size (point of convergence) (Figure 5.5). Lower element sizes resulted in only slight percentage variations of the numerical solution (0.56 % maximum deviation). An element size of 0.155 mm was selected for further numerical studies**.**

2) Quantification of wall shear stress distribution

A representative contour plot of the fluid τ_w spatial distribution on the tooth surface is shown in Figure 5.11. This simulation corresponded to a velocity inlet of 60 m/s, with the circular nozzle tip located at z/H=0.5, gingivo-incisally, where *z* (mm) is a spatial coordinate from the supragingival base of the tooth to the tip of the tooth perpendicular and *H* (mm) is the supragingival height of the tooth. Thus z/H=0.5 equates to halfway up the tooth. The simulation showed the predicted fluid τ_w distribution on the proximal surface of the tooth starting from the labial side of the IP space close to the nozzle tip (2.7 kPa), to the midpoint of the palatal surface of the tooth (0.3 kPa).

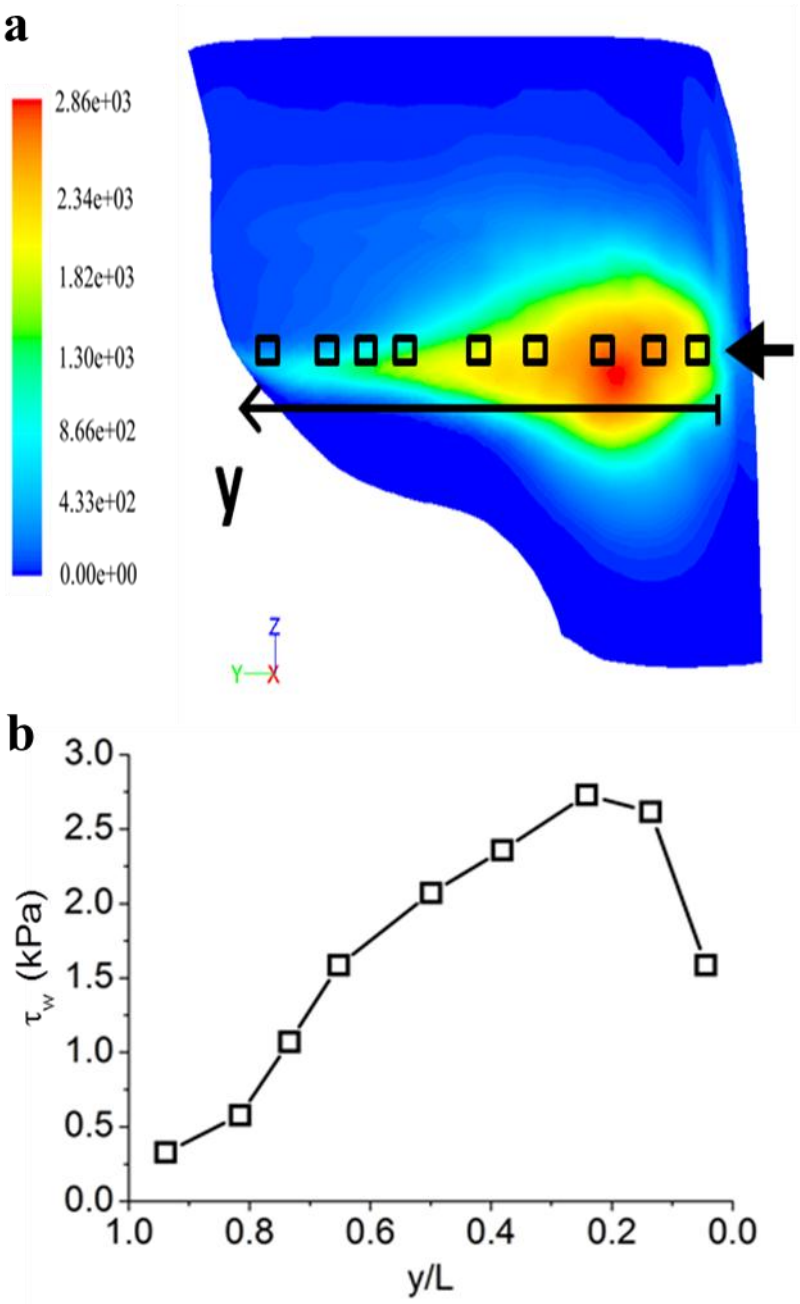

Figure 5.11 (a) Contours of τ_w distribution over the tooth surface, as determined from CFD simulations, with y being the location on the proximal side starting from the labial to the lingual side. The vertical coloured scale on the left represents the values for the shear stress obtained by the simulations. (b) The y-axis represent the τ_w values (in kPa) along the tooth (or y/L on the x-axis, where L being the fixed distance from the labial to the lingual side) at a fixed nozzle tip z-position (z/H = 0.5). The black squares in (a) correspond to the ones in (b).

3) Effect of the nozzle z-position on τ_w distribution

Contours of τ_w on the tooth surface at five nozzle tip z-positions were obtained in order to investigate the effect of tip positioning on the device hydrodynamic performance. Figure 5.12 shows the tooth surface area where τ_w is lower than the critical value of 1.7 Pa. Computational results predicted that the maximum % of biofilm removal would take place when the PT-*AirFloss* nozzle tip is placed at z/H = 0.5 or z/H = 0.66, while the efficacy of biofilm removal would be significantly reduced at extreme z/H positions, namely z/H = 0.17 (i.e. close to gingival margin), or z/H = 0.83 (i.e. close to the incisal edge).

Figure 5.13 shows the different distributions of streamlines at different nozzle z-position. These streamlines correspond to the trajectories of massless particles released from the nozzle tip. Also, the corresponding distributions on the tooth surface are shown for different nozzle z-position.

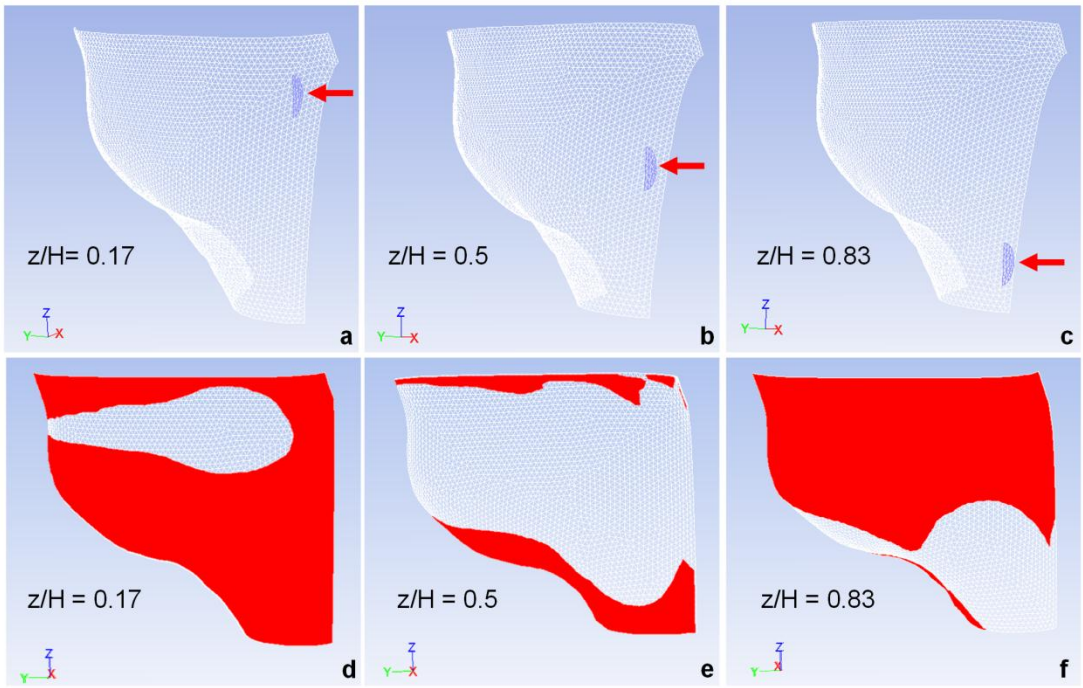

Figure 5.12 Effect of nozzle tip z-position (z/H) on τ_w spatial distribution over the tooth surface. The tip cross-section was circular with a diameter of 1.1 mm, and z/H was varied between 0.17 and 0.83 (a-c). The red arrow indicates the flow direction. The red area in (d-f) corresponds to the tooth surface area where τ_w is lower than $CDSS_{agg}$ = 1.7 Pa, for the different z-positions investigated.

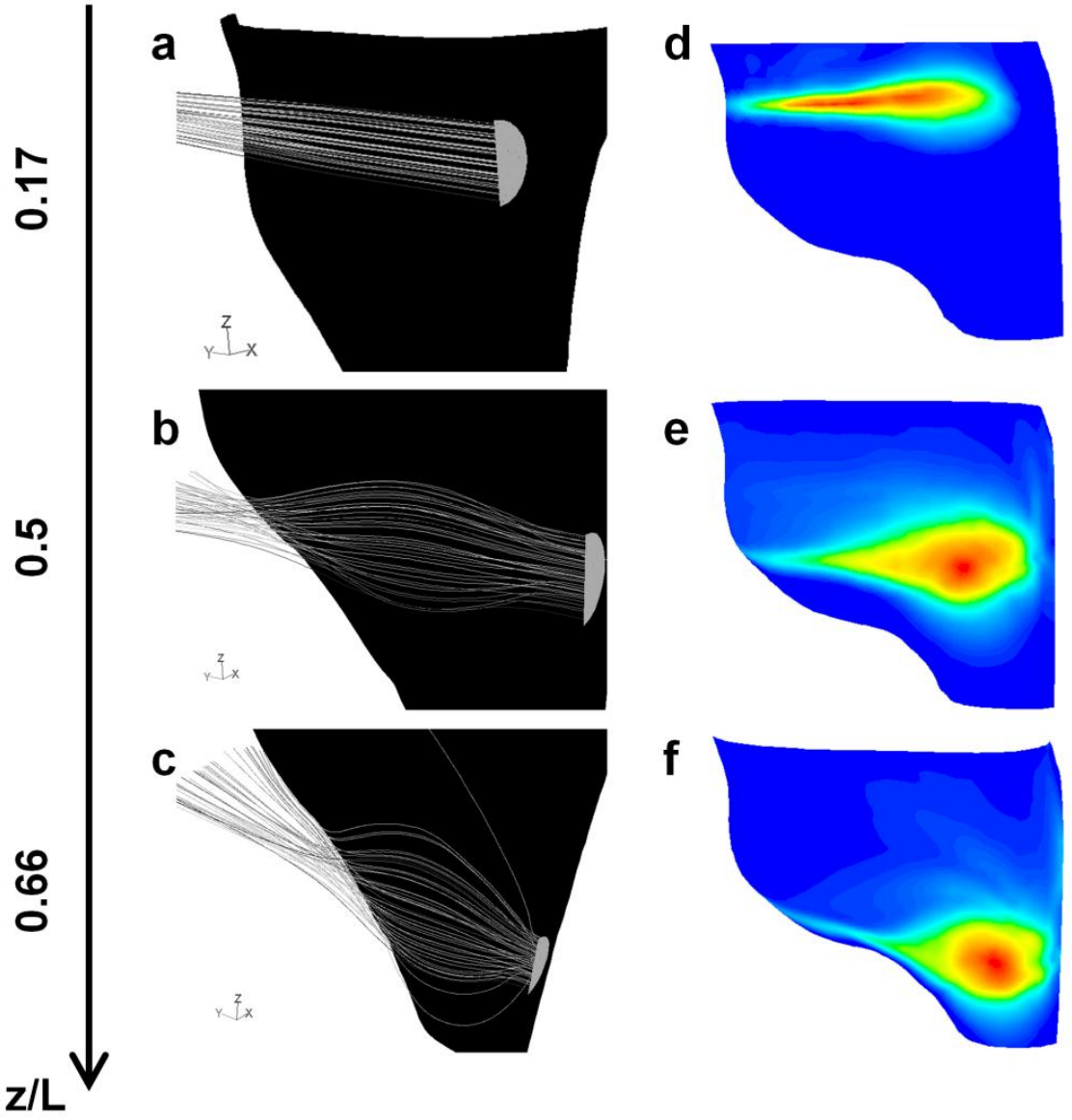

Figure 5.13 Effect of nozzle z-position on the hydrodynamics within the interproximal space. Distributions of streamlines at z/H = 0.17 (a), 0.5 (b) and 0.66 (c)

are reported. Streamlines correspond to the trajectories of massless particles released from the nozzle tip (i.e., inlet). Corresponding τ_w distributions on the tooth surface are shown in panels (d), (e) and(f).

4) Effect of the nozzle shape

Contours of τ_w on the tooth surface at four different nozzle tip cross-sectional shapes: square, elliptical, circular or triangular, were obtained to investigate the effect of changing the nozzle tip shape on the τ_w spatial distribution (Figure 5.14). The red area shows the tooth surface area where τ_w was lower than 1.7 Pa, at the different tip shapes investigated at a fixed tip z-position.

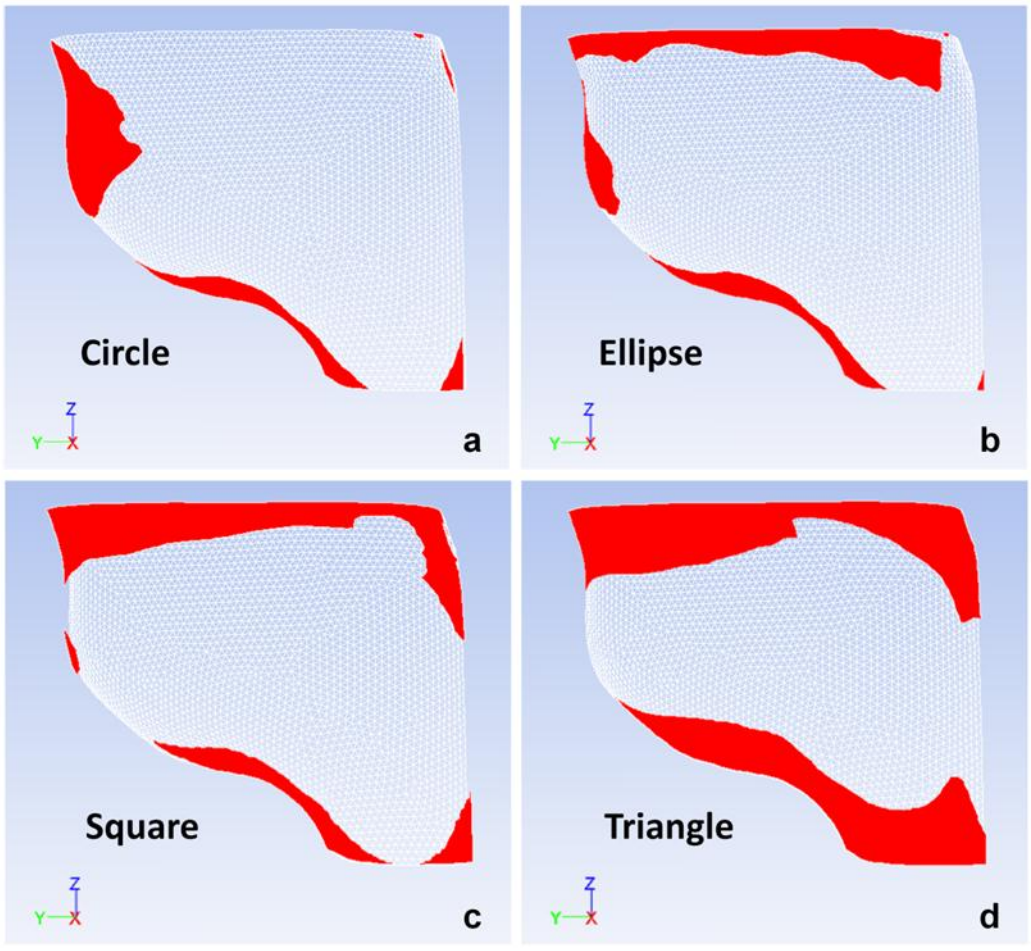

Figure 5.14 Effect of nozzle tip shape on τ_w spatial distribution over the tooth surface. The red area corresponds to the tooth surface area where τ_w is lower than $CDSS_{agg}$ = 1.7 Pa, for the different tip shapes investigated (at a fixed z-position, z/H = 0.5).

The combined effect of the nozzle tip z-position and cross-sectional shape on the PT-*AirFloss* hydrodynamic behaviour (i.e. $A_{1.7}$ values) is summarized in Figure 5.15. In all the examined cases (i.e. four cross-sectional shapes), $A_{1.7}$ displayed a similar trend with respect to the *z*-position. However, since the precise control of the nozzle z-position is practically difficult to achieve in the real-life application, a parameter describing the generalised removal performance of the PT-*AirFloss* device was introduced (referred to as **reliability factor**, ϕ). This has been calculated as the area bounded by the line joining the numerical $A_{1.7}$ values at the different z-positions (Figure 5.15c), using an in-house MATLAB-based code. The ϕ values were normalised with respect to the maximum value (which corresponded to a circular shape of the nozzle). Results show that: $\phi_{\text{circle}} > \phi_{\text{square}} > \phi_{\text{ellipse}} > \phi_{\text{triangle}}$.

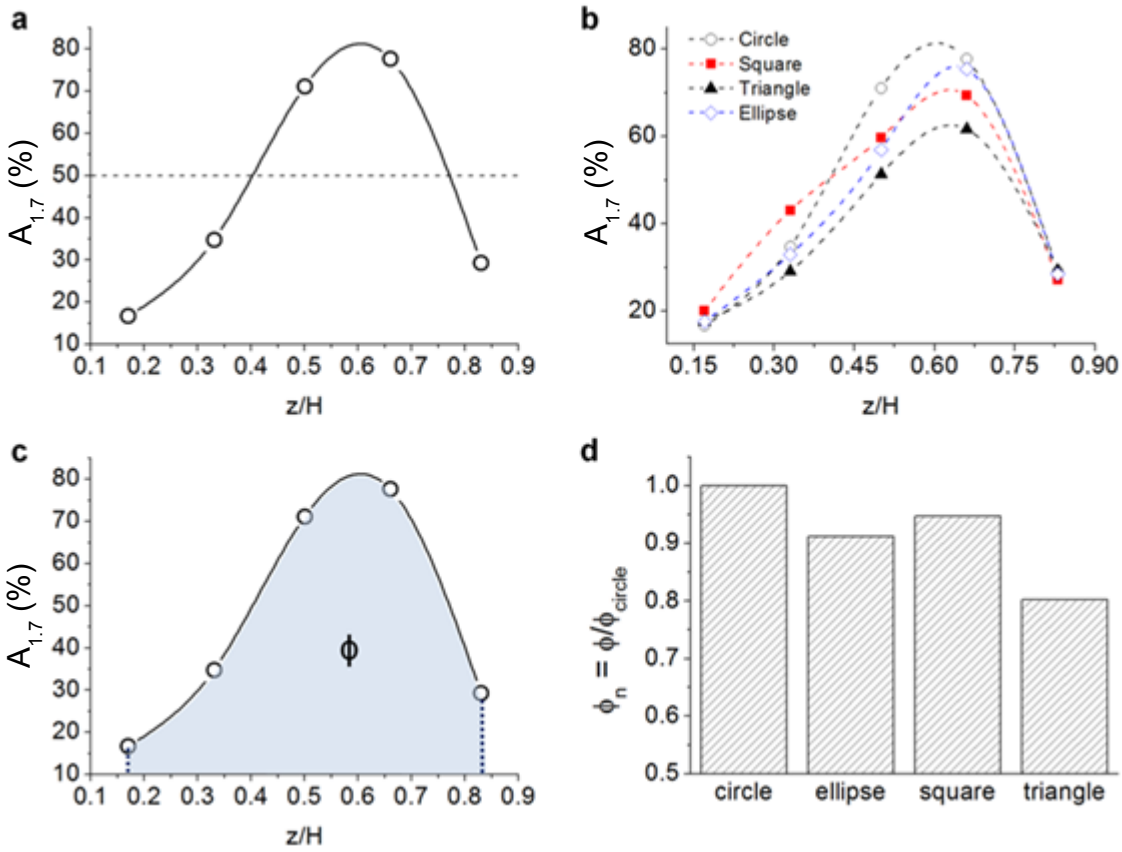

Figure 5.15 (a) Percentage of tooth surface area where the fluid τ_w was > $CDSS_{agg}$ = 1.7 Pa ($A_{1.7}$), at different z-positions of the circular nozzle tip. (b) $A_{1.7}$-z/H trend for the different tip cross-sectional shapes investigated. (c) Calculation of the reliability factor (ϕ) defined as the surface area bounded by the $A_{1.7}$-z/H curve. (d) Reliability factor for the different tip cross-sectional shapes investigated. Values were normalised with respect to ϕ_{circle}.

5.4. DISCUSSION

The high velocity water droplets released from the PT-*AirFloss* device were too fast to be seen by the naked eye (supplementary video 1). Their flow motion was captured using the high speed videography techniques which allowed us to generate novel footage showing the entire microburst mechanism. Analysing these videos allowed us to calculate the exit velocity of the water µ-drops from the PT-*AirFloss*, which was used to calculate Re, We, and Oh numbers and extract relevant information about the flow regime. The calculated values obtained for Re and We within the nozzle tip suggest that the fluid flow at the tip exit is turbulent and continuous. The Oh number within the nozzle tip implies that direct effects of liquid viscosity on liquid breakup were negligible, this was consistent with the video evidence [142]. It is worth noting here that the water drops were generated using a PT-*AirFloss* which has a different nozzle shape, tip diameter, and different water volume per burst compared to the commercially available product, the Sonicare HX8111 *AirFloss* (POH, Seattle).

Videos of the detachment of the surrogate plaque under high velocity water drops were also recorded (supplementary video 3). The device bursts a mixture of air and water, and the recorded videos demonstrated the presence of two phases: a) an initial continuous behaviour of the water flow of the burst (duration: 10 ms) and b) the ejection of air bubbles causing the water droplets to split into nanodrops (duration: 30 ms). In the presence of the dextran gel in the IP space, the videos demonstrated two mechanisms of detachment. In the first detachment mechanism, the burst totally detached the dextran gel from the tooth surface under the effect of the initial impact (Figure 5.10). In this case, the cohesive force within the gel overcame its adhesive strength to the tooth surface. In the second mechanism of detachment, the impact of the burst water droplets caused the substrate to be stretched before the main part detached; however, gel remained attached from the tooth surface and carried away with the fluid stream [17]. This behaviour is typical of a viscoelastic material, such as bacterial biofilms. In minimal time (< 15 ms), and using minimal water volume (115 µL), we previously estimated that more than 90 % of the dextran gel was removed from the IP space. The removal process of the dextran gel by bursting pressure-driven high velocity water droplets can be characterized by two phases. First, the stream impacts the plaque causing its immediate detachment at the impact site while creating a hole through cohesive failure. After that, the water droplets penetrate through the

hole creating a shear stress within the gel, while dragging it along with the stream, causing the gel to elongate before breaking away from the tooth surface. A critical shear stress was needed to remove the biofilm. In our current study, the droplets velocity was 60 m/s measured at the device outlet section, and the generated fluid shear stress proved to be highly effective in removing the attached surrogate biofilm. However, remnants of the gel remained on the back of the teeth, due to teeth architecture and the fluid flow behaviour in these regions, i.e. the inability of the fluid to flow around the anatomical curvature and undercuts associated with the palatal surface of the upper central teeth. These observations were predicted by the computational simulations in which τ_w on the proximal surface of the teeth was observed to decrease gradually in the labio-palatal direction.

The μ-CT imaging enabled the creation of detailed 3D images for the typodont and the IP space located between the two upper central incisors (i.e. region of interest for modelling purposes). The reconstructed 3D geometry of the IP space was used for CFD simulations which predicted the shear stress distribution over the teeth surfaces: the highest shear being closer to the nozzle tip, while the lowest shear being located at posterior aspect of the teeth (Figure 5.11).

The developed computational model allowed the prediction of the effect of changing the position of the nozzle tip in the z-direction (inciso-gingivally) and the shape of the tip cross-section on biofilm removal efficacy. The numerical simulations predicted that placing the nozzle tip in or close to the middle of the inciso-gingival height (z-position, z/H = 0.5 or 0.67) provides more effective biofilm removal, in comparison to placing the tip closer to either the incisal edge or the gingival line (Figure 5.12). This difference in the efficacy of removing biofilm is due to the different fluid streamlines produced when the nozzle is placed in different z-position in the IP space (Figure 5.13). A novel coefficient (reliability factor Φ) was also introduced, which provides a quantification of the device hydrodynamic performance independently from nozzle tip positioning (Figure 5.15). It can be used to evaluate the performance of different removal strategies (i.e. different nozzle tip shape, exit velocity) for comparative analyses. Numerical simulations also predicted that the circular nozzle tip was more effective in removing biofilms from the tooth surface than all the other shapes investigated (Figure 5.14), and this was reflected by increased reliability factor values.

To the best of our knowledge, this is the first time that CFD has been used to calculate τ_w distribution, caused by water drops generated from an oral hygiene device, on the tooth surface.

In the flow cell experiments, *S. mutans* biofilms were successfully grown inside microchannels under gravitational flow conditions. Using transmitted light microscopy (Figure 5.7), the biofilms size and morphology showed similar resemblance to previously reported data [143]. When these biofilms were subjected to an increased shear stress from 0 to 2 Pa, the large aggregates resisted movement from the surface until the wall shear stress reached a critical value (critical biofilm-aggregates detachment shear stress, or $CDSS_{agg}$), which ranged between 0.3 and 1.7 Pa, at which they detached (Figure 5.9). However, even at this critical value, the smaller biofilm patches and individual bacterial cells remained attached. Generally, detachment of biofilm fragments (erosion), or even of the entire biofilm (sloughing), are caused by high flow shear stress levels that exceed the adhesion strength of the biofilm [139] [76]. The detachment of the large aggregates occurred at a relatively low shear stress (~1 Pa), while the smaller patches remained firmly attached, even after increasing the flow up to 3 Pa. So, the $CDSS_{agg}$ estimated here describes the detachment involving large aggregates only, and not the total biofilm which requires a higher critical shear stress for detachment which was beyond the range of the microfluidics system under our operating conditions. The critical shear stress value of 1.7 Pa is close to the range of previously reported values of shear stress (5-12 Pa) required for detachment of non-dental biofilms [68] [139].

The simulations predicted τ_w distribution on the tooth surface caused by the microburst to be in the kPa range within the IP space, except in areas on the palatal side of the tooth where τ_w became significantly lower (~ 200 Pa). The maximum computational values for the fluid τ_w were ~ 1000 times higher than the $CDSS_{agg}$ obtained from the flow-cell experiments, and ~ 200 times higher than the estimated shear stress, reported in literature, for biofilm detachment [139] [68]. Thus, the simulations predict that a significant percentage area of the tooth is subjected to τ_w values capable of removing the *DPBs* from the IP spaces. These predicted values represent a challenge when it comes to replicate them in flow cell experiments. The

flow cell system that was used could reach up to 20 Pa as a maximum shear stress on the substrate. In order to validate the computationally obtained values, experiments were conducted using real *S. mutans* biofilms in the IP space aiming at quantifying the detachment process. The experimental results will be compared to the computational studies, with the main objective being the establishment of a semi-empirical analytical relationship between the applied shear stress and biofilm removal, which would simplify the direct quantitative measurement of biofilm detachment. This will be explained in the next chapter.

5.5. CONCLUSION

The detachment of *DPBs* with high velocity water μ-drops was studied in the laboratory using a surrogate plaque. An experimental setup was built and a methodology was developed to characterize and visualize the microburst. The impact of the water drop was high enough to cause adhesive and cohesive viscoelastic failure contributing to the detachment process. High velocity water μ-drops can effectively detach biofilms with minimal volume and time.

The 3D numerical simulations predicted the shear stress value and spatial distribution over the teeth surface in the IP spaces. Changing the shape and location of the nozzle tip with respect to the IP space significantly changed the outcome of the device burst. Biofilms grew from *S. mutans* inside microfluidic channels. It was found out that it is easier to detach larger biofilm aggregates at reasonably low fluid shear stresses than it is for the smaller colonies and individual bacteria that are more strongly adhered to each other, to the EPS matrix, and to substrate.

Chapter 6

6. Removal of interdental biofilms by high-velocity water µ-drops

6.1. INTRODUCTION

Dental caries is formed in part due to acids produced by oral bacteria metabolizing fermentable sugars such as sucrose, glucose or fructose [116] [144]. The formation of dental plaque biofilms (*DPBs*) by these bacteria, plays a major role in the aetiology of dental caries [145]. Microelectrode studies show that through respiration and fermentation acidophilic bacteria in dental plaque biofilms can create highly localized acidic anaerobic microenvironments on the underlying enamel where the pH can drop below 5 within 5 minutes of a sucrose pulse [3]. If allowed to proliferate, at or below, the gum line *DPBs* can also cause gingivitis and periodontitis, and are also associated with low birth weight and endocarditis [146].

Mechanical removal through twice daily tooth-brushing is an established method of managing *DPBs*, however, even with good practice plaque can build up in difficult to reach areas. String flossing is used to help remove DPB from the interproximal spaces between the teeth and prevent their build-up which results in class II cavities in the proximal surfaces of the teeth. Another mechanical approach for controlling biofilm accumulation is fluid shear stress. Biofilm detachment can be stimulated by generating sufficiently high fluid shear stresses [132]. Entrained air bubbles [102] [133] and high velocity water droplets [135] have also been shown to be able to remove bacteria and biofilms from surfaces utilizing the additional effect of generating a "surface-tension force" away from the surface by the passage of an air/water interface [62] [116]. An advantage of using fluid forces to remove biofilms is that mechanical forces can be projected beyond the device itself by generating currents in the fluid surrounding the teeth by powered brushing [140] or through the generation of water jets by oral irrigation [141]. More recently the Sonicare™ *AirFloss* device has been introduced for removing IP DBP. The *AirFloss* shoots a small volume (115 µL) of water and some entrained air at high velocity between the

IP space in a discrete burst, thus creating high shear stresses and high impact pressures over short periods of time minimizing water volume and cleaning times.

In this chapter we present an experimental and numerical study on the influence of a high-velocity water microdrop impact on the detachment of *Streptococcus mutans* biofilms from the IP spaces of a typodont model. Using high speed digital videography [118], the detachment process of *S. mutans* biofilms was captured. Image analysis was used to quantify the amount of biofilm removed as a function of time over the burst period. We used 3D confocal laser scanning microscopy (CLSM) to compare biofilm at different locations on the typodont before and after exposure to a PT-*AirFloss* microburst. X-ray microcomputed tomography (μ-CT) was used to image the typodont in 3D in order to produce an anatomically correct reconstruction of a representative IP space. Computational fluid dynamics (CFD) numerical techniques were employed to model and predict the spatial distribution of fluid wall shear stress (τ_w) over the tooth surface by varying the nozzle placement. There was a linear relationship between the predicted τ_w and the measured biofilm removal from the IP surface of the typodont.

6.2. MATERIALS AND METHODS

6.2.1. Bacteria and growth media

Biofilms from *Streptococcus mutans* UA159 (ATCC 700610) were grown. *S. mutans* is a facultative anaerobic, Gram-positive acidophilic bacterium, and an early colonizer of the tooth surface. *In vitro* biofilms grown from *S. mutans* are widely used to model an early stage cariogenic human dental plaque [68]. Stock cultures of *S. mutans* were stored at -80^{o}C in 10 % glycerol in physiological buffered saline (PBS). Biofilms were cultured using sucrose supplemented brain heart infusion (BHI+S) medium (Sigma-Aldrich, The United Kingdom) and incubated at 37^{o}C, 5 % CO_2.

6.2.2. Typodont model

To recreate a realistic geometry associated with the IP space biofilms were grown on the two upper centrals (teeth 8 and 9) removed from a training typodont (Frasaco A-PZ periodontal dental model 4030025). The teeth were autoclave sterilized at a

temperature of 121^{o}C for a minimum of 45 minutes. The teeth were placed in either a 90 mm petri plate or later a 15 mL Falcon tube, which was found to be more convenient. An inoculum was prepared in the Falcon tubes by adding 0.5 mL of *S. mutans* from the stock solution to 10 mLs of sterile BHI+S. When using petri plates, 1 mL of the stock solution was poured over the teeth, and sterile medium was added until the teeth were completely submerged (Figure 6.1 A). For seven consecutive days, the medium was refreshed and fresh medium with a new bacterial inoculum was added daily. After the growth period, the teeth were removed using sterile tweezers making sure that the proximal surfaces of the adjoining teeth, which constitute the IP space, were handled carefully to avoid any scratches. The two teeth were repositioned into the typodont, to recreate a correct anatomical spatial relationship. The assembled typodont teeth were allowed to incubate a further five days with daily medium and inoculum refreshment to allow the biofilm to naturally bridge between the IP space between the separate teeth.

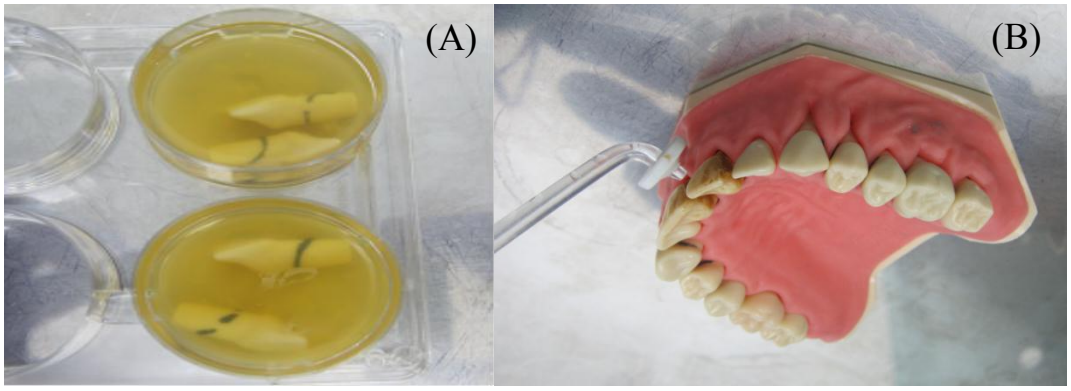

Figure 6.1 (A) Photograph showing the typodont teeth (8 and 9) in a 6-well plate. Fresh media and a new bacterial inoculum were added daily, for 7 consecutive days, to grow the biofilm in the IP space. (B) Position of PT-*AirFloss* with respect to the typodont facing the labial side of the teeth. The photo has been rotated 180^{o} to show the position as it would be when applying the PT-*AirFloss* against the teeth of the maxillary dental arch in actual use.

6.2.3. High speed videography and microburst

A prototype Sonicare *AirFloss* (provided by Philips Oral Healthcare, Seattle) was used to generate a microburst of 115 μL (± 50; n = 30) over a time period of approximately 0.033 s. The PT-*AirFloss* was modified so that it could be triggered remotely to avoid disturbing its position by pressing the button which is the normal operation. The PT-*AirFloss* was positioned in a clamp facing the IP space between the upper central incisors of the typodont (Figure 6.1 B) in accordance with the manufacturer's recommendations. An Ultima 512 high-speed CCD camera (Photron Inc., San Diego, CA, USA), equipped with a KC lens, with a KC-AUX and 1X, 3X or 4X magnifying lenses mounted on top of it (IF-1, IF-3 and IF-4, Infinity, Boulder, CO, USA) depending on the required magnification, was used to capture the bursting process of the PT-*AirFloss*. The high-speed camera can record up to 32,000 frames/s, but has limited memory of 512 MB. A high speed camera was required since the microburst was too fast to be seen with the naked eye, as it takes approximately 1/30 second for the complete process. The typodont was illuminated from the front using optical fibre light sources (MH-100, Dolan Jenner Industries Inc., Lawrence, MA, USA). Videos were recorded with inter frame time intervals (and frames per seconds, fps) of 1.25×10^{-4} s (8,000 fps) or 2.50×10^{-4} s (4,000 fps). The camera field of view was either 512 × 128 pixels, at a 4 × magnification over a physical area of 100 x 10 mm. The bursts were captured in the IP space between the upper central incisors of a typodont which was colonized with *S. mutans*. The experiment was independently repeated 12 times, from these 4 movies were used to quantify the amount of biofilm removed as a function of time. The choice of the 4 movies from the 12 taken was based on: i) the clarity of the images taken and ii) the stability of the field of view during the microburst. The other 8 movies were eliminated because there was displacement between the before and after frames, which made it difficult to use the movies for quantitative measurements.

6.2.4. Quantifying biofilm surface area coverage and removal from the high-speed videos

To quantify the amount of biofilm in terms of surface area coverage, the images obtained from the high speed camera were converted to 8-bit grayscale. To reduce noise the following commands were applied: smooth, enhance contrast, and adjust

threshold so that the biofilm appeared black. The total area selected as biofilm was measured using the "measure" or "analyse particles" command. For quantifying the percentage removal during and after bursting, image subtraction was used. The area defining the IP space area was traced manually and the subtraction of the "after" image from the "before" image was made for the biofilm inside that selected area. For measuring the removal rate over time, consecutive images in a movie were subtracted from each other using the "Stack Difference" plugin. In this case, it was not possible to manually trace the IP space area in each image, due to the large number of images in each stack. So the final values for coverage were plotted in terms of the total surface area of the frame.

6.2.5. Confocal laser scanning microscopy (CLSM)

The amount of biofilm on the IP surfaces of the typodont teeth was measured by a confocal microscopy using a Leica TCS SP2 AOBS (Leica Microsystems, France) Confocal Laser Scanning Microscope (CLSM). The typodont teeth were carefully disassembled after being treated with a PT-*AirFloss* burst. The teeth were then placed in a 35 mm petri dish and stained with the BacLight Live/Dead stain (Invitrogen). After a 15 min incubation period, the teeth were flooded with PBS and observed using either 63x or 48x water immersion objectives (Leica). Teeth not exposed to the PT-*AirFloss* were used as untreated controls. Three images were taken at five evenly spaced different locations (A, B, C, D, and E in Figure 6.2) across the IP space at the level of the PT-*AirFloss* tip from the mesio-labial to the mesio-palatal side. We used an excitation wavelength (λ_{ex}) of 488 nm for both the SYTO9 "live" green stain and the propidium iodide "dead" red stain. The biofilm % surface area coverage was quantified using the NIH software ImageJ (http://rsb.info.nih.gov/ij/), by measuring total area of bacteria (both green and red fluorescence). The images were converted to 8-bit grayscale. To reduce noise, we applied the following commands: "smooth", "enhance contrast", and "adjust threshold" so that the biofilm appeared black. The total area selected as biofilm was measured using either the "measure" or "analyse particles" command. The % removal was calculated by subtracting the amount of biofilm that remained after the microburst, from the original amount of biofilm (i.e. before the microburst). For example, for calculating the % removal of biofilm in a given location A:

Biofilm % Removal = $\left(\frac{A_2 - A_4}{A_2}\right) * 100$

Where A_2 is the amount of biofilm quantified before the PT-*AirFloss* burst, while A_4 is the amount of biofilm quantified after the burst (Figure 6.2).

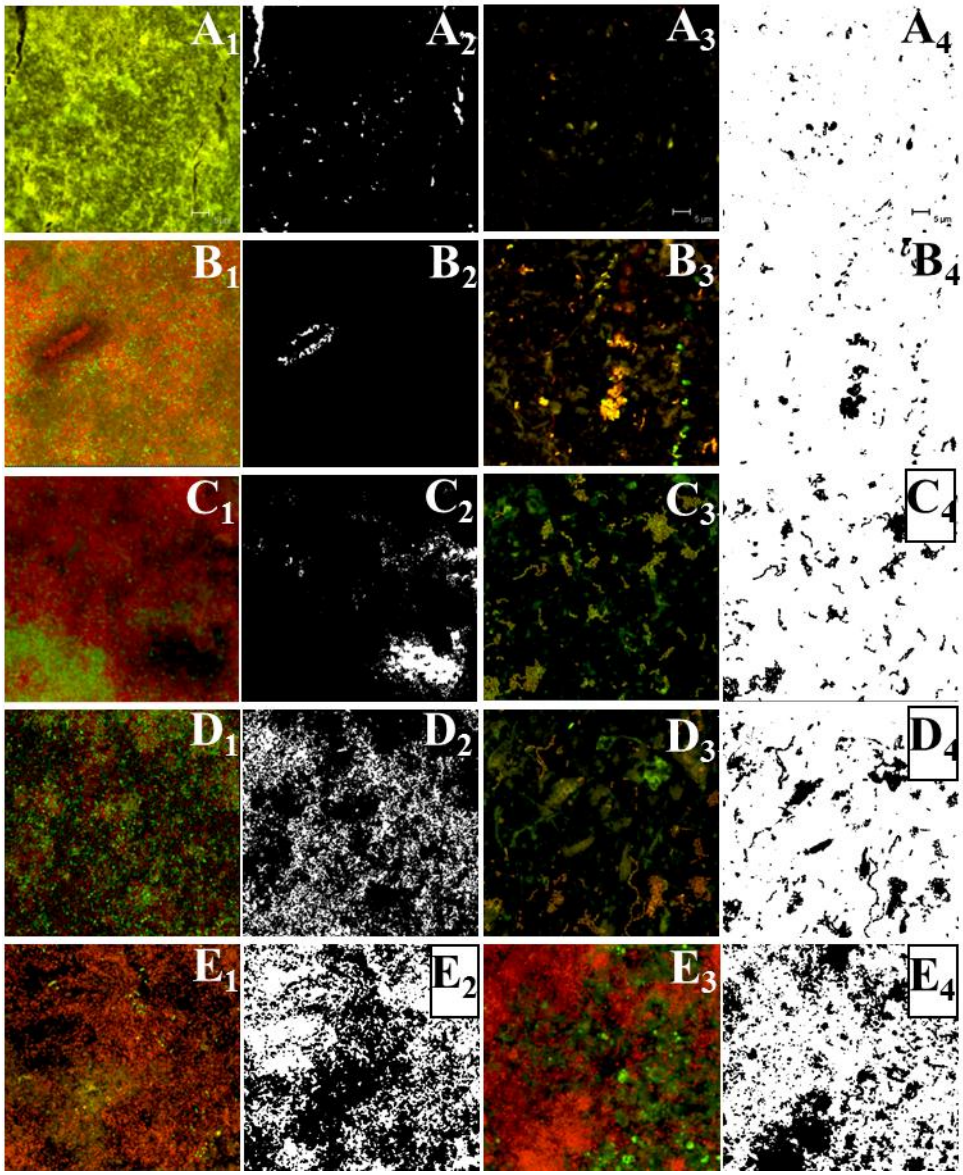

Figure 6.2 Representative CLSM images of *S. mutans* biofilm on five different locations (A, B, C, D, and E) across the IP space at the level of the prototype *AirFloss* tip from the proximo-labial to the proximo-palatal side of a maxillary central incisor (the five locations are identified clearly in Figure 3). A_1, B_1, C_1, D_1 and E_1 are the

images for the biofilm before the burst (on the untreated tooth), and A_2, B_2, C_2, D_2 and E_2 are the corresponding images after thresholding using ImageJ (the biofilm is in black in these images, while the white areas are biofilm-free regions). Meanwhile, A_3, B_3, C_3, D_3 and E_3 are the images for the biofilm on the treated tooth after the burst, and A_4, B_4, C_4, D_4 and E_4 are the corresponding thresholded images. The untreated samples (columns 1 and 2) and treated samples (columns 3 and 4) are not from the same specimens. The % removal was calculated by subtracting the amount of biofilm that remained after from the original amount of biofilm.

6.2.6. µ-CT geometry reconstruction of the typodont model

X-ray microcomputed tomography (µCT) was used to image the typodont in 3D to show the IP space in 3D and for use in subsequent computation fluid dynamics modelling. Images were obtained using an X-Tek Benchtop160Xi scanner (X-Tek Systems Ltd, Tring, Hertfordshire, UK), equipped with a Hamamatsu C7943 X-ray flat panel sensor (Hamamatsu Photonics, Welwyn Garden City, Hertfordshire, UK). The scans were performed using "shuttle" mode, in which the scanner table moves back and forth, at 80 kV and 100 µA, with no filter. The reconstructed volume was 1999 × 2000 × 1540 voxels with 0.0456 mm voxel edge size. The source-to-object distance was 261 mm, the source-to-detector distance was 1140 mm, and the detector size was 2000 × 2000 pixels with 0.2 mm pixel edge size. The exposure time was 2000 ms (4 × gain, no binning). After removing the metallic screws from the typodont, the hard thermosetting plastic teeth, with the elastic silicone rubber gums and the plastic holder base of the typodont were readily distinguishable due to differences in X-ray attenuation by the different materials, so that the individual typodont components could be reconstructed using CT-PRO 2.0 (Metris X-Tek, UK) and visualized using VG Studio Max 2.0 (Volume Graphics, Heidelberg, Germany) to show various aspects of the assembled typodont and the individual teeth while maintaining their spatial relationship (Figure 5.1 B).

6.2.7. Computational fluid dynamics simulations

To model the dynamic behaviour of the microburst created within the IP space, the tomography obtained from μ-CT was converted to a 3D computer aided design (CAD) file geometry using Amira software (Mercury Computer Systems, Berlin, Germany,

http://www.amira.com/). The computational domain, represented by the IP space, was discretized with software Gambit 2.4.6 (Simmetrix Inc., U.S.A.) using tetrahedral meshing scheme. A cell size of ~155 μm was chosen which lead to a total number of 143985 mesh elements. Since the IP space was symmetrical, only half of the IP space was modelled, reducing computational time.

CFD simulations based on the finite element method (FEM) were performed using ANSYS Fluent 12.1.4 software (ANSYS Inc., Canonsburg, PA, USA), which allowed for the determination of the flow field within the IP space and τ_w generated on the tooth surface. An air-liquid interaction to simulate the effects of a water burst moving into an air space was performed by adopting a Volume of Fluid (VOF) multi-phase model, with the surface tension (γ) between air and water set to 0.072 N/m. VOF models are commonly used to perform simulations involving free surface flows with sharp interfaces. In this method, in addition to quantities such as pressure and velocity, a scalar quantity is introduced for each grid element, which represents the fraction of the two phases (i.e. air and water). If an element is filled entirely with water, the VOF fraction is equal to 1; if an element is filled completely with air, the VOF fraction is instead equal to 0. For elements that are partially filled with water, the VOF scalar takes a value between 0 and 1, in accordance with the water fraction. The VOF fraction was transported by means of the advection equation [140]. A steady-state model was used for solving the Navier-Stokes equations within the IP space. Both laminar and turbulent models were tested for this purpose. The robust and economical k-ε model was observed to provide the best convergence of the solution, and was selected for the present numerical study [141]. The experimentally-assessed value of 60 m/s for the exit velocity was used as a velocity boundary condition. A pressure boundary condition in air was set to 1 atmosphere. The teeth and gum surfaces were modelled as rigid walls. The physical properties of water at 20^{o}C were used as previously described.

Simulations were carried out on Iridis 3, a Linux-based cluster composed of 1008 Intel Nehalem compute nodes with two 4-core processors. A mesh independence study was performed in order to select the appropriate element size, and determine the optimal compromise between solution accuracy and computational time (Figure 5.5). In the simulations, the flow dynamics of the PT-*AirFloss* in the IP space was

investigated, and the fluid velocity fields within the IP space and τ_w spatial distributions on the tooth surface were quantified.

6.3. RESULTS

6.3.1. Detachment visualization of the viscoelastic DPBs

When the biofilm was subjected to the bursting action of an empty PT-*AirFloss (i.e. no water, only air burst),* it deformed in the direction of the flow. When the flow was stopped, the biofilm bounced partway to its original position. Videos of this experiment can be viewed in the supporting information on the cd (supplementary video 2). This air-only burst was applied to demonstrate the viscoelastic behaviour of the biofilms. However, for all the remaining experiments, the normal PT-*AirFloss* burst (i.e. device filled with water, as indicated in the manufacturer's instructions) was applied.

Using image analysis techniques for four videos, the percentage removal of *DPBs* in the IP space by the PT-*AirFloss* was 90 % (± 2; n = 4) of the total initial amount, which was obtained by subtracting the images before and after a single PT-*AirFloss* burst (Figure 6.3). The IP space area was traced manually and the subtraction was made for the biofilm inside that selected area. The videos recorded by the high speed imaging techniques showed the burst mechanism of the water µ-drops from the PT-*AirFloss*, and clearly proved the initial continuous-flow behaviour (first 10ms) of water drops which was later on interrupted by air bubbles produced by the device. This caused the water to break up into micro and nanodrops. As estimated from the videos, the large majority of the biofilm was removed by the continuous-flow jet within the first 10 ms.

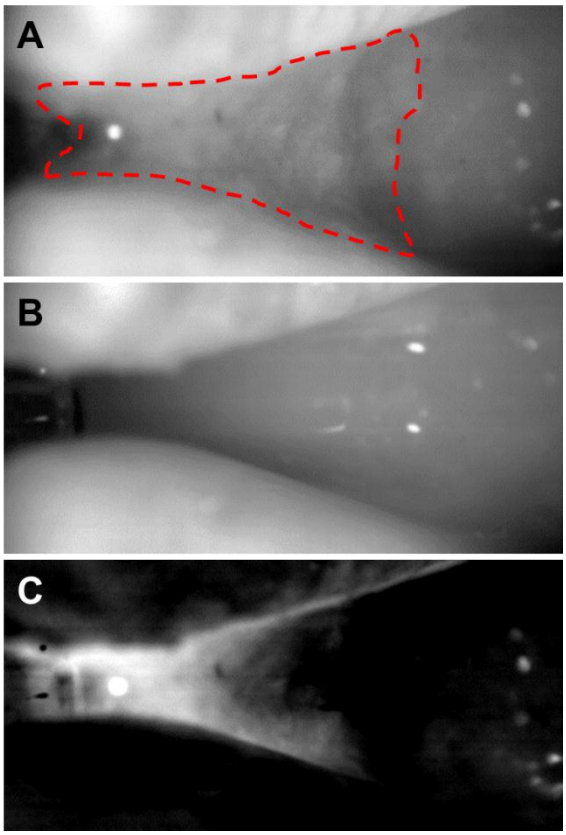

Figure 6.3 High speed camera frames show the removal of a *S. mutans* biofilm from the IP space under the influence of high velocity water droplets. Image analysis was used to subtract the "before burst" image in panel A from the "after burst" image in panel B. The result is shown in panel C. The biofilm that had detached (dashed red line in A) was quantified for four different videos, using ImageJ software.

The detachment of *DPBs* over time was also studied. The analysis of the videos demonstrated the fast removal of the biofilms from the tooth surface. It took approximately 35 ms for the biofilms to be completely removed by water released from one PT-*AirFloss* burst. Using the ImageJ subtraction plugin, the amount of biofilm was quantified frame-by-frame, over the duration of the recorded videos. This resulted in determining the biofilm's coverage area over time. The resulting curves demonstrated decrease in the surface area coverage of the biofilm over time (i.e. increase in the percentage reduction of the surface area coverage of the biofilm over time as plotted in Figure 6.4 B).

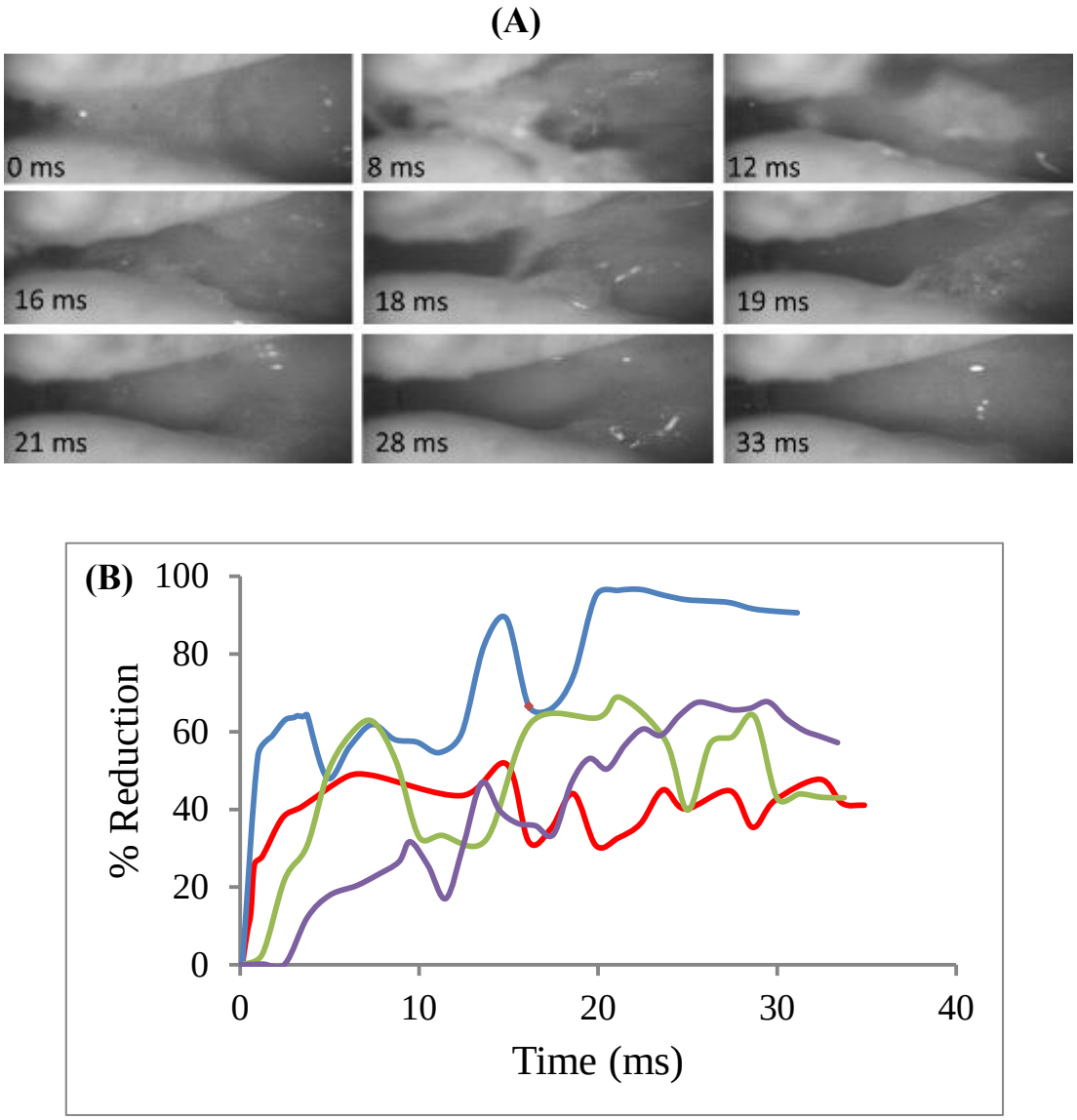

Figure 6.4 (A) High speed video frames showing the detachment of a *S. mutans* biofilm from the IP space between the two upper central incisors. The major part of the aggregate was removed within 20 ms, and almost all of it was removed within 33 ms. The images show the elongation of the biofilm before detachment. **(B)** Four curves from four different videos for the percentage reduction of the surface area coverage of the biofilm over time.

6.3.2. Analysis of the CLSM images and quantification of biofilm removal

Using confocal microscopy, *S. mutans* biofilms grown in the IP space showed bacterial cells aggregating together and forming complex cell cluster colonies consisting of 'tower', 'mushroom', and 'mound' shaped structures. The thickness of the

resulting biofilm on each tooth surface was approximately 200-300 μm. After the microburst, the images taken for the proximal surface of the teeth showed almost no biofilm close to the nozzle tip of the PT-*AirFloss*. Image analysis results showed 95 % removal close to the tip, 62 % removal at approximately half the labio-palatal distance from the tip to the back of the teeth, and 8 % removal at the back of the teeth (Figure 6.5). The percentage removal values were plotted versus the distance from the nozzle tip to midpoint of the palatal surface of the teeth. The resulting curve was compared to the values obtained from the numerical simulations for τ_w at the same locations.

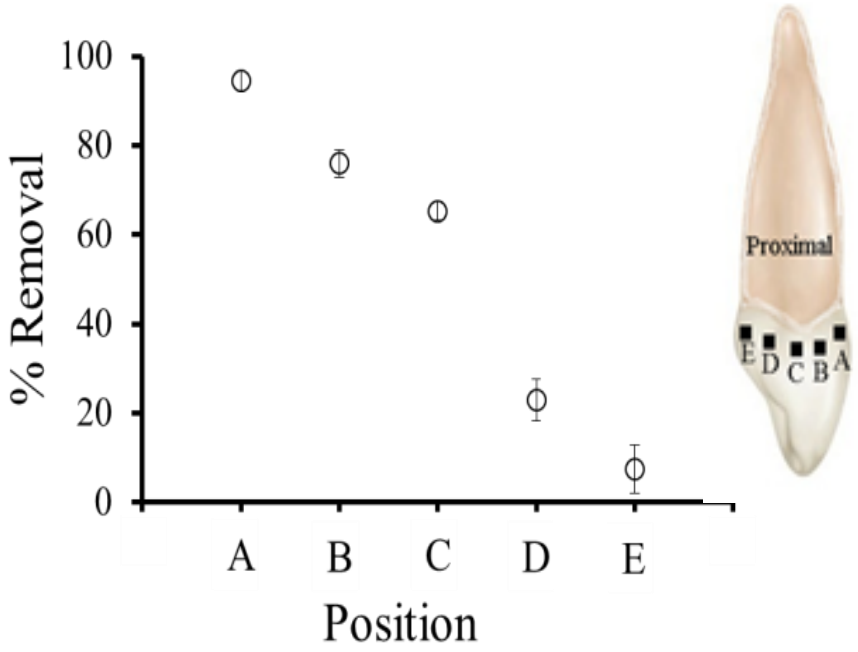

Figure 6.5 % Removal of the biofilm quantified from the CLSM images at different locations on the tooth surface in the IP space. The schematic drawing (right) shows the proximal view of the upper central typdont incisor. The black squares represent the different locations where the CLSM images were taken to quantify biofilm removal.

6.3.3. Numerical Simulations

Mesh Independence Study

A mesh independence study was performed, and an element size of 0.155 mm was selected for further numerical studies (results and graph shown in chapter 5)**.**

Quantification of τ_w distribution

A representative contour plot of the fluid τ_w spatial distribution on the tooth surface is shown in Figure 6.6a. This simulation corresponded to a velocity inlet of 60 m/s, with the circular nozzle tip located at z/H = 0.5, gingivo-incisally, where *z* (mm) is a spatial coordinate from the supra-gingival base of the tooth to the tip of the tooth perpendicular and *H* (mm) is the supra-gingival height of the tooth. Thus z/H = 0.5 equates to halfway up the tooth. The simulation showed the predicted fluid τ_w distribution on the proximal surface of the tooth starting from the labial side of the IP space close to the nozzle tip (2.7 kPa), to the midpoint of the palatal surface of the tooth (0.3 kPa).

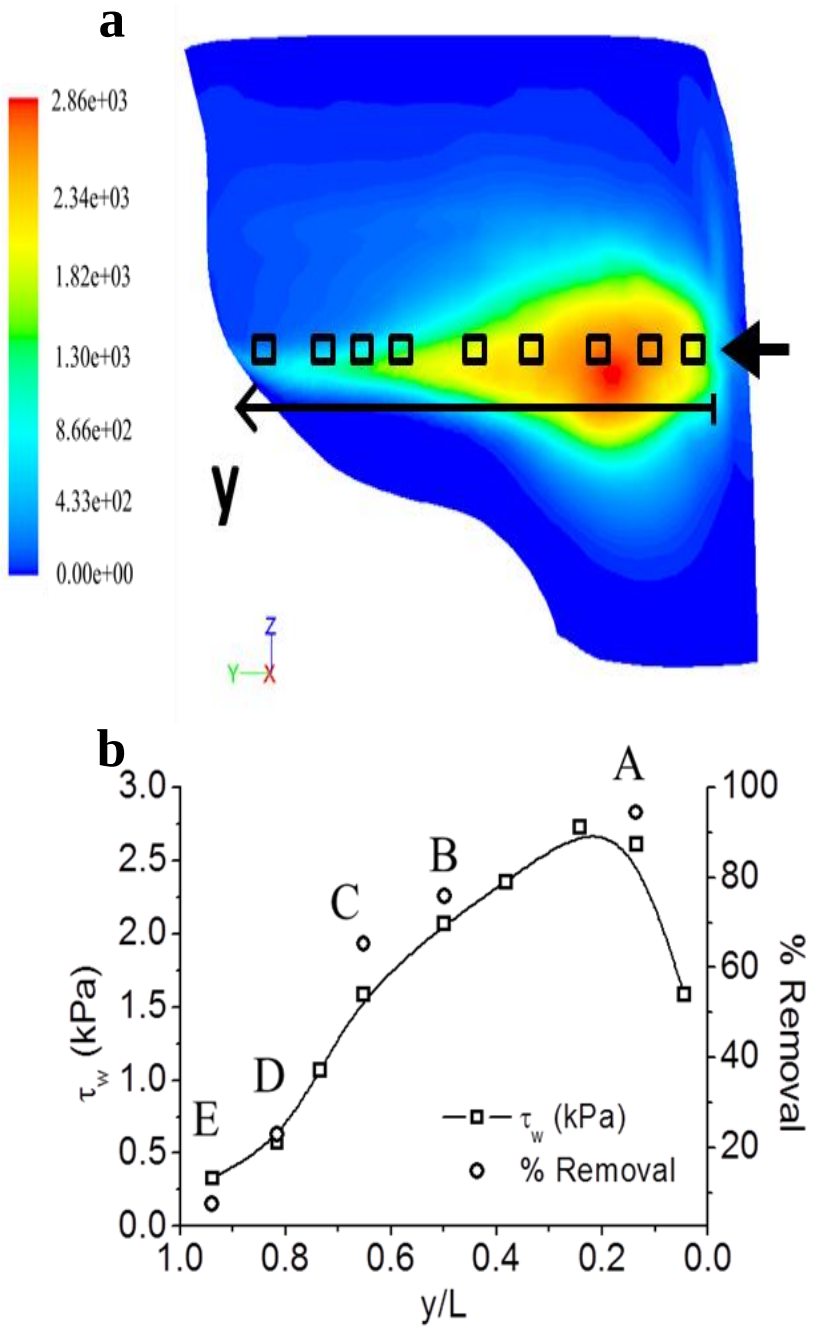

Figure 6.6 (a) Contour map showing the spatial distribution of the fluid shear stress on the tooth surface (colour distribution), as calculated from numerical simulations (circular nozzle tip; z/H = 0.5). **(b)** τ_w on the tooth surface (in kPa) at different y-positions along the tooth (i.e. from labial to palatal side), at a fixed z-position (gingivo-incisal), as also calculated from numerical simulations. Empty squares correspond to the measurement points (squares) in **(a)**. On the secondary y-axis, the percentage of biofilm removal measured experimentally in Figure 6.5 is plotted, with the 5 empty circles (denoted as A, B, C, D, and E) correspond to the same positions in the two figures.

6.3.4. Computational prediction of shear stress and experimental biofilm removal

The τ_w distribution obtained computationally was compared to experimentally measured removal of biofilms. A linear correlation of % removal as a function of τ_w (Figure 6.7) was found according to:

$$\text{Percent removal} = k\,\tau_w \quad (r^2 = 0.94) \qquad [1]$$

Where τ_w is wall shear stress (in Pa), and k (in Pa^{-1}) is the slope of the interpolating function.

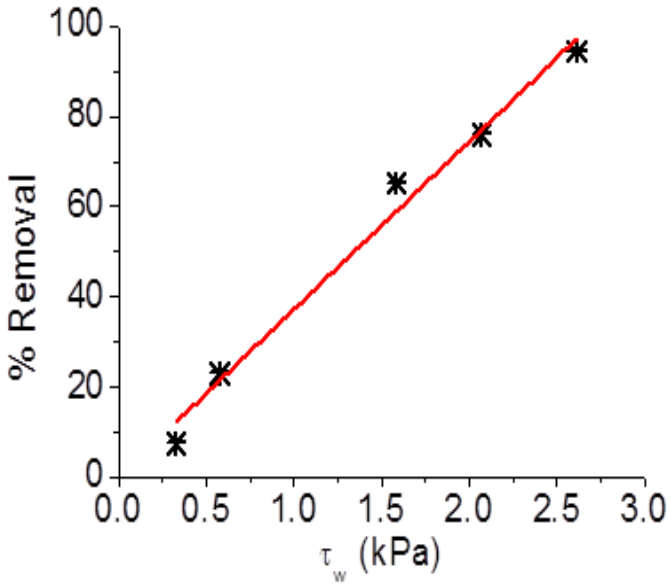

Figure 6.7 Relationship between biofilm percentage removal (determined experimentally) and τ_w on the tooth surface (determined computationally). Data points were interpolated with a linear trend (red line).

6.4. DISCUSSION

S. mutans biofilms were successfully grown on typodont teeth under static conditions. Using CLSM (Figure 6.2), the biofilms size and morphology shows resemblance to how they were described in literature [22] [143].

The high velocity water droplets released from the PT-*AirFloss* device are too fast to be seen by the naked eye. The flow motion of the droplets was captured using high speed videography which allowed us to generate novel footage showing the entire PT-*AirFloss* microburst mechanism (supplementary video 1). The fluid flow at the exit of the PT-*AirFloss* have been previously characterized by using the exit velocity of 60 m/s that was measured from the recorded high speed videos to calculate Reynolds number (Re), Weber number (We), and Ohnesorge number (Oh).

Videos of the detachment of the *DPBs* under high velocity water drops were also recorded (supplementary video 4). The device bursts a mixture of air and water, and the recorded videos demonstrated the presence of two phases: a) an initial continuous behaviour of the water flow of the burst (duration: 10ms) and b) the ejection of air bubbles causing the water droplets to split into nanodrops (duration: 35ms). In the presence of *DPBs* in the IP space, the burst water droplets impacted the biofilm causing an initial cohesive failure and subsequent adhesive failure as the shear caused the biofilm to flow over the tooth surfaces. In minimal time (< 15 ms), and using minimal water volume, more than 90 % of the biofilm was removed from the IP space. Confocal microscopy (Figure 6.2) showed that there was no biofilm close to the device tip, but small patches of biofilm remained on the prominences at the back of the teeth (palatal/lingual surface). The detached *DBPs* showed typical viscoelastic behaviour [17]. The *DPBs* were stretched under the impact of the fluid until they were totally detached and carried away with the fluid stream. In another experiment, the *DPBs* were subjected to the air-only burst from the PT-*AirFloss*, i.e. without putting any liquid in the device, and they deformed in the direction of the air flow

(supplementary video 2). When the burst ended, the *DPBs* returned partway to their original position, where they were still present and attached. We put forward the following mechanism for non-contact removal: (i) the energy from the device burst is absorbed by biofilm, resulting in the visco-elastic expansion of the biofilm; (ii) if the energy absorbed is sufficient and deformation is beyond the yield point, biofilm removal occurs [68] [77] [88] [130].

The removal process of *DPBs* by bursting high velocity water droplets from a pressure-driven droplet stream can be characterized by two phases. First, the stream impacts the *DPBs* causing the immediate detachment of the biofilm at the impact site while creating a hole. This is more commonly termed as cohesive failure. After that, the water droplets penetrate through the hole creating a shear stress on its neighbouring layers within the biofilm, while dragging them along its stream, causing them to elongate before breaking away from the tooth surface. This phase is known as the adhesive failure [147]. In this study, the droplets velocity was 60 m/s measured on exiting the device, and the generated fluid shear stress proved to be highly effective in removing attached biofilms. However, although the CLSM images confirmed our initial visual conclusion of the complete removal of biofilms close to the nozzle tip of the device, layers of biofilms remained on the back of the teeth, due to teeth architecture and the fluid flow behaviour in such regions. Experimental analyses showed that the amount of detached biofilm decreased away from the nozzle tip (Figure 6.5). This is explained by the reduction of τ_w on the surface of the teeth, as measured computationally. The weakening of shear forces is mainly due to the teeth geometry and the existence of curvature and undercuts which protects the bacteria from the effect of the burst.

The experimental data were compared to the results obtained from the 3D numerical simulations (Figure 6.6). The μ-CT scanner enabled the creation of 3D images for the typodont and for our region of interest: the IP space located between the two upper central incisors. The reconstructed 3D geometry of this IP space was used for the CFD simulations which predicted the shear stress distribution over the teeth surfaces: the highest shear being closer to the nozzle tip, while the lowest shear is located at posterior aspect of the teeth (Figure 6.6a). The 3D simulations for predicting τ_w were consistent with the obtained experimental results. *DPBs* survived the burst at areas of

low τ_w, while they were flushed away at areas where τ_w was higher. A direct linear relationship was deduced between the predicted fluid τ_w and the amount of detached biofilm obtained experimentally (Eqn. 1). This relationship could be used to predict the efficacy of oral healthcare devices which use shear forces, to remove *DPBs*. The values of *k* can be manipulated by exposing the biofilm to antibacterial agents (e.g. enzymes, chemicals, dentifrices) which target specific parts of the biofilm EPS causing its degradation. This ultimately leads to weakening of the biofilm and making it easier to detach at lower shear forces.

6.5. CONCLUSION

S. mutans biofilms were grown on typodont teeth. The detachment of *DPBs* from the IP space between the upper central incisors with high velocity water μ-drops was studied in the laboratory. An experimental setup was built and a methodology was developed to characterize, visualize, and quantify the efficacy of biofilm detachment by water droplets. The impact of the water drop was high enough to cause adhesive and cohesive viscoelastic failure contributing to the detachment process. High velocity water μ-drops can effectively remove and viscoelastic biofilms with minimal volume and time. This efficacy in detaching *DPBs* from the IP spaces, and thus preventing its chronic accumulation, automatically translates into prevention of dental caries formation in these sites.

The 3D numerical simulations predicted the shear stress value and spatial distribution over the teeth wall, and the results were in agreement with our experimental data. A linear relationship relating the computational value of τ_w exerted by the device on the teeth surface to the experimental detachment values obtained in the lab was established.

Chapter 7

7. Dispersal of *Streptococcus mutans* biofilms by matrix-degrading enzymes

7.1. INTRODUCTION

Bacteria in biofilms produce a matrix of extracellular polymeric substances (EPS) made up of carbohydrates, proteins, nucleic acids, and lipids/phospholipids [62] [21]. The EPS proportion in biofilms is generally estimated to constitute 50-90 % of the total organic matter [16] [101]. These microorganisms become embedded in this matrix which protects them and is responsible for their structure, coherence, physico-chemical properties and mechanical stability [148]. The cohesiveness of this three-dimensional, gel-like, highly hydrated EPS enables the biofilms to accumulate massively and contribute to the persistent infections that can develop in any site in the human body, including the oral cavity [115].

By studying the mechanical response of oral biofilms, better ways for removing or disrupting these bacterial communities are developed. Removal of oral biofilms by shear forces is one of the effective biofilm control strategies [62] [116]. Such strategies could be enhanced to become even more effective, by studying how the enzymatic treatments alter the mechanical response of biofilms and thus changing the response of the biofilm to the applied mechanical force. Hydrolytic enzymes have the potential to be used for the inhibition of the attachment on the tooth surface, or to degrade the already-formed dental plaque by hydrolysing its matrix [21]. As the application of shear forces might not be sufficient to stop the progression of dental plaque, thus it might be necessary to employ enzymatic plaque control as an adjunct.

A number of enzymes have been used to target specific molecules involved in the biofilm matrix [149]. The presence of DNaseI disrupts the biomass and further accumulation of *Streptococcus mutans* biofilms by targeting the extracellular DNA (or eDNA), which plays a role in adhesion and surface aggregation [150]. Here the effect of three different non-toxic and biodegradable enzymes was evaluated: DNase,

RNase, and Bromelain, a thiol protease extracted from pineapple stem, on early-stage biofilm formation and development by determining their effects on the biofilm matrix. We hypothesized that the disruption of the biofilm by these enzymes penetrating into the biofilm and degrading its matrix, or specific molecules in it, will potentially inhibit the early colonization events on the teeth. The three enzymes were applied on *S. mutans* biofilms and their individual effects on aggregation and bacterial viability were determined and compared. Also, different combinations of these enzymes were used, and their degrading effects on the biofilm matrix were studied. The inhibition activity of these enzymes on bacterial adhesion was also measured in terms of both the prevention of bacterial adhesion and of the detachment of already adhered bacteria.

An obstacle that faces the efficacy of any enzymatic therapy for disrupting oral biofilms is the relatively short residence time of the enzymes at the site of administration. To circumvent this problem, a film-forming adhesive copolymer was used, which offers a prolonged contact of the enzymes with the teeth and oral tissues. A biocompatible copolymer was used in conjunction with the matrix-degrading enzymes. The adhesive copolymer could potentially enhance the enzymes degradation activity by increasing their residence time in contact with the tooth surface allowing for a prolonged effect. Combining the adhesive copolymer with the enzymes would assist the degradation of the laboratory-grown *S. mutans* biofilms.

7.2. MATERIALS AND METHODS

7.2.1. Bacteria and growth media

Biofilms were grown from *Streptococcus mutans* UA159 (ATCC 700610). *S. mutans* is a facultative anaerobic, Gram-positive acidophilic bacterium, and an early colonizer of the tooth surface. *In vitro* biofilms grown from *S. mutans* are widely used to model an early stage cariogenic human dental plaque. Stock cultures of *S. mutans* were stored at -80^{o}C in 10 % glycerol in physiological buffered saline (PBS). Biofilms were cultured using sucrose supplemented brain heart infusion (BHI+S) medium (Sigma-Aldrich, The United Kingdom) and incubated at 37^{o}C, 5 % CO_2.

7.2.2. Enzymatic treatments

The three enzymes used in this study were supplied by different providers, and the enzymatic solutions were prepared according to their corresponding manufacturer's instructions. Bromelain (Sigma-Aldrich, UK) and was freshly prepared as 10 and 50 µg/ml solutions in phosphate-buffered saline (PBS). Ribonuclease A from bovine pancreas (Sigma-Aldrich, UK) and RNase-Free DNase I (Fisher Scientific, UK) were freshly prepared as 10 and 50µg/ml solutions in de-ionized water (Milli-pore, UK). The freshly prepared enzymes solutions were applied directly, and activation was achieved by incubation at 37^{o}C for 30 or 60 minutes.

7.2.3. Growth of biofilms in polystyrene microtiter plates

Clear 6-well, 24-well and 96-well plates (Nunclon^{TM} D Multidishes, Sigma Aldrich D7039, UK) were inoculated with autoclaved (BHI+S) media (200 µL aliquots in the 96-well, 1 ml aliquots in the 24-well, and 2 ml aliquots in the 6-well), before an overnight culture of *S. mutans* (10 µL in the 96-well, 50 µL in the 24-well, and 100 µL in the 6-well) was transferred. The biofilms were allowed to grow for 48h under shaking conditions (70 rpm), with the media changed once after 24h, before starting the enzymatic treatments. The wells were rinsed with three aliquots of either PBS or water. A blank with PBS (or water) as well as a control with bacterial suspension without enzymes were included in each row of the experimental plate. All the experiments were performed in duplicate. Fluorescence of the blank (without bacteria) and fluorescence of the control (biofilm without enzyme) were accounted for and included in the calculations to determine the fluorescence of the sample (biofilm with enzyme). For the 24-well plate experiments, the three enzymes were applied separately to the first 3 columns (4 wells each), the 4th and the 5th column were used as two different controls, and a combination of RNase and DNase was applied to the 6th column (Table 1). As for the 96-well plate experiments, the three enzymes were applied separately in three rows (6-10 wells each), then different combinations of the enzymes were used in four rows (6-10 wells each), and the remaining rows or columns were used for the different controls (Table 2).

7.2.4. Microplate reader

A procedure for counting bacterial cells over a fixed period of time must be used in order to determine different parameters of any bacterial population. The turbimetric method was used for our experiments, which allows a fast and accurate estimation of bacterial cells numbers in a liquid culture. Turbidity of a liquid culture is a measure of the amount of light scattered by the cells in suspension. An Omega plus microplate reader (BMG Labtech, UK) was used which measures the optical density OD of the liquid culture or the amount of light that is scattered by the cells in the liquid. It also detects the fluorescence intensity by exciting the sample at a specific wavelength causing it to emit light, and the emitted light is collected and separated from the excitation light by a filter, and the signal is measured using a light detector such as a photomultiplier tube (PMT). The microplate reader was used to study the degradation effect of the enzymes on the biofilm by measuring the OD and the fluorescence intensity of the liquid culture.

7.2.5. Live/Dead and Crystal Violet staining

Biofilms were stained with a LIVE/DEAD *Bac*Light Bacterial Viability kit (Invitrogen, UK). Briefly, after the rinses were performed the LD stain was prepared by dissolving 2 µL/ml of each (PI and SYTO9) in 10 ml PBS, and added to the wells for 20 minutes in the dark at room temperature. Fluorescence was measured using the plate reader. The excitation wavelength $\lambda_{excitation}$ used for SYTO9 (green) was 480 nm and the emission wavelength $\lambda_{emission}$ was 530 nm. The red fluorescent nucleic acid stain PI was excited at $\lambda_{excitation}$ of 488 nm, while its emission wavelength $\lambda_{emission}$ was 650 nm. An inverted fluorescence microscopy (AMG EVOS fl) was used to take images which were later on analysed for complementary quantification purposes (described in more detail in section 7.2.6.). Then, the biofilms were stained with 1 % Crystal Violet (CV) as follows: after rinsing the biofilms to remove all loosely attached bacteria, the plates were air dried for 45 minutes, then 1 % CV was added to each well of the plate for 20 minutes. Unbound CV was removed by aspiration and tap water was used to rinse the plate until no more CV was observed to dissolve in water. The plates were air dried and photographed. Then 95 % ethanol containing 2 % acetic acid (v/v) was added to each (to elute), and 100 µL from each well was transferred to a new 96-well plate and the optical density (OD) of CV was measured

at 590 nm by the plate reader, and the data was analysed using the MARS Data Analysis Software (Omega, BMG LABTECH, Offenburg, Germany) and Microsoft Excel.

	1	2	3	4	5	6
A	Bromelain	RNase	DNase	Control 1	Control 2	RNase + DNase
B	Bromelain	RNase	DNase	Control 1	Control 2	RNase + DNase
C	Bromelain	RNase	DNase	Control 1	Control 2	RNase + DNase
D	Bromelain	RNase	DNase	Control 1	Control 2	RNase + DNase

Table 7.1 Experimental design used for the biofilm degrading enzymes experiments in the 24-well plate (6 columns x 4 rows). Control 1 denotes biofilm only (no enzyme treatment), and control 2 (or blank) denotes PBS or water only (no biofilm and no enzymes).

	1	2	3	4	5	6	7	8	9	10	11	12
A	Sterile Media										Control 1	
B	Bromelain											
C	DNase											
D	RNase											
E	RNase and DNase											
F	Bromelain + (DNase and RNase)										Control 2	
G	DNase + RNase + Bromelain											
H	RNase + DNase + Bromelain										Control 3	

Table 7.2 Experimental design for the enzymes experiments in the 96-well plate (12 columns 1 to 12, and 8 rows from A to H). Sterile media was used in A to check for possible contamination during the experiment. For every treatment (rows B-H), wells in columns 1-10 were used. The last two columns (11 and 12) were used for the different controls in the experiment: biofilm only with no enzyme treatment (control 1), PBS or water only (control 2), and the stains solutions that were used (control 3).

7.2.6. Epi-fluorescence microscopy and image analysis

Image acquisition was performed on an inverted fluorescence microscopy (AMG EVOS fl). EVOS allows the simultaneous monitoring of PI and SYTO9 dyes. It also has the transmitted and DAPI modes. Three different objectives (40 ×, 20 ×, and 4 ×) were used. For the 40 × and 20 × objectives, 6-10 images were taken from different locations within each well. For the 4 × objective 5 images were taken for each well: one from the centre and 4 from different locations: left, right, bottom and top, and the

5 images were put together to form one final microscopic image that shows the entire well from side to side at this magnification and that was used for image analysis. The 5 images covered more than 80 % of the total surface area of the well. The remaining 20 %, which represents the four corners of the wells that were not captured by microscopic images, didn't show any biofilm because the pipetting was done in these corners of the wells. Biofilm surface coverage was calculated using ImageJ where the EVOS images were converted into a binary system (0 or 1) and biofilm-covered areas were quantified.

7.2.7. Enzymes for degrading biofilms on typodont teeth

S. mutans biofilms were grown on the tooth of a training typodont (Frasaco A-PZ periodontal dental model 4030025). The teeth were autoclave sterilized. The teeth were placed in either a 90 mm petri plate or a 15 mL Falcon tube, which was found to be more convenient. An inoculum was prepared in the Falcon tubes by adding 0.5 mL of *S. mutans* from the stock solution to 10 mL of sterile media (BHI+S). When using petri plates, 1 mL of the stock solution was poured over the teeth, and sterile media was added until the teeth were completely submerged. After a 48 hr incubation period and the media refreshed twice, the teeth were removed using sterile tweezers and were handled carefully to avoid any scratches. The teeth were submerged in freshly prepared 50 µg/ml solutions of the three enzymes in de-ionized water. After adding the enzymes and incubating at 37^{o}C for 30 or 60 minutes, images by the EVOS microscope were taken to study degradation.

7.2.8. Enzymes for the inhibition of bacterial adhesion

For the experiments involving the inhibition of bacterial adhesion, a pre-coating of a 24-well plate was done by placing 1 ml of 50 µg/ml of each of the three enzymes, both separately and collectively, in each well for 24 hours at 4^{o}C. The enzymes were then removed from the wells which were rinsed with either PBS or water for 5 minutes at room temperature. The coated wells were dried at 37^{o}C for 1 hr before the addition of the bacterial suspension (0.5 ml per well) and incubation for 24 h under shaking conditions (70 rpm). The controls were wells filled with PBS and water, and the number of rinses was accounted for. Microscopic images were taken by the EVOS microscope in transmitted mode.

7.2.9. Enzyme-adhesive copolymer mixture

A biocompatible copolymer of methylvinyl ether and maleic anhydride (Gantrez S 97 BF, from Ashland), with excellent mucosal adhesive properties and biocompatibility, was used in conjunction with the enzymes. The mixture was prepared from an original 4 % adhesive copolymer solution and 1 mg/ml enzyme stock solution. For example, to prepare the adhesive copolymer/Bromelain solution, 9 ml of the 4 % adhesive copolymer solution were added to 1 ml of the 1 mg/ml stock Bromelain solution, to obtain a final concentration of 100 µg/ml of the enzyme and 3.6 % of the adhesive copolymer in de-ionized water. To test the effect of the adhesive copolymer on the enzymes activity, three day old *S. mutans* biofilms on HA coupons were divided into 4 groups. Each of a PBS solution only, a 3.6 % adhesive copolymer solution, a 100 µg/ml enzymes solution, and the adhesive copolymer - enzyme solution were applied to one group, in a small petri dish. EVOS images were taken (10 for every plate), followed by image analysis. Also OD values for the enzymes versus time were measured by the plate reader after 5, 10, 15, 20, 30, 45 and 60 minutes.

To test the prolonged effect of the adhesive copolymer, all solutions were removed from the petri dishes, replaced with fresh media (BHI+S), and left for 24 hrs. EVOS images were taken after 12, 24, and 48 hrs, followed by image analysis.

7.2.10. Statistical analyses

Either the Student's t-test was used to determine whether the effects of the enzymes on degrading the biofilm were significant, and to compare the efficacy of the three different enzymes used (data were subjected to a Microsoft Excel macro), or One-way analysis of variance (ANOVA) was used, and Tukey's honestly significant difference (HSD) test with a confidence level of 95% was applied as a post-hoc test.

7.3. RESULTS

7.3.1. *Streptococcus mutans* biofilms

Viewed under an epifluorescence inverted microscope, the resulting biofilms were thick and confluent (B and C in Figure 7.1), or composed of dense microcolonies with

small, water-channel-like void areas (A and D in Figure 7.1) Viable bacteria were stained green, while dead bacteria were stained red. When the dead and live bacteria were close to each other or on top of each other, the red staining was mixed with green, which resulted in orange or yellowish colours (Figure 7.1).

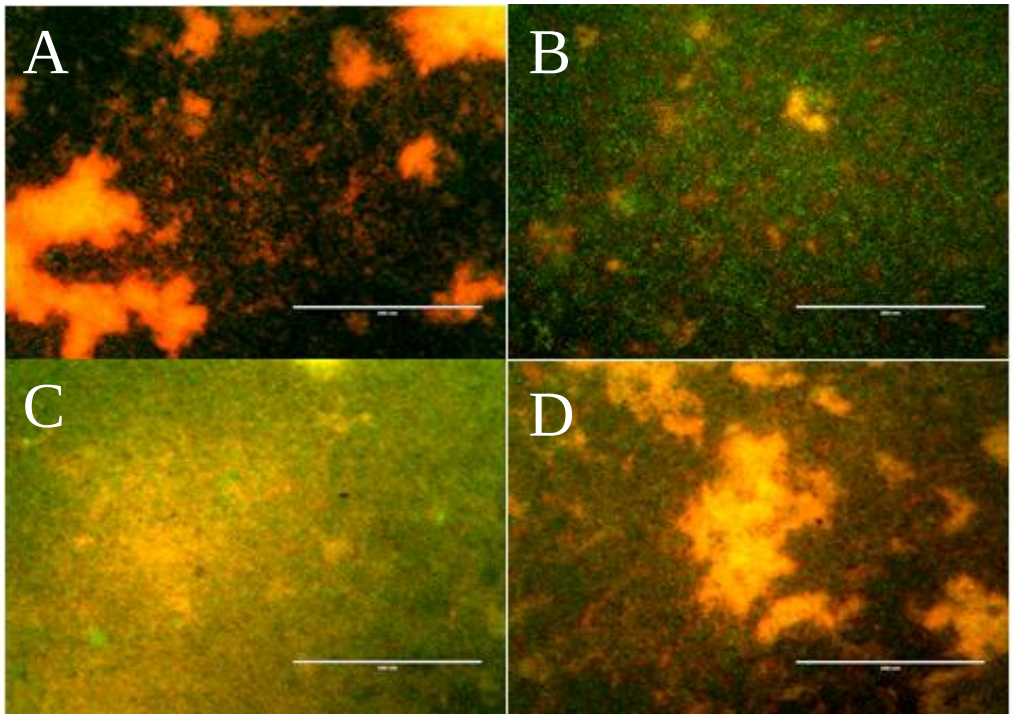

Figure 7.1 Live/Dead fluorescence images of *S. mutans* biofilms grown in plates. Four images (A, B, C and D) were from different wells that were used as control (biofilm only), and were later used as controls to compare with images taken for enzyme-treated biofilms. Scale bar = 200 µm.

7.3.2. Matrix-degrading enzymes

Enzymes in 24-well plates: biofilms were successfully grown in the 6 columns as was evidenced by microscopic images. The OD results (Figure 7.2) from the plate reader showed a decrease from the control to all the wells containing the enzymes, in both experimental runs. The fluorescence intensity from L/D (Figure 7.3) showed more live than dead bacteria in the control, but more dead than live bacteria in all of the enzymes wells. When comparing the control wells to the enzyme-treated wells there

was a decrease in the total number of bacteria, a decrease in the number of live, and a decrease in the number of dead. The OD for the Crystal Violet showed a decrease from the control to the enzymes, and more decrease in the case of the two enzymes combination (Figure 7.4).

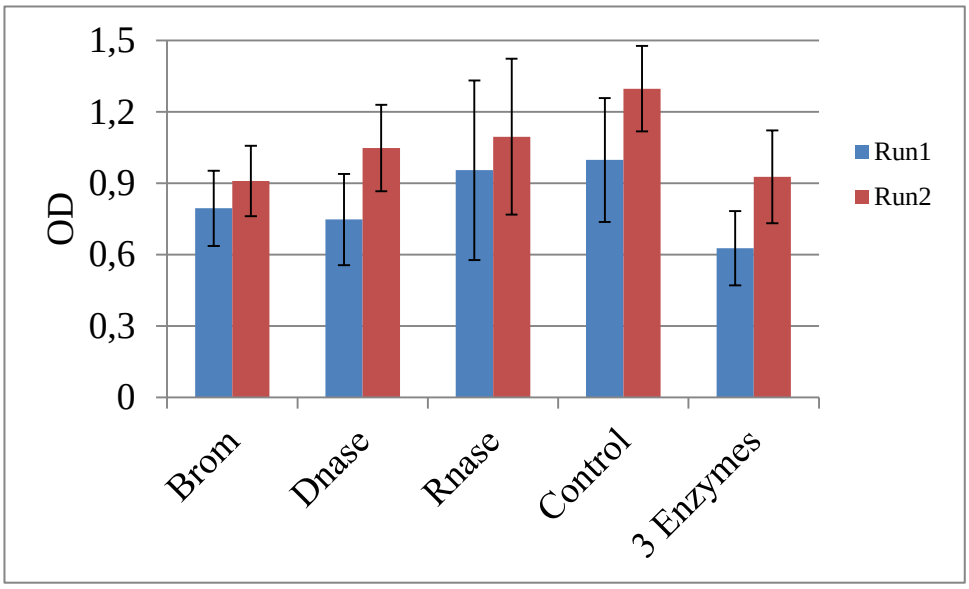

Figure 7.2 Preliminary data showing the final OD values for the three different enzymes, the control (biofilm only), and the combination of the three enzymes. The values represent two experimental runs (n = 4 in each). The bar graphs represent the average (± standard deviation in error bars). The two enzymes were sequentially added to the biofilm and incubated with 1 hour in between and two rinses with PBS or water after each enzyme application. All the 6 treatments had the same number of rinses.

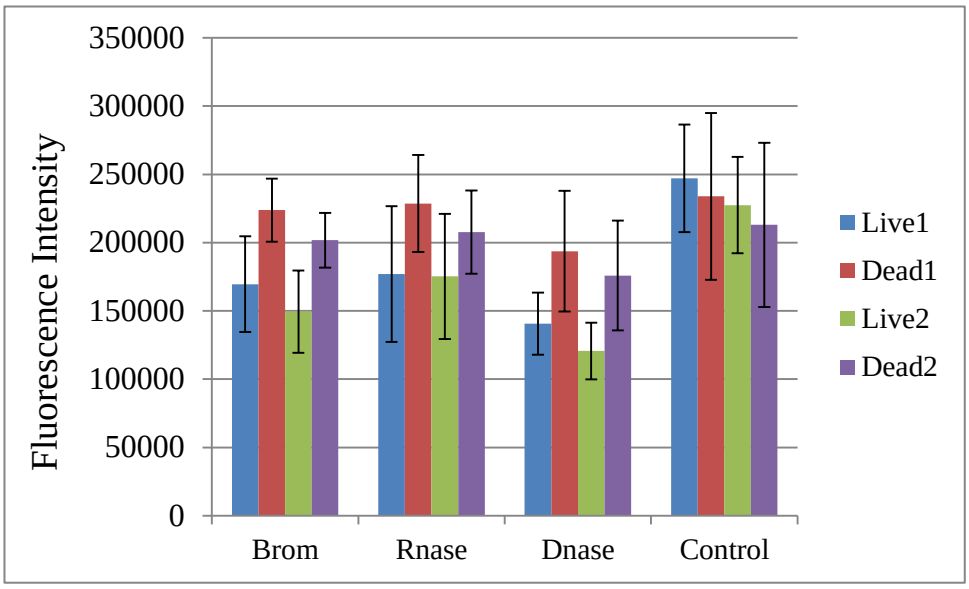

Figure 7.3 Preliminary data showing the fluorescence intensity values (L/D) for the three different enzymes, and the control (biofilm only), for two independent experiments (n = 4 in each). The bar graphs represent the average (± standard deviation in error bars). The three enzymes and the control had the same number of rinses with PBS or water.

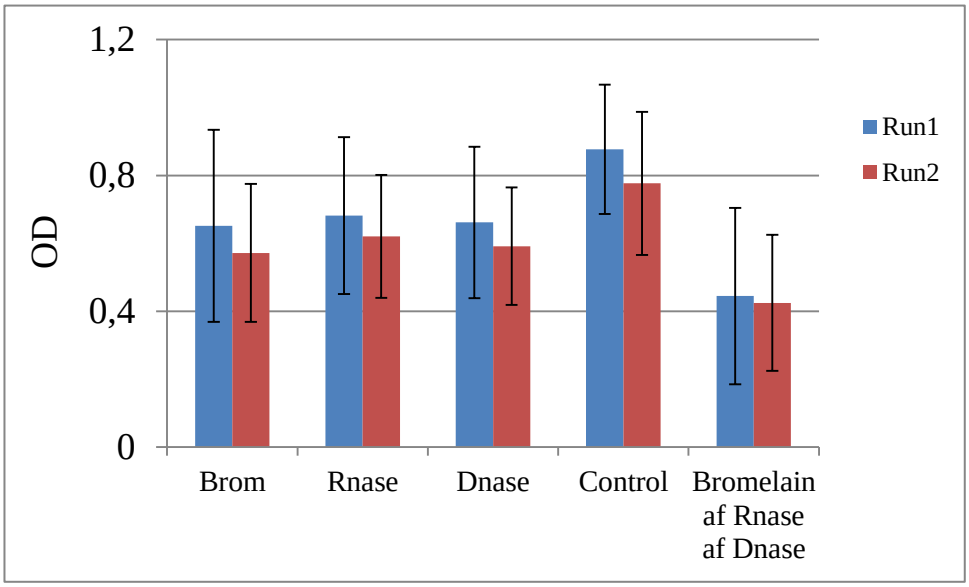

Figure 7.4 Preliminary data showing the final OD values (for Crystal Violet staining) for the three different enzymes, the control (biofilm only), and the combination of 3 enzymes. The values are for two independent experiments (n = 4 in each experiment). The error bars represent the standard deviation from the mean.

Enzymes in 96-well plates: biofilms were successfully grown in the wells as was evidenced by microscopic images. Using the plate reader, the fluorescence intensity from L/D (Figure 7.5) showed more live than dead bacteria in the control, but more dead than live bacteria for each of the individual enzyme treatment. When comparing the control wells to the enzyme-treated wells there was a decrease in the total number of bacteria, a decrease in the number of live, and a decrease in the number of dead. The results for the three different combinations of enzymes that were used: 1) Brom + (DNase and RNase), 2) DNase + RNase + Bromelain, 3) RNase + DNase + Bromelain generally showed increase in the number of bacteria compared to the single-enzyme treatments. The OD values for two biofilms (24 h and 48 h) that were stained with Crystal Violet are plotted in Figure 7.6. The results showed a decrease from the control to the enzymes for both the 24 h and the 48 h biofilms.

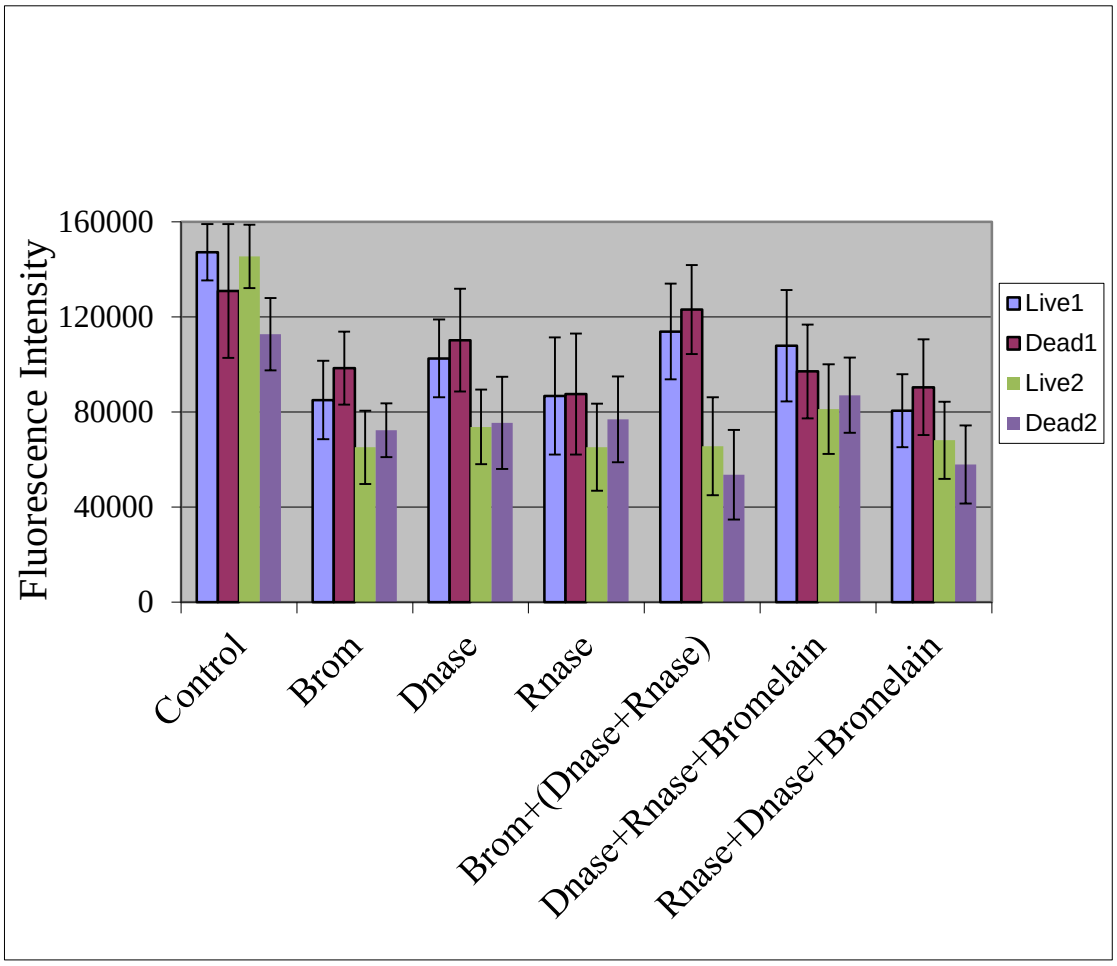

Figure 7.5 Preliminary data showing the fluorescence intensity values (L/D) for the three different enzymes, the three different combinations of the enzymes, and the control (biofilm only). The data are for two independent experiments (n = 5-11 in each experiment). Live1/Dead1 represents the data for the first run, while Live2/Dead2 represents the data for the second run. The error bars represent the standard deviation from the mean. The number of rinses was accounted for. The enzymes are applied following the sequence shown in the graph (e.g. DNase + Rnase + Bromelain means that DNase was applied first, followed by Rnase, and then Bromelain).

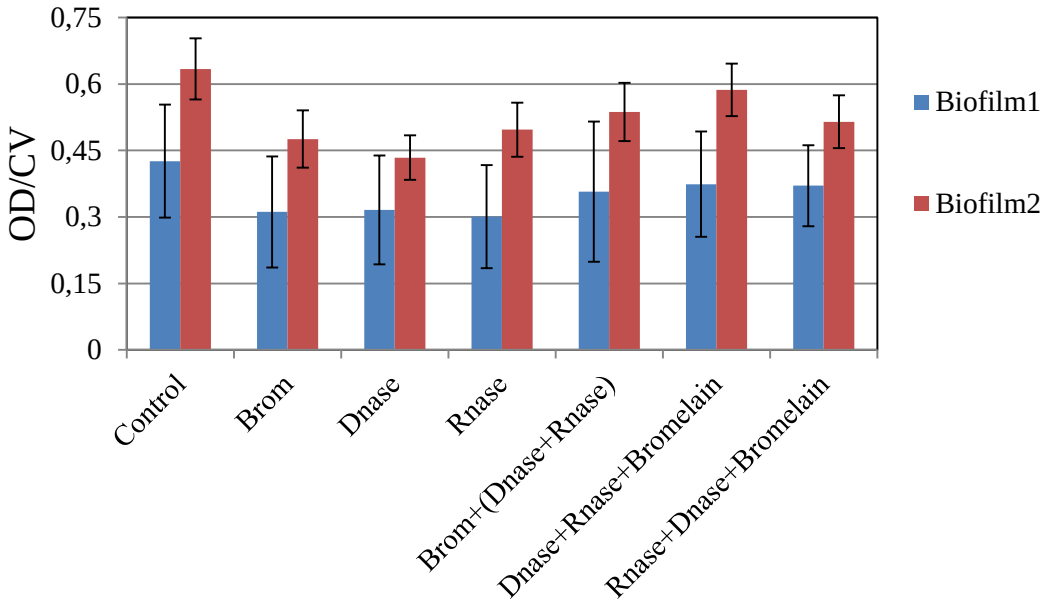

Figure 7.6 Preliminary data showing the final OD values for two biofilms (24 h and 48 h) stained with Crystal Violet (n = 5-11). The error bars represent the standard deviation from the mean. The plot includes the values for the treatments with the three different enzymes, the three combinations of the enzymes, and the control (biofilm only). The OD values for the 48 hr. biofilm (red) are overall higher than those for the 24 hr. biofilm (blue). However, the effect of the enzymes is comparable and follows similar trend for both biofilms.

Enzymes on typodont teeth: biofilms were successfully grown on the model teeth, as evidenced by microscopic images (Figure 7.7). The plastic model teeth do not transmit light, so it was not possible to see the bacterial biofilms. However, by fixing the teeth in place using lock-in tweezers, and looking from the side, we were able to distinguish the biofilm from the tooth surface and measure the thickness of the biofilm before and after the enzymatic treatments. The thickness ranges went down from 150-300 µm (before) to 10-50 µm (after).

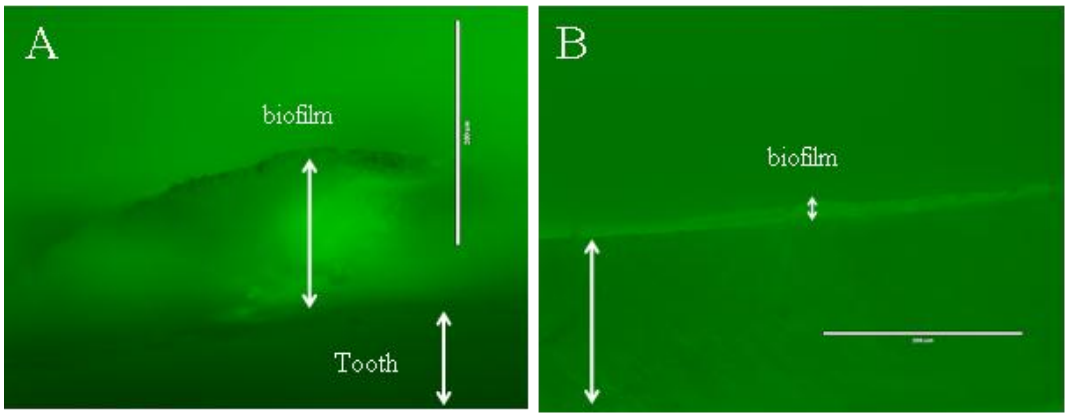

Figure 7.7 Microscopic images showing a *S. mutans* biofilm on a typodont tooth A) before and B) after enzymatic treatment with Bromelain. The image was taken by EVOS microscope with the 20 × objective. The vertical (A) and horizontal (B) scale bars = 200 µm.

7.3.3. Image analysis

The microscopic images produced by EVOS were analysed. Image processing and analysis by the NIH software ImageJ (http://rsb.info.nih.gov/ij/) allowed the quantification of biofilm percentage surface coverage area, by measuring the total area of bacteria (both green and red fluorescence). Because two sets of images were obtained using different microscopic objectives of 20 × and 4 ×, two image analysis methods were used. For the images taken by the 20 × objective (Figure 7.8), 6-10 images were recorded for each well in the 96-well plate and analysed. For the images taken by the 4 × objective (Figure 7.9), the analysis was explained earlier in a previous chapter (materials and methods). The results from the two methods were averaged and the results are presented in Figure 7.10.

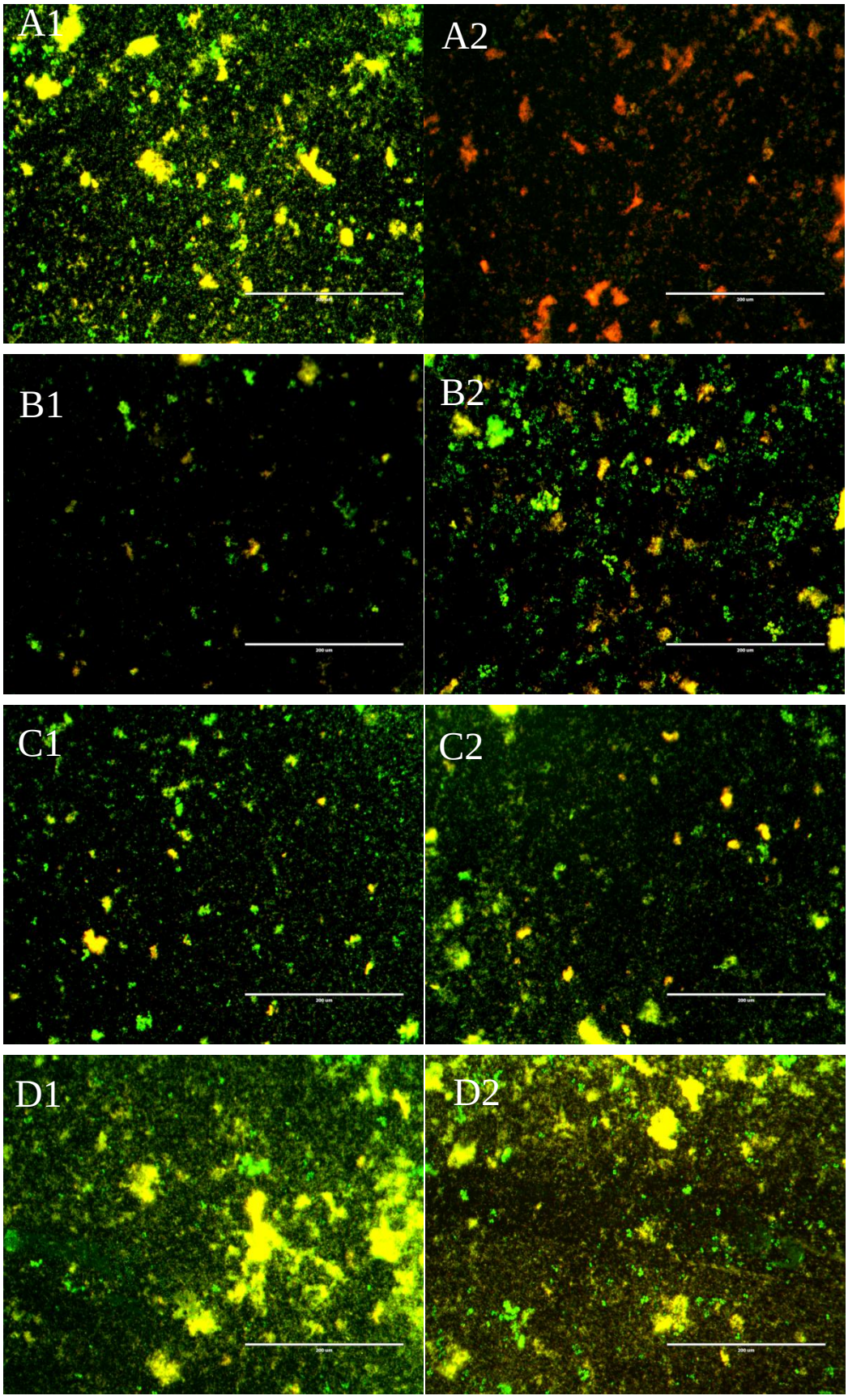
A1
A2
B1
B2
C1
C2
D1
D2

Figure 7.8 Live/Dead fluorescence images of *S. mutans* biofilms grown in wells treated with different enzymes. A) DNase B) Bromelain C) RNase D) Combination of the enzymes Bromelain + (RNase and DNase). Two images for each treatment are shown here to demonstrate the heterogeneity of biofilms even when grown under the same conditions. The images were compared to the control images in Figure 7.1. Scale bar = 200 µm.

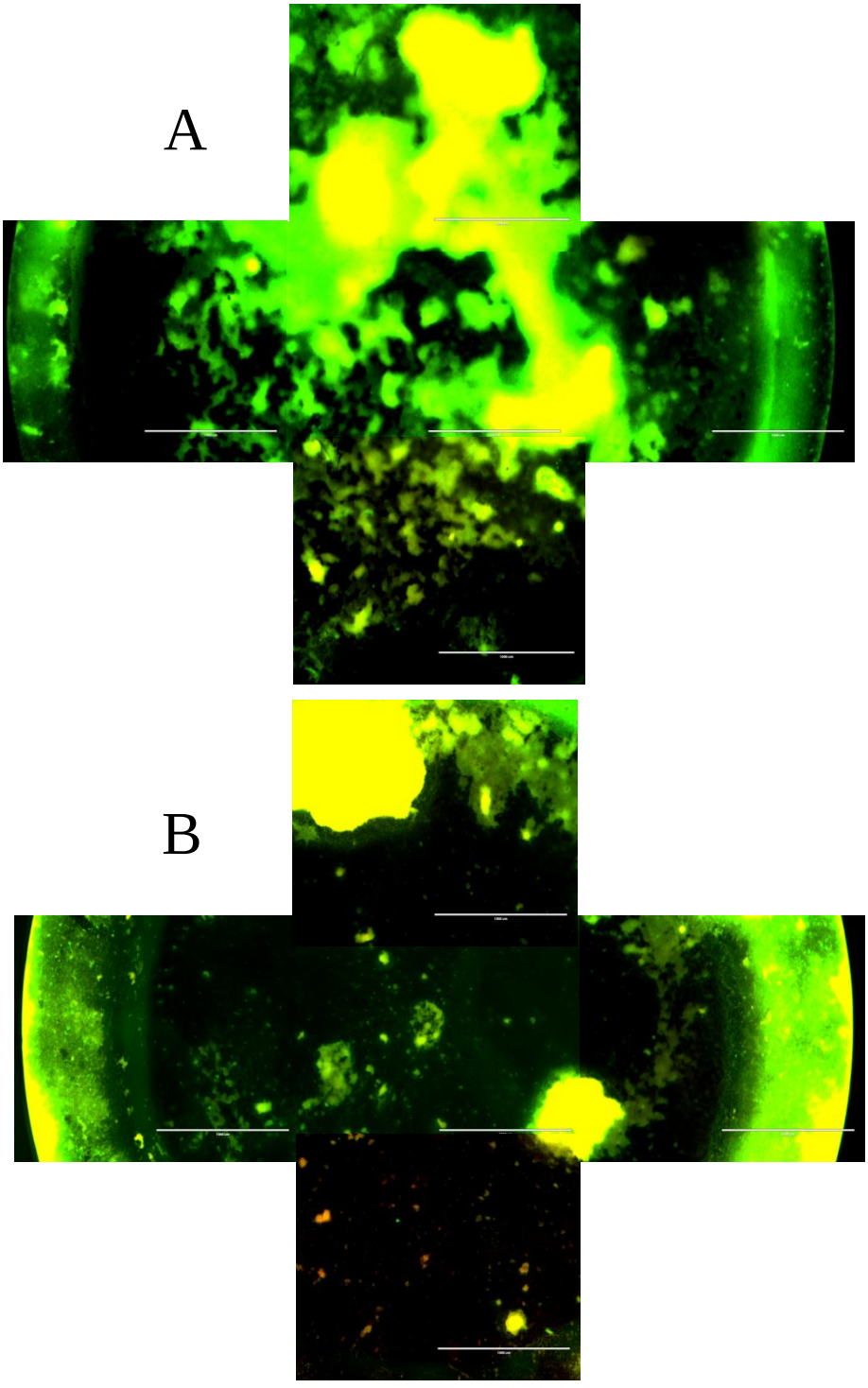

Figure 7.9 Low power microscopic images showing: the control (A), and the Bromelain-treated (B) wells. Each image is made of 5 images that were taken from the: centre, left, right, bottom and top sides of the well and put together. Scale bar = 1000 µm.

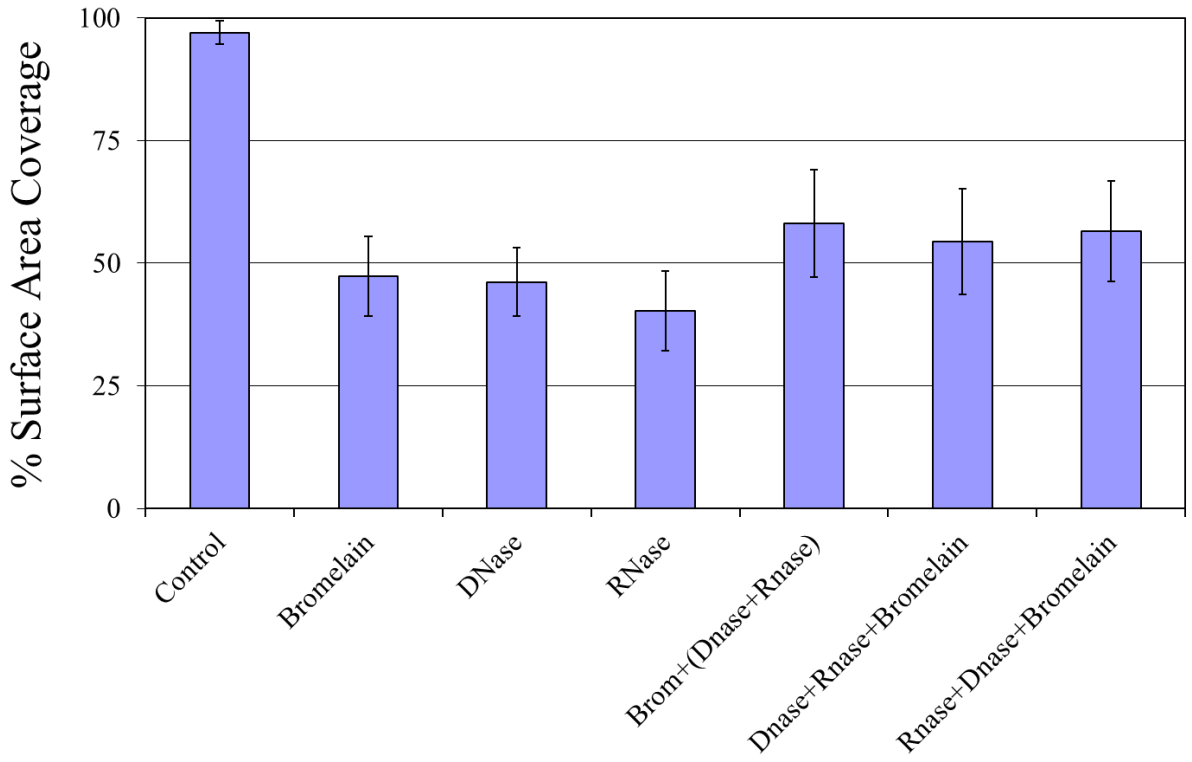

Figure 7.10 Preliminary data showing the percentage of surface area coverage of the biofilm in the 96-well plates. The values were obtained from the analysis of the EVOS microscopic images, and they represent an average of two image analysis methods (n = 7 in each).

7.3.4. Enzymes for the inhibition of bacterial adhesion

The preliminary results showed that pre-coating the wells with the different enzymes neither prevented biofilm formation nor minimized its growth, as was evidenced by the microscopic images. All the images taken for the control (biofilm only) and the enzyme-treated wells were similar and showed the same amount of biofilm (Figure 7.11).

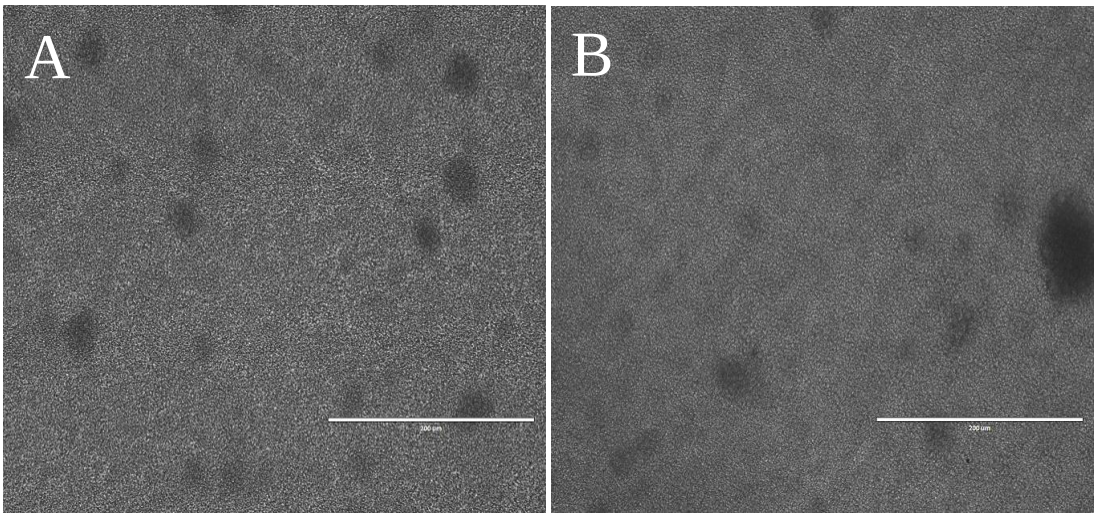

Figure 7.11 Transmitted light microscopic images of *S. mutans* biofilms grown in 24-well plates. Image A was taken for a biofilm grown in a well that was pre-coated with DNase enzyme, while image B was taken for the control well (no enzymatic coating, only biofilm). Both images showed complete biofilm coverage. Scale bar = 200 μm.

7.3.5. The effect of the enzymes-adhesive copolymer combination

Figure 7.12 Shows the effect, over time, of one of the enzymes (Bromelain) used in the experiments on degrading the biofilm. The more time the enzyme was given to react, the more amount of the biofilm was degraded.

The addition of adhesive copolymer to the enzymes did not negate the effect that the latter had on degrading the biofilm. Figure 7.13 demonstrates that the action of the enzyme (Bromelain) was not changed when the adhesive copolymer was combined with the enzymatic solution treatment of the biofilm.

Furthermore, the addition of the adhesive copolymer maintained the effect of the enzyme for prolonged periods of time, when compared to the use of enzyme alone without the adhesive copolymer (Figure 7.14).

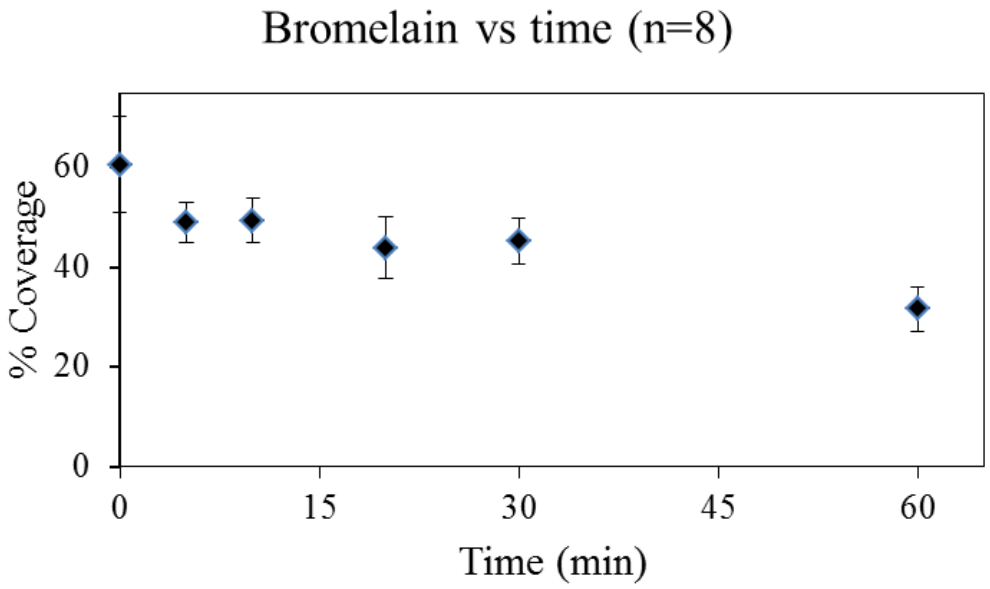

Figure 7.12 Preliminary data showing the biofilm surface coverage versus time after addition of the protease Bromelain. The biofilm was grown on a hydroxyapatite disc.

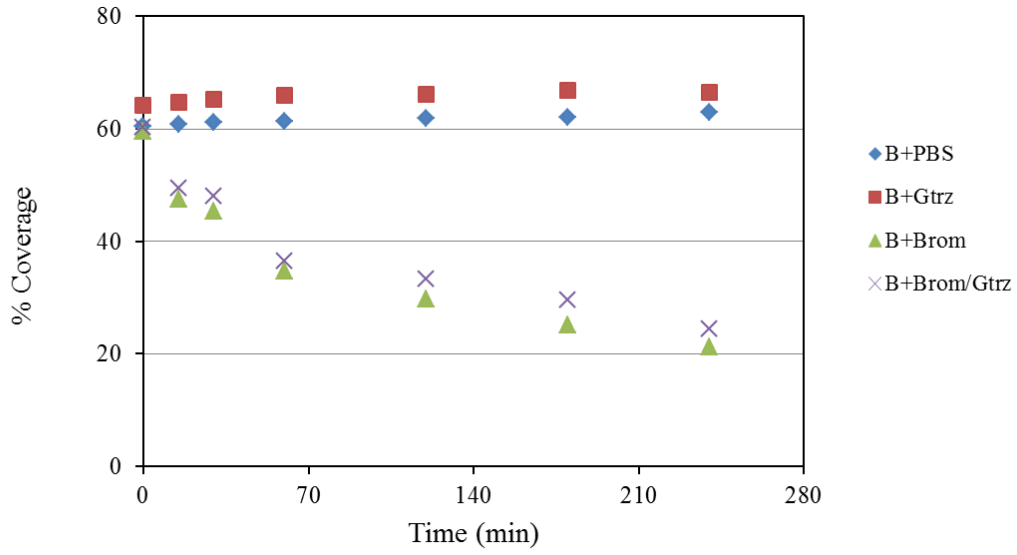

Figure 7.13 Preliminary data showing the biofilm surface coverage versus time, showing the degrading effect of an enzyme (Bromelain) on the biofilm, both alone and in the presence of the adhesive copolymer, where: B+PBS (biofilm+PBS = control 1)**,** B+Gtrz (biofilm+Gantrez = control 2)**,** B+Brom (biofilm+Bromelain)**,** B+Brom/Gantrez (biofilm+Bromelain/Gantrez mixture).

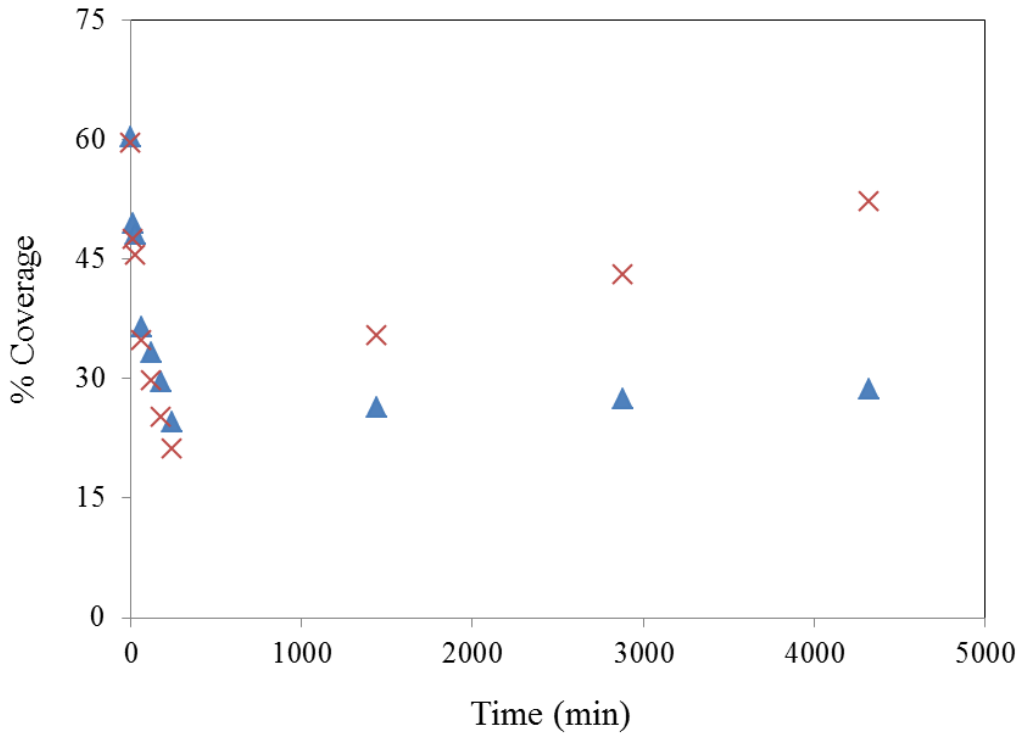

Figure 7.14 Preliminary data showing the biofilm surface coverage versus time, showing that the adhesive copolymer maintaining the effect of the enzyme for prolonged periods of time (triangles) when compared to the use of enzyme alone without the adhesive copolymer (crosses X).

7.4. DISCUSSION

S. mutans biofilms were successfully grown in the 6, 24 and 96-well plates and on the typodont teeth as evident by microscopic images. Three biofilm matrix-degrading enzymes were used in this study. Each enzyme targets a specific molecule in the EPS [151] [115] [152]. The effect of each enzyme was studied separately, and then the different combinations of these enzymes were studied in the aim to find out the most efficient mixture in terms of degrading the biofilm matrix. All 3 enzymes used, whether used separately or in combinations, proved their ability to degrade a part of the matrix, as demonstrated by the optical density and fluorescence measurements by the microplate reader, and by the image analysis results. The results obtained in the 96-well plates were different than the results obtained in the 24-well plates. Even

when the experiment was repeated in the same plate (24 or 96), the results varied each time. The different trends of removal observed were attributed to the wide heterogeneity associated with the biofilm matrix [20], even in the case of a mono-species biofilm, or when the experiment was repeated under the exact same conditions. The matrix is a dynamic environment composed of microbial cells, polysaccharides, proteins, carbohydrates, nucleic acids, and water, together with excreted cellular products [21]. Numerous microenvironments exist within this great heterogeneity, and wide variability is always expected when studying these biofilms.

The total number of bacteria decreased from the control to the enzyme-treated wells. The control showed more live than dead, while the treated ones generally showed more dead than live. This could be explained by the fact that the degradation of specific molecules in the matrix by these enzymes might have caused the death of a number of the bacteria. The results from the enzymes combinations showed an increase in the number of bacteria over the individual enzymes, mainly because the addition of more enzymes was done by incubation for 1-2 additional hours which allowed the continuation of growth of the biofilm. Here, the biofilm growth rate overcame the degradation effect of the enzyme. The combinations of enzymes used did not demonstrate a better degradation effect in comparison with their individual enzymes, hence the necessity to try different combinations in future work. When choosing the combinations, Bromelain was deliberately left out (or last) because it degrades all proteases, while DNase or RNase were applied first.

For the inhibition of adhesion experiments, the pre-coating of the wells by the enzymes did not prevent *S. mutans* biofilm formation or affect its accumulation. It was expected that biofilm releasing enzymes could exhibit broad-spectrum activity [152], which was not the case.

A film-forming adhesive copolymer was used, with excellent mucosal adhesive properties and biocompatibility, was used in conjunction with the enzymes. The adhesive copolymer enhanced the enzymes degradation activity by seemingly increasing their residence time in contact with the tooth surface allowing for a prolonged effect. Combining the adhesive copolymer with the enzymes allowed better degradation of the laboratory-grown *S. mutans* biofilms as estimated from image analysis.

7.5. CONCLUSION

S. mutans biofilms were successfully grown inside microtiter plates and on model teeth. The microplate reader proved to be very useful in our study, giving us an excellent tool to investigate the effect of enzymatic treatments on the growth of biofilms. The enzymes used were all capable, to varying degrees, of degrading parts of the biofilm matrix. The combinations of enzymes used improved the degradation effect; however, more investigation is needed. The stains used (Live/Dead and Crystal Violet) allowed the visualization of the biofilm and provided valuable information that was used for further analysis. Pre-coating the plates with the enzymes did not inhibit biofilm formation. Combining the enzymes with an adhesive copolymer might increase their effect by potentially increasing their residence time in contact with the oral and dental tissues. All the data presented in this chapter is considered preliminary since most the experiments were done only twice. More investigation has to be done in future studies to prove the results obtained here.

Chapter 8

8. General conclusions

Although a set of comprehensive conclusions were provided at the end of each chapter, this section intends to draw together the key findings in order to establish a general overview of the experimental discussion and outline future directions.

Calcium cross-linked dextran gel, which could be used as a surrogate to replace real dental plaque biofilms for rapid screening and for use in non-microbiological research settings, was developed. The mechanical properties of the gel, as well as the viscoelastic *S. mutans* biofilms, were studied using uni-axial compression.

A model system to investigate the cleaning of dental biofilms using high velocity water drops was developed. High speed imaging was used to elucidate and quantify the cleaning mechanisms. High resolution end point data for assessing efficacy of the cleaning process was obtained by designing the experimental model to be compatible with confocal microscopy.

The detachment of biofilms with high velocity water μ-drops delivered by an interdental cleaning device prototype was investigated in the laboratory using both the surrogate gel and the *S. mutans* biofilms. An experimental setup was built and a methodology was developed to characterize and visualize the μ-burst. The impact pressure of the water drop was high enough to cause sequential cohesive and adhesive viscoelastic failure contributing to the detachment process. This efficacy in detaching *DPBs* from the IP spaces, and thus preventing its chronic accumulation, automatically translates into prevention of dental caries formation in these sites.

The utilization of μ-CT to image the typodont in 3D was significant and allowed the construction of a model of the IP space that was used in subsequent CFD modelling, which was utilized to calculate the shear stress distribution, caused by water drops generated from an oral hygiene device, on the tooth surface. ANSYS Fluent, the widely-used and well validated software, was used for that purpose. To the best of our knowledge, this is the first time that CFD has been used to calculate the wall shear

stress distribution, caused by water drops generated from an oral hygiene device, on the tooth surface.

The 3D numerical simulations predicted the shear stress value and spatial distribution over the teeth wall, and the results were in agreement with our experimental data. A direct numerical relationship, relating the computational value of τ_w exerted by the device on the teeth surface to the experimental biofilm detachment values obtained from laboratory experiments for the percentage removal of biofilms, was established. Changing the shape and location of the nozzle tip with respect to the IP space significantly changed the outcome of the device burst.

The microplate reader proved to be very useful in our study, giving us an excellent tool to investigate the effect of enzymatic treatments on the growth of biofilms. *S. mutans* biofilms were successfully grown inside microtiter plates. The preliminary data showed that the enzymes used were all capable of degrading parts of the biofilm matrix. The combinations of enzymes used did not improve the degradation effect, hence more investigation is needed. The stains used allowed the visualization of the biofilm and provided valuable information that was used for further analysis. Pre-coating the plates with the enzymes did not inhibit biofilm formation. Combining the enzymes with an adhesive copolymer seemingly enhanced their effect by potentially increasing their residence time in contact with the oral and dental tissues.

Chapter 9

9. Future directions

9.1. Mechanics and disruption of dental biofilms

Future work will focus on measuring the mechanical properties of *S. mutans* biofilms, which were subjected to different enzymatic and chemical treatments, using compression, tension and shear testing. An ideal system would be able to perform the three tests because during mechanical removal of oral biofilms, a combination of compression, shear and tensile forces is applied to a biofilm. To our best knowledge, no such system exists at the moment. These three different kinds of tests will complement each other and will enable us to extract all the necessary mechanical parameters required to know the exact biofilm behaviour and response to forces exerted on it. Such data will be the cornerstone to develop strategies aiming towards removal and disruption of dentals biofilms.

Future work will include measuring various biofilm mechanical and viscoelastic parameters at different conditions (pH, time, temperature, etc.) and varying concentrations of different ions (e.g. Na^{+}, F^{-}, Ca^{2+}, $Al^{3+)}$ as well as in response to the ionic chelators (e.g. EDTA, GDTA), since EPS cross-linking significantly affects cohesiveness of the biofilm. These chelants form soluble, complex molecules with certain metal ions in the biofilm, inactivating the ions so that they cannot normally react with other elements or ions to produce precipitates. Chlorhexidine CHX (disinfectant), Xylitol, $AlCl_3$, dentifrices, and antimicrobials are other agents that will be used and tested on the biofilms.

In addition, biofilms treated with the enzymes mentioned in Chapter 7 will be mechanically characterized to assess the effect that these matrix-degrading enzymes have on biofilms. Assessing viscoelasticity will be monitored before, during and after exposure to various combinations of the mentioned ions or chelators. Biofilms will be treated with all the previously mentioned agents and their mechanical parameters will be extracted and compared to untreated biofilms.

Our future work will also focus on coming up with different enzymatic combinations to achieve higher degradation effects on the biofilms. The enzymes will also be used with other antimicrobial agents, such as chlorhexidine, to enhance the degradation of the biofilm matrix and hence total biofilm detachment. Also, mechanical testing will be conducted in conjunct with the enzymatic treatments to study the effect of these enzymes on the mechanical properties of the biofilms. All the experiments will be repeated with dental plaque biofilms or *S. mutans* biofilms grown on human teeth.

9.2. Simulations and computational studies

Computational fluid dynamics simulations

After studying and numerically approximating the mechanical parameters of the *S. mutans* biofilms, the corresponding values will be incorporated into the CFD work and simulations will be performed to obtain the most accurate representation of biofilm mechanics and behaviour under various conditions.

The mechanical properties of biofilms (i.e. failure and viscoelastic properties) that were studied using uniaxial compression will be incorporated into the simulation in the aim of getting the most realistic data regarding the behaviour, disruption or detachment of dental biofilms. Also, different particles (and enzymes) will be incorporated into the flow (i.e. added to water used in the devices). Their behaviour and velocities will be monitored in the aim of studying the biofilm behaviour and mechanics.

The relationship between computational simulations and experimental work that was mentioned in Chapter 6 will be explored further. Our aim will be to maximize the biofilm removal percentage at the lowest possible shear stress. This could be achieved by introducing various treatments to the biofilms, such an enzymes and chemicals. Such treatments could weaken the EPS cohesiveness and the biofilm's attachment to the surface making it easier to detach using fluid flow forces.

Once we achieve the goal of using the 3D simulation to study the effect of fluid flow on the biofilm and use in vitro biofilm research to improve this modelling, this 3D model will be applied to study the disruption of biofilms in areas other than the IP space, such the surfaces of root canals (endodontic pathology), roots (periodontal pathology) and dental implants (peri-implantitis) where the biofilms cause inflammatory reaction of the host. Coming up with such a simulation is very important because in the dental field the dimensions are very small, it is difficult to create reliable in vitro biofilm models to study the removal of the biofilm.

REFERENCES

[1] R. M. Donlan and J. W. Costerton, “Biofilms: Survival Mechanisms of Clinically Relevant Microorganisms,” *Clinical Microbiology Reviews* , vol. 15 , no. 2 , pp. 167–193, Apr. 2002.

[2] H. P. Blaschek, H. H. Wang, and M. E. Agle, *Biofilms in the food environment*. Willey-Blackwell, Ames, Oxford, Carlton, 2007.

[3] T. Bjarnsholt, P. Jensen, C. Moser, and N. Høiby, *Human Oral Bacterial Biofilms: Composition, Dynamics, and Pathogenesis, in Biofilm Infections*. Springer New York, 2011, pp. 35–68.

[4] DHH services, “Oral Health in America: A report of the Surgeon General.,” 2000.

[5] P. E. Peterson, “Continuous improvement of oral health in the 21st century - the approach of the WHO Global Oral Health Programme. The World Oral Health Report,” 2003.

[6] A. Savage, K. A. Eaton, D. R. Moles, and I. Needleman, “A systematic review of definitions of periodontitis and methods that have been used to identify this disease.,” *Journal of Clinical Periodontology*, vol. 36, no. 6, p. 458, 2009.

[7] D. M. Bamberger, “Diagnosis and treatment of osteomyelitis. Compr Ther.,” *Compr Ther. Summer*, vol. 26, no. 2, pp. 89–95, 2000.

[8] C. L. Frere, “Review of: Color Atlas of Dental Hygiene: Periodontology,” *Journal of Dental Hygiene*, vol. 81, no. 3, p. 59.

[9] I. Kleinberg, “A Mixed-bacteria Ecological Approach to Understanding the Role of the Oral Bacteria in Dental Caries Causation: an Alternative to Streptococcus mutans and the Specific-plaque Hypothesis,” *Critical Reviews in Oral Biology & Medicine* , vol. 13 , no. 2 , pp. 108–125, Mar. 2002.

[10] J. M. Hardie, “The microbiology of dental caries.,” *Dent Update*, vol. 9, no. 4, pp. 199–200, 202–4, 206–8., 1982.

[11] J. M. Hardie, “Oral microbiology: current concepts in the microbiology of dental caries and periodontal disease.,” *Br Dent J*, vol. 172, no. 7, pp. 271–8, 1992.

[12] W. J. Moore, “The role of sugar in the aetiology of dental caries. 1. Sugar and the antiquity of dental caries.,” *J Dent, 1983.*, vol. 11, no. 3, pp. 189–90, 1983.

[13] Y. Chen, “The antimicrobial efficacy of Fructus mume extract on orthodontic bracket: a monospecies-biofilm model study in vitro.,” *Arch Oral Biol*, vol. 56, no. 1, pp. 16–21, 2010.

[14] J. Abranches, J. H. Miller, A. R. Martinez, R. A. Simpson-Haidaris, P. J. Burne, and J. A. Lemos, “The Collagen-Binding Protein Cnm Is Required for Streptococcus mutans Adherence to and Intracellular Invasion of Human Coronary Artery Endothelial Cells.,” *Infection and Immunity*, vol. 79, no. 6, pp. 2277–2284, 2011.

[15] E. Giertsen, R. A. Arthur, and B. Guggenheim, “Effects of Xylitol on Survival of Mutans Streptococci in Mixed-Six-Species in vitro Biofilms Modelling Supragingival Plaque.,” *Caries Research*, vol. 45, no. 1, p. 31., 2010.

[16] M. I. Klein, L. DeBaz, S. Agidi, H. Lee, G. Xie, A. H. M. Lin, B. R. Hamaker, J. A. Lemos, and H. Koo, “Dynamics of Streptococcus mutans Transcriptome in Response to Starch and Sucrose during Biofilm Development.,” *PLoS One.*, vol. 5, no. 10, p. e13478., 2010.

[17] A. Rmaile, D. Carugo, L. Capretto, X. Zhang, J. A. Wharton, P. J. Thurner, M. Aspiras, M. Ward, and P. Stoodley, “Microbial tribology and disruption of dental plaque bacterial biofilms,” *WEAR*, p. In press, 2013.

[18] J. Costerton, K. Cheng, G. Geesey, T. Ladd, J. Nickel, M. Dasgupta, and T. Marrie, “Bacterial biofilms in nature and disease.,” *ANNUAL REVIEW OF MICROBIOLOGY*, no. 41, pp. 435–64, 1987.

[19] N. S. Jakubovics and P. E. Kolenbrander, “The road to ruin: the formation of disease-associated oral biofilms,” *Oral Diseases*, vol. 16, no. 8, pp. 729–739, Nov. 2010.

[20] H.-C. Flemming, T. R. Neu, and D. J. Wozniak, “The EPS Matrix: The ‘House of Biofilm Cells’,” *Journal of Bacteriology* , vol. 189 , no. 22 , pp. 7945–7947, Nov. 2007.

[21] H.-C. Flemming and J. Wingender, “The biofilm matrix,” *Nat Rev Micro*, vol. 8, no. 9, pp. 623–633, Sep. 2010.

[22] J. W. Costerton, P. S. Stewart, and E. P. Greenberg, “Bacterial biofilms: A common cause of persistent infections.,” *Science*, no. 284, pp. 1318–1322, 1999.

[23] C. A. Fux, J. W. Costerton, P. S. Stewart, and P. Stoodley, “Survival strategies of infectious biofilms,” *Trends in Microbiology*, vol. 13, no. 1, pp. 34–40, Jan. 2005.

[24] P. D. Marsh, “Dental plaque as a biofilm: the significance of pH in health and caries.,” *Compend Contin Educ Dent*, vol. 30, no. 2, pp. 76–8, 80, 83–7; quiz 88, 90., 2009.

[25] V. Zijnge, “Oral biofilm architecture on natural teeth.,” *PLoS One*, vol. 5, no. 2, p. e9321, 2010.

[26] A. G. Gristina, “Biomaterial-centered infection: microbial adhesion versus tissue integration.,” *Science*, vol. 237, no. 4822, pp. 1588–95., 1987.

[27] S. K. Hendricks, C. Kwok, M. Shen, T. A. Horbett, B. D. Ratner, and J. D. Bryers, “Plasma-deposited membranes for controlled release of antibiotic to prevent bacterial adhesion and biofilm formation,” *Journal of Biomedical Materials Research*, vol. 50, no. 2, pp. 160–170, May 2000.

[28] C. Hannig, M. Hannig, and T. Attin, “Enzymes in the acquired enamel pellicle,” *European Journal of Oral Sciences*, vol. 113, no. 1, pp. 2–13, Feb. 2005.

[29] D. Bakker, F. Huijs, J. DeVries, J. Klijnstra, J. Busscher, and H. van der Mei, “Bacterial deposition to fluoridated and non-fluoridated polyurethane coatings with different elastic modulus and surface tension in a parallel plate and a stagnation point flow chamber.,” *Col Surf B: Biointerf*, no. 32, pp. 179–190., 2003.

[30] M. Salerno, B. Logan, and D. Velegol, “Importance of Molecular Details in Predicting Bacterial Adhesion to Hydrophobic Surfaces,” *Langmuir*, no. 20, pp. 10625–10629, 2004.

[31] P. Steinberg, R. Schneider, and S. Kjelleberg, “Chemical defenses of seaweeds against microbial colonization,” *Biodegradation*, vol. 8, no. 3, pp. 211–220, 1997.

[32] H. J. Busscher, W. Norde, and H. C. van der Mei, “Specific Molecular Recognition and Nonspecific Contributions to Bacterial Interaction Forces,” *Applied and Environmental Microbiology* , vol. 74 , no. 9 , pp. 2559–2564, May 2008.

[33] R. Bos, “Physico-chemistry of initial microbial adhesive interactions--its mechanisms and methods for study.,” *EMS Microbiol Rev*, vol. 32, no. 2, pp. 179–230., 1999.

[34] C. J. Whittaker, C. M. Klier, and P. E. Kolenbrander, “MECHANISMS OF ADHESION BY ORAL BACTERIA,” *Annual Review of Microbiology*, vol. 50, no. 1, pp. 513–552, Oct. 1996.

[35] K. C. Marshall, “Mechanisms of bacterial adhesion at solid± water interface.,” *In Bacterial Adhesion ed. Savage, D.C. and Fletcher, M. pp. 133±161.*, p. New York: Plenum Press., 1985.

[36] R. Lux and W. Shi, “Chemotaxis-guided Movements in Bacteria,” *Critical Reviews in Oral Biology & Medicine* , vol. 15 , no. 4 , pp. 207–220, Jul. 2004.

[37] H. C. Berg and D. A. Brown, “Chemotaxis in Escherichia coli analysed by three-dimensional tracking.,” *Nature*, no. 239, pp. 500–504, 1972.

[38] M. C. M. Loosdrecht and A. J. B. Zehnder, “Energetics of bacterial adhesion,” *Experientia*, vol. 46, no. 8, pp. 817–822, 1990.

[39] B. V Derjaguin, Y. I. Rabinovich, and N. V Churaev, “Direct measurement of molecular forces,” *Nature*, vol. 272, no. 5651, pp. 313–318, Mar. 1978.

[40] M. van Loosdrecht, J. Lyklema, W. Norde, and A. Zehnder, “Bacterial Adhesion: A Physicochemical Approach,” *Microbial Ecology*, vol. 17, no. 1, pp. 1–15, 1989.

[41] J. Ward and R. Berkeley, “The microbial cell surface and adhesion.,” *In: Berkeley RCW, Lynch JM, Melling J, Rutter PR, Vincent B (eds) Microbial Adhesion to Surfaces. Ellis Horwood, Chichester, pp. 47-66.*, 1980.

[42] A. I. Railkin, *Marine biofouling. Colonization processess and defenses.* Boca Raton: CRC Press., 2004, p. 304.

[43] N. S. Jakubovics, N. Strömberg, C. J. Van Dolleweerd, C. G. Kelly, and H. F. Jenkinson, “Differential binding specificities of oral streptococcal antigen I/II family adhesins for human or bacterial ligands,” *Molecular Microbiology*, vol. 55, no. 5, pp. 1591–1605, Mar. 2005.

[44] W. Loesche, “Role of Streptococcus mutans in human dental decay.,” *Microbiol Rev.*, no. 50, p. 353, 1986.

[45] X. Xue, H. Sztajer, N. Buddruhs, J. Petersen, and M. et al. Rohde, “Lack of the delta subunit of RNA polymerase increases virulence related traits of Streptococcus mutans.,” *PLoS ONE.*, vol. 6, no. 5, p. e20075, 2011.

[46] A. F. P. Leme, H. Koo, C. M. Bellato, G. Bedi, and J. A. Cury, “The Role of Sucrose in Cariogenic Dental Biofilm Formation—New Insight,” *Journal of Dental Research* , vol. 85 , no. 10 , pp. 878–887, Oct. 2006.

[47] N. Takahashi and B. Nyvad, “The Role of Bacteria in the Caries Process: Ecological Perspectives ,” *Journal of Dental Research* , vol. 90 , no. 3 , pp. 294–303, Mar. 2011.

[48] K. Mäkinen, “Sugar Alcohols, Caries Incidence, and Remineralization of Caries Lesions: A Literature Review,” *International Journal of Dentistry*, vol. 2010, p. 23.

[49] M. Matsumoto-Nakano, M. Tsuji, A. Amano, and T. Ooshima, “Molecular interactions of alanine-rich and proline-rich regions of cell surface protein

antigen c in Streptococcus mutans," *Oral Microbiology and Immunology*, vol. 23, no. 4, pp. 265–270, Aug. 2008.

[50] W. H. BOWEN, K. SCHILLING, E. GIERTSEN, S. PEARSON, S. F. LEE, A. BLEIWEIS, and D. BEEMAN, "Role of a Cell Surface-Associated Protein in Adherence and Dental Caries," *Infection and Immunity*, vol. 59, no. 12, pp. 4606–4609, 1991.

[51] K. S. Devulapalle, S. D. Goodman, Q. Gao, A. Hemsley, and G. Mooser, "Knowledge-based model of a glucosyltransferase from the oral bacterial group of mutans streptococci," *Protein Science*, vol. 6, no. 12, pp. 2489–2493, Dec. 1997.

[52] P. D. Marsh, "Dental Plaque as a Microbial Biofilm," *Caries Research*, vol. 38, no. 3, pp. 204–211, 2004.

[53] P. E. Kolenbrander, R. J. Palmer Jr, S. Periasamy, and N. S. Jakubovics, "Oral multispecies biofilm development and the key role of cell–cell distance," *Nat Rev Micro*, vol. 8, no. 7, pp. 471–480, Jul. 2010.

[54] J. Kreth, J. Merritt, L. Zhu, W. Shi, and F. Qi, "Cell density- and ComE-dependent expression of a group of mutacin and mutacin-like genes in Streptococcus mutans," *FEMS Microbiology Letters*, vol. 265, no. 1, pp. 11–17, Dec. 2006.

[55] R. G. Quivey, W. L. Kuhnert, and K. Hahn, "Genetics of Acid Adaptation in Oral Streptococci," *Critical Reviews in Oral Biology & Medicine* , vol. 12 , no. 4 , pp. 301–314, Jan. 2001.

[56] W. L. Kuhnert, G. Zheng, R. C. Faustoferri, and R. G. Quivey, "The F-ATPase Operon Promoter of Streptococcus mutans Is Transcriptionally Regulated in Response to External pH," *Journal of Bacteriology* , vol. 186 , no. 24 , pp. 8524–8528, Dec. 2004.

[57] R. N. Grüneberg, F. Antunes, H. F. Chambers, J. Garau, W. Graninger, F. Menichetti, W. E. Peetermans, D. Pittet, P. M. Shah, and D. Vogelaers, "The role of glycopeptide antibiotics in the treatment of infective endocarditis,"

International Journal of Antimicrobial Agents, vol. 12, no. 3, pp. 191–198, Jul. 1999.

[58] J. Lu, W. Zhang, Y. Hao, and Y. Zhu, "Defect of cell wall construction may shield oral bacteria's survival in bloodstream and cause infective endocarditis," *Medical Hypotheses*, vol. 73, no. 6, pp. 1055–1057, Dec. 2009.

[59] N. Taniguchi, K. Nakano, R. Nomura, S. Naka, A. Kojima, M. Matsumoto, and T. Ooshima, "Defect of glucosyltransferases reduces platelet aggregation activity of Streptococcus mutans: Analysis of clinical strains isolated from oral cavities," *Archives of Oral Biology*, vol. 55, no. 6, pp. 410–416, Jun. 2010.

[60] R. Nomura, K. Nakano, H. Nemoto, K. Fujita, S. Inagaki, T. Takahashi, K. Taniguchi, M. Takeda, H. Yoshioka, A. Amano, and T. Ooshima, "Isolation and characterization of Streptococcus mutans in heart valve and dental plaque specimens from a patient with infective endocarditis," *Journal of Medical Microbiology* , vol. 55 , no. 8 , pp. 1135–1140, Aug. 2006.

[61] J. M. ten Cate, "Biofilms, a new approach to the microbiology of dental plaque," *Odontology*, vol. 94, no. 1, pp. 1–9, 2006.

[62] P. D. Marsh, A. Moter, and D. A. Devine, "Dental plaque biofilms: communities, conflict and control," *Periodontology 2000*, vol. 55, no. 1, pp. 16–35, Feb. 2011.

[63] P. Stoodley, Z. Lewandowski, J. D. Boyle, and H. M. Lappin-Scott, "Oscillation characteristics of biofilm streamers in turbulent flowing water as related to drag and pressure drop," *Biotechnology and Bioengineering*, vol. 57, no. 5, pp. 536–544, Mar. 1998.

[64] A. Houry, M. Gohar, J. Deschamps, E. Tischenko, S. Aymerich, A. Gruss, and R. Briandet, "From the Cover: Bacterial swimmers that infiltrate and take over the biofilm matrix," *Proceedings of the National Academy of Sciences*, vol. 109, no. 32, pp. 13088–13093, 2012.

[65] T. J. M. Steenbergen, A. J. Winkelhoff, and J. Graaff, "Pathogenic synergy: mixed infections in the oral cavity," *Antonie van Leeuwenhoek*, vol. 50, no. 5–6, pp. 789–798, 1984.

[66] Z. Metzger, Y. Y. Lin, F. Dimeo, W. W. Ambrose, M. Trope, and R. R. Arnold, "Synergistic pathogenicity of Porphyromonas gingivalis and Fusobacterium nucleatum in the mouse subcutaneous chamber model.," *Journal of endodontics*, vol. 35, no. 1, pp. 86–94, Jan. 2009.

[67] V. Körstgens, H. Flemming, J. Wingender, and W. Borchard, "Influence of calcium ions on the mechanical properties of a model biofilm of mucoid Pseudomonas aeruginosa.," *Water Sci Technol*, vol. 43, no. 6, pp. 49–57, 2001.

[68] P. Stoodley, R. Cargo, C. Rupp, S. Wilson, and I. Klapper, "Biofilm material properties as related to shear-induced deformation and detachment phenomena.," *J Ind Microbiol Biotechnol*, vol. 29, no. 6, pp. 361–7., 2002.

[69] F. Ahimou, M. J. Semmens, P. J. Novak, and G. Haugstad, "Biofilm Cohesiveness Measurement Using a Novel Atomic Force Microscopy Methodology," *Applied and Environmental Microbiology* , vol. 73 , no. 9 , pp. 2897–2904, May 2007.

[70] B. W. Towler, C. J. Rupp, A. L. B. Cunningham, and P. Stoodley, "Viscoelastic Properties of a Mixed Culture Biofilm from Rheometer Creep Analysis," *Biofouling*, vol. 19, no. 5, pp. 279–285, Oct. 2003.

[71] P. Stoodley, Z. Lewandowski, J. D. Boyle, and H. M. Lappin-Scott, "The formation of migratory ripples in a mixed species bacterial biofilm growing in turbulent flow," *Environmental Microbiology*, vol. 1, no. 5, pp. 447–455, Sep. 1999.

[72] C. J. Rupp, C. A. Fux, and P. Stoodley, "Viscoelasticity of Staphylococcus aureus Biofilms in Response to Fluid Shear Allows Resistance to Detachment and Facilitates Rolling Migration," *Applied and Environmental Microbiology* , vol. 71 , no. 4 , pp. 2175–2178, Apr. 2005.

[73] G. Couarraze and J. L. Grossiord, *Initiation à la rhéologie*. Lavoizier – Tec & Doc, 1991, pp. 60–91.

[74] W. Nowacki, *Dynamic Problems of Thermoelasticity*. Springer, Warszawa, 1975.

[75] W. G. Characklis, “Biofilm Development and Destrution in Turbulent Flow,” *Ozone: Science & Engineering*, vol. 1, no. 2, pp. 167–181, Jan. 1979.

[76] A. Ohashi and H. Harada, “A novel concept for evaluation of biofilm adhesion strength by applying tensile force and shear force,” *Water Science and Technology*, vol. 34, no. 5–6, pp. 201–211, 1996.

[77] P. Stoodley, Z. Lewandowski, J. D. Boyle, and H. M. Lappin-Scott, “Structural deformation of bacterial biofilms caused by short-term fluctuations in fluid shear: An in situ investigation of biofilm rheology,” *Biotechnology and Bioengineering*, vol. 65, no. 1, pp. 83–92, Oct. 1999.

[78] I. Klapper, C. J. Rupp, R. Cargo, B. Purvedorj, and P. Stoodley, “Viscoelastic fluid description of bacterial biofilm material properties,” *Biotechnology and Bioengineering*, vol. 80, no. 3, pp. 289–296, Nov. 2002.

[79] T. Shaw, M. Winston, C. Rupp, I. Klapper, and P. Stoodley, “Commonality of elastic relaxation times in biofilms.,” *Phys. Rev. Lett.*, vol. 93, no. 9, pp. 1–4, 2004.

[80] J. W. Costerton, Z. Lewandowski, D. E. Caldwell, D. R. Korber, and H. M. Lappin-Scott, “Microbial Biofilms,” *Annual Review of Microbiology*, vol. 49, no. 1, pp. 711–745, Oct. 1995.

[81] D. de Beer, P. Stoodley, F. Roe, and Z. Lewandowski, “Effects of biofilm structures on oxygen distribution and mass transport,” *Biotechnology and Bioengineering*, vol. 43, no. 11, pp. 1131–1138, May 1994.

[82] M. M. Klausen, T. R. Thomsen, J. L. Nielsen, L. H. Mikkelsen, and P. H. Nielsen, “Variations in microcolony strength of probe-defined bacteria in activated sludge flocs,” *FEMS Microbiology Ecology*, vol. 50, no. 2, pp. 123–132, Nov. 2004.

[83] M. J. Chen, Z. Zhang, and T. R. Bott, “Effects of operating conditions on the adhesive strength of Pseudomonas fluorescens biofilms in tubes,” *Colloids and Surfaces B: Biointerfaces*, vol. 43, no. 2, pp. 61–71, Jun. 2005.

[84] V. Körstgens, H.-C. Flemming, J. Wingender, and W. Borchard, “Uniaxial compression measurement device for investigation of the mechanical stability of biofilms,” *Journal of Microbiological Methods*, vol. 46, no. 1, pp. 9–17, Jul. 2001.

[85] S. Aggarwal, E. H. Poppele, and R. M. Hozalski, “Development and testing of a novel microcantilever technique for measuring the cohesive strength of intact biofilms,” *Biotechnology and Bioengineering*, vol. 105, no. 5, pp. 924–934, Apr. 2010.

[86] A. W. Cense, E. A. G. Peeters, B. Gottenbos, F. P. T. Baaijens, A. M. Nuijs, and M. E. H. van Dongen, “Mechanical properties and failure of Streptococcus mutans biofilms, studied using a microindentation device,” *Journal of Microbiological Methods*, vol. 67, no. 3, pp. 463–472, Dec. 2006.

[87] E. H. Poppele and R. M. Hozalski, “Micro-cantilever method for measuring the tensile strength of biofilms and microbial flocs,” *Journal of Microbiological Methods*, vol. 55, no. 3, pp. 607–615, Dec. 2003.

[88] A. M. Vinogradov, M. Winston, C. J. Rupp, and P. Stoodley, “Rheology of biofilms formed from the dental plaque pathogen Streptococcus mutans,” *Biofilms*, vol. 1, no. 01, pp. 49–56, 2004.

[89] E. Paramonova, E. D. de Jong, B. P. Krom, H. C. van der Mei, H. J. Busscher, and P. K. Sharma, “Low-Load Compression Testing: a Novel Way of Measuring Biofilm Thickness,” *Applied and Environmental Microbiology* , vol. 73 , no. 21 , pp. 7023–7028, Nov. 2007.

[90] E. Paramonova, O. J. Kalmykowa, H. C. van der Mei, H. J. Busscher, and P. K. Sharma, “Impact of Hydrodynamics on Oral Biofilm Strength,” *Journal of Dental Research* , vol. 88 , no. 10 , pp. 922–926, Oct. 2009.

[91] W. Characklis, G. McFeters, and K. Marshall, *Physiological ecology in biofilm systems. In: Characklis WG, Marshall KC, editors. Biofilms.* New York: John Wiley & Sons, 1990, pp. 341–94.

[92] L. Pons, M.-L. Délia, and A. Bergel, “Effect of surface roughness, biofilm coverage and biofilm structure on the electrochemical efficiency of microbial cathodes,” *Bioresource Technology*, vol. 102, no. 3, pp. 2678–2683, Feb. 2011.

[93] S. Li, “The effect of surface roughness, produced by ultrasonic scaling, on biofilm formation and integrity on selected restorative materials.,” University of Otago, 2013.

[94] F. G. Lima, A. R. Romano, M. B. Correa, and F. F. Demarco, “Influence of microleakage, surface roughness and biofilm control on secondary caries formation around composite resin restorations: an in situ evaluation ,” *Journal of Applied Oral Science* , vol. 17 . scielo , pp. 61–65, 2009.

[95] W. Teughels, N. Van Assche, I. Sliepen, and M. Quirynen, “Effect of material characteristics and/or surface topography on biofilm development,” *Clinical Oral Implants Research*, vol. 17, no. S2, pp. 68–81, Oct. 2006.

[96] J. B. Schlenoff, A. H. Rmaile, and C. B. Bucur, “Hydration Contributions to Association in Polyelectrolyte Multilayers and Complexes: Visualizing Hydrophobicity,” *Journal of the American Chemical Society*, vol. 130, no. 41, pp. 13589–13597, Sep. 2008.

[97] K. Guo, S. Freguia, P. G. Dennis, X. Chen, B. C. Donose, J. Keller, J. J. Gooding, and K. Rabaey, “Effects of Surface Charge and Hydrophobicity on Anodic Biofilm Formation, Community Composition, and Current Generation in Bioelectrochemical Systems,” *Environmental Science & Technology*, vol. 47, no. 13, pp. 7563–7570, Jun. 2013.

[98] R. Donlan, “Biofilms: microbial life on surfaces,” *Emerg Infect Dis.*, vol. 8, no. 9, pp. 881–90, 2002.

[99] J. Pringle and M. Fletcher, “Influence of Substratum Wettability on Attachment of Freshwater Bacteria to Solid Surfaces,” *Appl Environ Microbiol.*, vol. 45, no. 3, pp. 811–817, 1983.

[100] B. Bendinger, H. Rijnaarts, K. Altendorf, and A. Zehnder, “Physicochemical cell surface and adhesive properties of coryneform bacteria related to the

presence and chain length of mycolic acids," *Appl Environ Microbiol.*, vol. 59, no. 11, pp. 3973–3977, 1993.

[101] J. A. Perry, D. G. Cvitkovitch, and C. M. Lévesque, "Cell death in Streptococcus mutans biofilms: a link between CSP and extracellular DNA," *FEMS Microbiology Letters*, vol. 299, no. 2, pp. 261–266, Oct. 2009.

[102] A. W. Cense, B. Dongen, M.E.H. van Gottenbos, A. M. Nuijs, and S. Y. & Shulepov, "Removal of biofilms by impinging water droplets.," *Journal of Applied Physics*, vol. 100, no. 12, p. 124701, 2006.

[103] J. B. Xavier, C. Picioreanu, S. A. Rani, M. C. M. van Loosdrecht, and P. S. Stewart, "Biofilm-control strategies based on enzymic disruption of the extracellular polymeric substance matrix – a modelling study," *Microbiology* , vol. 151 , no. 12 , pp. 3817–3832, Dec. 2005.

[104] M. Böl, R. B. Möhle, M. Haesner, T. R. Neu, H. Horn, and R. Krull, "3D finite element model of biofilm detachment using real biofilm structures from CLSM data," *Biotechnology and Bioengineering*, vol. 103, no. 1, pp. 177–186, May 2009.

[105] P. Zhu, Y. Han, Y. Lin, and Y. et aL Xu, "A Computational Fluid Dynamic Analysis of Peri-Bracket Salivary Flow Influencing the Microbial and Periodontal Parameters.," *PLos ONE*, vol. 8, no. 4, 2013.

[106] I. Gebeshuber, A. Pauschitz, and F. Franek, "Biotribological model systems for emerging nanometer scale technologies," in *in Proc. Emerging Technologies*, 2006.

[107] I. Gebeshuber, "Tribology - Materials Surfaces & Interfaces," vol. 2, pp. 200–212., 2008.

[108] P. Stoodley, K. Sauer, D. G. Davies, and J. W. Costerton, "BIOFILMS AS COMPLEX DIFFERENTIATED COMMUNITIES," *Annual Review of Microbiology*, vol. 56, no. 1, pp. 187–209, Oct. 2002.

[109] M. J. Tighe, P. Kite, D. Thomas, W. N. Fawley, and M. J. Mcmahon, "Rapid Diagnosis of Catheter-Related Sepsis Using the Acridine Orange Leukocyte

Cytospin Test and an Endoluminal Brush," *Journal of Parenteral and Enteral Nutrition* , vol. 20 , no. 3 , pp. 215–218, May 1996.

[110] H. Ceri, M. E. Olson, C. Stremick, R. R. Read, D. Morck, and A. Buret, "The Calgary Biofilm Device: New Technology for Rapid Determination of Antibiotic Susceptibilities of Bacterial Biofilms," *Journal of Clinical Microbiology* , vol. 37 , no. 6 , pp. 1771–1776, Jun. 1999.

[111] J. Thomas, I. Lynton, and H. Rinde, "Economic impact of biofilms on treatment costs," pp. 21–38, 2006.

[112] X. Y. Zhu, J. Lubeck, and J. J. Kilbane, "Characterization of Microbial Communities in Gas Industry Pipelines," *Applied and Environmental Microbiology* , vol. 69 , no. 9 , pp. 5354–5363, Sep. 2003.

[113] J. W. Graves and E. H. Sullivan, "Internal corrosion in gas gathering systems and transmission lines.," *Mater. Prot.*, vol. 5, pp. 33–37.

[114] M. Salta, J. A. Wharton, S. Wirwinski, U. Mart, R. J. K. Wood, L. R. Goodes, and K. R. Stokes, "Designing biomimetic antifouling surfaces.," *Philosophical Transactions of the Royal Society A: Mathematical, Physical and Engineering Sciences*, vol. 368, no. 1929, pp. 4729–4754, 2010.

[115] J. B. Kaplan, "Biofilm Dispersal: Mechanisms, Clinical Implications, and Potential Therapeutic Uses," *Journal of Dental Research* , vol. 89 , no. 3 , pp. 205–218, Mar. 2010.

[116] P. Marsh, "Dental plaque as a biofilm and a microbial community – implications for health and disease," *BMC Oral Health*, vol. 6, no. 1, pp. 1–7, 2006.

[117] A. Horswill, P. Stoodley, P. Stewart, and M. Parsek, "The effect of the chemical, biological, and physical environment on quorum sensing in structured microbial communities," *Analytical and Bioanalytical Chemistry*, vol. 387, no. 2, pp. 371–380, 2007.

[118] P. J. Thurner, B. Erickson, Z. Schriock, J. Langan, J. Scott, M. Zhao, J. C. Weaver, G. E. Fantner, P. Turner, J. H. Kindt, G. Schitter, D. E. Morse, and P.

K. Hansma, “High-speed photography of the development of microdamage in trabecular bone during compression.,” *Journal of Materials Research*, vol. 21, no. 5, pp. 1093–1100, 2006.

[119] P. D. Fey, J. S. Ulphani, F. Götz, C. Heilmann, D. Mack, and M. E. Rupp, “Characterization of the Relationship between Polysaccharide Intercellular Adhesin and Hemagglutination in Staphylococcus epidermidis,” *Journal of Infectious Diseases* , vol. 179 , no. 6 , pp. 1561–1564, Jun. 1999.

[120] L. Hall-Stoodley, J. W. Costerton, and P. Stoodley, “Bacterial biofilms: from the Natural environment to infectious diseases,” *Nat Rev Micro*, vol. 2, no. 2, pp. 95–108, Feb. 2004.

[121] I. N. Sneddon, “The relation between load and penetration in the axisymmetric boussinesq problem for a punch of arbitrary profile,” *International Journal of Engineering Science*, vol. 3, no. 1, pp. 47–57, May 1965.

[122] B. Purevdorj-Gage, W. J. Costerton, and P. Stoodley, “Phenotypic differentiation and seeding dispersal in non-mucoid and mucoid Pseudomonas aeruginosa biofilms,” *Microbiology* , vol. 151 , no. 5 , pp. 1569–1576, May 2005.

[123] N. Rajaratnam, “Turbulent jets.,” *ELSEVIER*, pp. 231–234, 1976.

[124] A. Palevski, I. Glaich, S. Portnoy, E. Linder-Ganz, and A. Gefen, “Stress relaxation of porcine gluteus muscle subjected to sudden transverse deformation as related to pressure sore modeling.,” *J. Biomech. Eng.*, vol. 128, no. 5, pp. 782–7, 2006.

[125] S. P. Lin and R. D. Reitz, “DROP AND SPRAY FORMATION FROM A LIQUID JET,” *Annual Review of Fluid Mechanics*, vol. 30, no. 1, pp. 85–105, Jan. 1998.

[126] J. D. Ferry, *Viscoelastic Properties of Polymers*. 3rd. ed., Wiley, New York, 1980.

[127] R. N. Wenzel, “RESISTANCE OF SOLID SURFACES TO WETTING BY WATER,” *Industrial & Engineering Chemistry*, vol. 28, no. 8, pp. 988–994, Aug. 1936.

[128] A. Rmaile, “Characterization of polyelectrolyte multilayers and complexes: towards bio-implant applications.,” Florida State University, 2007.

[129] M. Darby, *Dental hygiene theory and practice.*, 2nd ed. Philadelphia : W.B. Saunders, 2003.

[130] P. K. Sharma, M. J. Gibcus, H. C. van der Mei, and H. J. Busscher, “Influence of Fluid Shear and Microbubbles on Bacterial Detachment from a Surface,” *Applied and Environmental Microbiology* , vol. 71 , no. 7 , pp. 3668–3673, Jul. 2005.

[131] P. R. Rutter and B. Vincent, “Attachment mechanisms in the surface growth of microorganisms, In M. J. Bazin and J. I. Prosser (ed.) Physiological models in microbiology, vol. II. CRC Press, Boca Raton, Fla,” vol. II, pp. 87–107, 1988.

[132] M. R. Parini, D. L. Eggett, and W. G. Pitt, “Removal of Streptococcus mutans biofilm by bubbles,” *Journal of Clinical Periodontology*, vol. 32, no. 11, pp. 1151–1156, Nov. 2005.

[133] C. Gomez-Suarez, H. J. Busscher, and H. C. van der Mei, “Analysis of bacterial detachment from substratum surfaces by the passage of air-liquid interfaces.,” *Appl Environ Microbiol*, vol. 67, no. 6, pp. 2531–7, 2001.

[134] H. Adams, M. Winston, J. Heersink, J. Buckingham-Meyer, KA Costerton, and P. Stoodley, “Development of a laboratory model to assess the removal of biofilm from interproximal spaces by powered tooth brushing,” *Am J Dent*, no. 15, p. 12B–17B, 2002.

[135] D. M. Lyle, “Use of a water flosser for interdental cleaning.,” *Compend Contin Educ Dent*, vol. 32, no. 9, pp. 78, 80–72, 2011.

[136] J. Ferziger and M. Peric, *Computational methods for fluid dynamics*, 3rd ed. Springer, 2002.

[137] M. Rein, “Phenomena of liquid drop impact on solid and liquid surfaces,” *Fluid Dynamics Research*, vol. 12, no. 2, p. 61, 1993.

[138] M. R. Benoit, C. G. Conant, C. Ionescu-Zanetti, M. Schwartz, and A. Matin, “New Device for High-Throughput Viability Screening of Flow Biofilms,” *Applied and Environmental Microbiology* , vol. 76 , no. 13 , pp. 4136–4142, Jul. 2010.

[139] A. Ohashi and H. Harada, “Adhesion strength of biofilm developed in an attached-growth reactor,” *WATER SCIENCE AND TECHNOLOGY*, vol. 29, no. 10/11, p. 281, 1994.

[140] C. W. Hirt and B. D. Nichols, “Volume of fluid /VOF/ method for the dynamics of free boundaries,” *Journal of Computational Physics*, vol. 39, pp. 201–225, 1981.

[141] D. C. Wilcox, *Turbulence Modeling for CFD*, 3rd ed. DCW Industries, Inc., La Canada CA, 2006.

[142] K. A. Sallam, Z. Dai, and G. . Faeth, “Liquid breakup at the surface of turbulent round liquid jets in still gases,” *International Journal of Multiphase Flow*, vol. 28, no. 3, p. 427, 2002.

[143] J. Heersink, W. J. Costerton, and P. Stoodley, “Influence of the sonicare toothbrush on the structure and thickness of laboratory grown Streptococcus mutans biofilms assessed by digital time-lapse and confocal microscopy,” *American J. Dentistry*, vol. 16, no. 2, pp. 79–83, 2003.

[144] J. van Houte, “Role of Micro-organisms in Caries Etiology,” *Journal of Dental Research* , vol. 73 , no. 3 , pp. 672–681, Mar. 1994.

[145] C. von Ohle, A. Gieseke, L. Nistico, E. M. Decker, D. deBeer, and P. Stoodley, “Real-Time Microsensor Measurement of Local Metabolic Activities in Ex Vivo Dental Biofilms Exposed to Sucrose and Treated with Chlorhexidine ,” *Applied and Environmental Microbiology* , vol. 76 , no. 7 , pp. 2326–2334, Apr. 2010.

[146] P. K. Sharma, M. J. Gibcus, H. C. Van Der Mei, and H. J. Busscher, "Microbubble-induced detachment of coadhering oral bacteria from salivary pellicles," *European Journal of Oral Sciences*, vol. 113, no. 4, pp. 326–332, Aug. 2005.

[147] J. A. von Fraunhofer, "Adhesion and Cohesion," *International Journal of Dentistry*, p. Article ID 951324, 8 pages, 2012.

[148] H. C. Flemming, J. Wingender, T. Griegbe, and C. Mayer, "Physico-chemical properties of biofilms. In: Evans LV (ed) Biofilms: recent advances in their study and control.," *Harwood Academic, Amsterdam*, pp. 19–34, 2000.

[149] R. C. Shields, N. Mokhtar, M. Ford, M. J. Hall, J. G. Burgess, M. ElBadawey, and N. S. Jakubovics, "Efficacy of a Marine Bacterial Nuclease against Biofilm Forming Microorganisms Isolated from Chronic Rhinosinusitis," *PLos ONE*, vol. 8, no. 2, p. e55339., 2013.

[150] I. W. Sutherland, "The biofilm matrix – an immobilized but dynamic microbial environment," *Trends in Microbiology*, vol. 9, no. 5, pp. 222–227, May 2001.

[151] R. Nijland, M. J. Hall, and J. G. Burgess, "Dispersal of biofilms by secreted, matrix degrading, bacterial DNase.," *PloS one*, vol. 5, no. 12, p. e15668, 2010.

[152] J. B. Kaplan, C. Ragunath, K. Velliyagounder, D. H. Fine, and N. Ramasubbu, "Enzymatic Detachment of Staphylococcus epidermidis Biofilms," *Antimicrob Agents Chemother*, vol. 48, no. 7, pp. 2633–2636, 2004.